UNIVERSITY OF CALIFORNIA
RIVERSIDE

Structural Engineering of Optical Nanomaterials

A Dissertation submitted in partial satisfaction
of the requirements for the degree of

Doctor of Philosophy

in

Materials Science and Engineering

by

Yaocai Bai

March 2017

Dissertation Committee:
Dr. Yadong Yin, Chairperson
Dr. David Kisailus
Dr. Juchen Guo

The Dissertation of Yaocai Bai is approved:

_____

_____

_____

Committee Chairperson

University of California, Riverside

Acknowledgements

Though only my name appears on the cover of this dissertation, I could never have reached the heights and explored the depths and finished my Ph.D. study smoothly without the help, support, guidance and efforts of many people.

First, I would like to express my deepest gratitude to my advisor Professor Yadong Yin for the continuous support of my Ph.D study and related research, for his insightful guidance and infectious enthusiasm, for his endless patience and immense knowledge. He has provided me with valuable ideas and offered me great freedom in research. Professor Yin will definitely be my role model in my future life and career. I would also like to thank Professor Juchen Guo and Professor David Kisailus for being my Dissertation committees and providing me useful feedback to improve my research and my dissertation.

I am also grateful to all my lab colleagues for their inspirations and collaborations. I greatly appreciate the opportunity I have had to work with Dr. Wenshou Wang, Dr. Le He, Dr. James Goebl, Dr. Michael Dahl, Dr. Mingsheng Wang, Dr. Yiding Liu, Dr. Guocheng Lyu, Dr. Guangyi Chen, Dr. Lishun Fu, Wenjing Xu, Ji Feng, Xiaojing Wang, Zhiwei Li, Aiqin Gao, Fenglei Lyu, Guohui Qin, Yun Liu, Shichuan Li, Chunyu Zhou, Qianqian Shang, Fan Yang, Rashed Aleisa and all the other past and current members. I am also thankful to Dr. Chuanbo Gao and Dr. Xiaxi Yao for helpful discussions. I must thank Dr. Yu Lu for her kind assistance in both scientific research and daily life.

Many thanks also go to Dr. Krassimir Bozhilov and Dr. Jie Zhou for their kind assistance in using their facilities at UCR. I also want to thank my friends at UCR for helping me in both research and life. They are Dr. Yuan Wang, Dr. Wei Wang, and Chengyin Fu.

Most importantly, I would like to thank my family. None of this would have been possible without the love and patience of my family. I would like to express my heart-felt gratitude to my parents Lan Wang and Kezhou Bai, my parents-in-law Zixiang Li and Jianzhong Di, my wife Xue Di, and my son Daniel for everything they have done for me.

Finally, I would like to thank the institutions responsible for financially supporting this work, including the National Science Foundation (DMR-0956081, CHE-1308587) and the U.S. Department of Energy (DE-SC0002247).

Dedication

To my wife Xue and my son Daniel.

ABSTRACT OF THE DISSERTATION

Structural Engineering of Optical Nanomaterials

by

Yaocai Bai

Doctor of Philosophy, Graduate Program in Materials Science and Engineering
University of California, Riverside, March 2017
Dr. Yadong Yin, Chairperson

Optical nanomaterials have attracted tremendous interest from a large community of researchers because of their widespread applications. The optical properties are closely related the structures of nanomaterials, thus making the structural engineering over nanomaterials in a controlled manner an important topic. This dissertation discusses our efforts in the engineering and applications of optical nanomaterials including noble metal nanostructures and hollow nanostructures.

Noble metal nanostructures possess novel optical properties due to localized surface plasmon resonances. Controllable synthesis of noble metal nanostructures with desired morphology and optical properties is highly desirable. In this work, we attempt to prepare anisotropic Ag/Au alloy nanorods with homogenous compositions through a high-temperature annealing process. Alloy nanorods exhibit strong surface plasmon

resonances with high stability upon etching. Tunable and fascinating optical properties are achieved through controlling over aspect ratios and compositions of the nanorods.

Improved understandings on the properties of resorcinol-formaldehyde (RF) resins will benefit the colloidal synthesis of RF-based nanomaterials. In this study, the chemical stability and the evolution of both surface properties and chemical structures of RF resin spheres are systematically studied, which provide guidance for the rational design and fabrication of various hollow nanostructures. Based on the new understandings, an extension of the surface-protected etching strategy has been adopted for the preparation and engineering of hollow RF nanostructures. A RF-template-engaged redox reaction method is proposed and utilized for rational synthesis of mesoporous hollow manganese oxide nanostructures. Visible resonant Mie scattering properties are theoretically simulated and experimentally demonstrated.

Finally, a couple of novel optical demonstrations based on the design and structural engineering of nanostructures are presented. The first one is the design of plasmonic dichroic film on a mirrored substrate, which has been realized by spray-coating core-shell nanostructures. By structural engineering over the core-shell particles, dichroic film with multi-colors has been successfully created, which holds great potential in anti-counterfeiting. The other one is related to the modulation of light transmittance and the drying process of hollow nanostructures. Au nanoparticles are incorporated into the hollow structures and employed to probe the drying process.

Table of Contents

List of Figures

Figure 4.8 Optical extinction spectra during drying process of (a) Au@TiO_2 yolk-shell structures and (b) Au/TiO_2 shell mixture. The insets in (a) and (b) show the TEM images of the yolk-shell structures and Au/TiO_2 shell mixture, respectively. Dependence of peak position and peak intensity on the drying time. (c) Au@TiO_2 yolk-shell and (d) Au/TiO_2 mixture. (Page 118)

Chapter 1

Overview of Optical Properties of Nanomaterials

1.1 Introduction

Nanostructured materials or nanomaterials, typically being less than 100 nm in length along at least one dimension, have attracted great attention due to their attractive properties introduced by the small size scale.[1-4] It is commonly believed that nanomaterials are cornerstones of nanoscience and nanotechnology. From the viewpoint of fundamental studies and technological advancement, there is a strong demand to better understand the properties of nanomaterials to better harness them for related applications. Compared to their bulk counterparts, the unique features of nanomaterials, such as large surface area, localized surface plasmon resonances, quantum confinement of semiconductors, etc. have opened new horizons for a variety of applications, including catalysis, energy storage, surface enhanced Raman spectroscopy, fluorescence-based sensing, etc.[5-11]

One of the most fascinating and useful aspects of nanomaterials is their optical properties,[12-14] which involve the interaction of electromagnetic radiation with matter. New optical properties arise when the size of particles shrinks to the nanoscale.[6] For instance, when the size is reduced below 10 nm, CdSe nanoparticles (NPs) can exhibit quantum confinement of excitons, producing a size-dependent fluorescence and becoming a “quantum dot”.[15] Similar nanoscale effects can also be seen in noble metal NPs, which exhibit both size and shape dependent optical properties due to the coupling

of plasma oscillations on their surfaces with incident light.[16-18] Indeed, novel optical properties manifest on the nanoscale for metal, semiconductor, and insulator. A famous example utilizing the optical properties of nanomaterials could be dated back to the 4th century when the Romans made the dichroic Lycurgus Cup. The Cup shows a different color depending on whether light is passing through it; red when lit from behind and green when lit from in front, which is now believed to be the unique scattering and absorption properties of Au and Ag NPs embedded in the glass. Nowadays, optical properties of nanomaterials are among the most exploited and useful properties for technological applications, ranging from sensing and detection, optical imaging, light energy conversion, display, photocatalysis, and biomedical treatment. For example, many chemical sensors take advantage of the unique optical properties of nanomaterials, such as surface enhanced Raman scattering and fluorescence.[10]

The optical properties are closely related to the electronic properties as well as the structures of the nanomaterials.[14] Optical nanomaterials, including quantum dots, noble metal NPs, and metamaterials, etc. have attracted tremendous interest from a large community of researchers because they hold huge potential in a variety of applications. Thus, covering all the common types of optical nanomaterials would be beyond the scope of this thesis, so discussion will be focused on a few important categories of nanomaterials relevant to the work presented here.

In this Chapter, I will give an overview on the basic principles behind the optical properties of nanomaterials. First, localized surface plasmon resonances from noble metal nanostructures will be briefly introduced, including the principles and factors affecting

the optical properties. Afterwards, a brief overview on structural color such as photonic crystals and resonant Mie scattering will be presented. In addition, structural engineering of optical nanomaterials will be discussed in the aspect of seed mediated growth and morphological control. Finally, the focus of this thesis as well as general description of each Chapter will be summarized.

1.2 Localized surface plasmon resonances

Localized surface plasmon resonances (LSPRs) arise from the collective oscillation of free electrons in a nanocrystal made of a metal such as Au and Ag in response to the oscillating electric field of the incident light, as illustrated in Figure 1.1.[18, 19] Metallic NPs can be described as a lattice of ionic cores with conduction electrons moving almost freely inside the NPs. Under the irradiation of light, the conduction electrons oscillate coherently due to the oscillating electric field of the light, moving the electrons towards the NP surface. An electric dipole will thus be created with negative charge accumulating on one side and positive charge on the other side. This dipole generates an electric field inside the NP opposite to that the light that will force the electrons to return to the equilibrium position, which is similar to a linear oscillator. If the electrons are displaced from the equilibrium position and the field is removed later, they will oscillate with a certain frequency that is called the resonant frequency. Based on the law of conservation of energy, the incident light extinguishes within a narrow energy range when exciting LSPRs, allowing us to detect LSPRs through optical absorption and scattering spectroscopy.

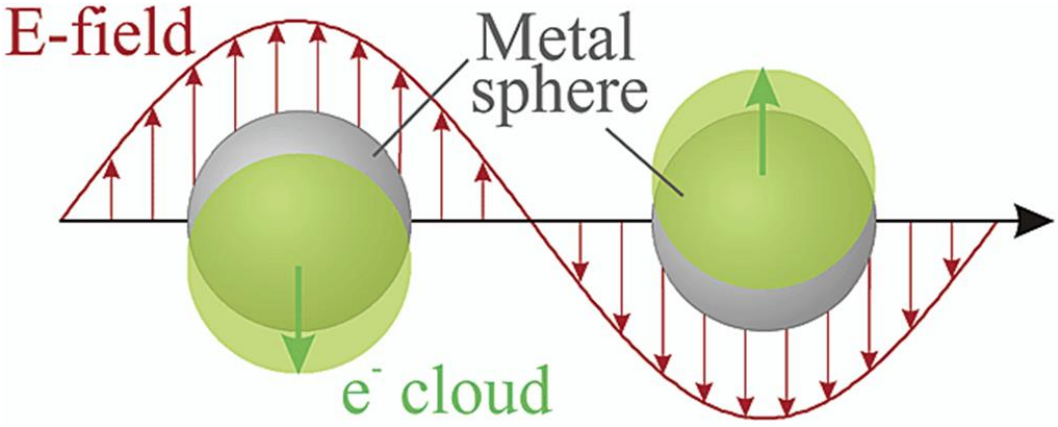

Figure 1.1 Schematic of plasmon oscillation for a sphere, showing the displacement of the conduction electron charge cloud relative to the nuclei. Adapted with permission from ref. 18.

From a more fundamental perspective, there are only two possibilities of interaction of a medium with light, which are scattering and absorption. When light interacts with mass, some of the photons are transmitted (forward scattered), while others are back scattered or absorbed. The optical cross section of a material is a measure of the intensity of the light that is absorbed or scattered by that material. The extinction is the sum of scattering and absorption, so is the extinction cross section. What makes the LSPRs unique are the large extinction cross sections. As illustrated in Figure 1.2, the extinction cross section for 10 nm size metallic NPs could be up to 10 times or even higher than their geometrical section, indicating that the NPs can absorb or scatter photons even away from their physical positions.[19] For instance, the extinction cross section of 10 nm in diameter of Ag NP is 4080 nm^2, while its geometrical section is 78.5 nm^2, indicating over 50 times difference. Noteworthy is that the light absorption is exponentially dependent on the absorption cross section, suggesting a moderate increase in the extinction cross section can lead to a huge enhancement of light absorption.

The LSPR frequency and intensity are found to strongly depend on the size, shape or geometry, dielectric constants of both the metal and the surrounding material, and interparticle distance. The dielectric properties of the materials determine the LSPR band position and intensity. As shown in Figure 1.2, the resonant wavelength varies from different metallic NPs due to their difference in metal dielectric constant. For example, Ag NPs exhibit resonant wavelength at 410 nm while Au NPs show an extinction peak at 520 nm. The LSPR properties are not limited to metal nanostructures. Materials that possess a negative real and small positive imaginary dielectric constant are capable of

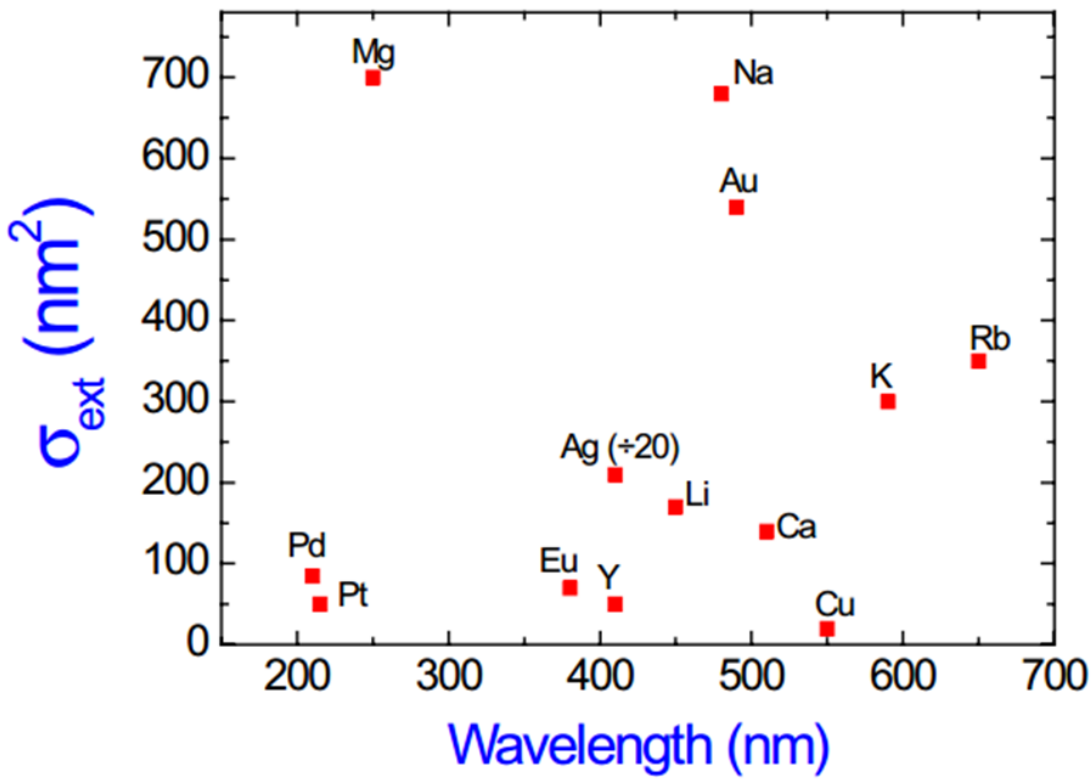

Figure 1.2 Resonant frequency and extinction cross section for metallic NPs with 10 nm size in air. The extinction cross section of Ag has been divided by 20 for a better presentation (the real value is 4080 nm^2). Adapted with permission from ref. 19.

supporting the surface plasmon resonances. Commonly employed plasmonic materials include the noble metals Au and Ag, but more recently copper, aluminium, highly doped oxides and chalcogenides, and graphene.[20] In this thesis, we focus only on the noble metals of Au and Ag nanostructures because the LSPR of Au and Ag are spectrally located in the visible to near-infrared range and they are relatively stable in ambient environments.

The size has a dramatic effect on the LSPR properties. In general, one needs to take the quadrupolar term or multipolar effects into account for a large metal NP, while the small NP can be considered as a dipole. In addition, the LSPRs are also strongly affected by the particle shape or geometry because the charges accumulate at the particle surface. For example, there are two plasmon modes in Au nanorods (NRs). One is the longitudinal LSPR mode associated with the electron oscillations along the length axis, and the other is the transverse LSPR mode excited by light polarized along the transverse direction of the nanorod.

Besides the size and shape effects, the surrounding medium significantly modify the excitation of LSPRs, which will be introduced in Chapter 4 in detail. Briefly, the dielectric function of the surrounding medium alters the geometry of the electric filed at the surface of NPs and the induced polarization of the dielectric medium will partially compensate the charge accumulation due to the movement of conduction electrons in the NPs.[19] As the excitation of LSPRs induces an electric field in the vicinity of the NPs, one can imagine the electric field interactions among NPs when they are close enough. For instance, colloidal Au nanospheres exhibit ruby red color, while assembling those

nanospheres into chain-like structures will cause color change to blue, which is due to the coupling between Au nanospheres.[21]

1.3 Structural color and resonant Mie scattering

To make a material that is colored, one normally uses a dye or pigment. The color produced from dyes or pigments originates from the absorption of light to excite an electron between the ground and excited state of chromophore. In addition to use a dye or pigment for coloration, another way is to make a nanostructure that reflects or scatters light so that waves of certain frequencies can constructively interfere. Those nanostructured materials are said to have structural color. While pigments and dyes degrade and their color fade over time, structural colors can be made resistant to fading because they have a more physical origin that stems from the modulation of photon motions when light travels through the nanostructures.[22] Structural colors are iridescent and metallic, cannot be mimicked by chemical dyes or pigments, and free from photobleaching unlike traditional pigments or dyes. Therefore, structural colors of nanomaterials are of special interest as important chromatic materials. An important class of structural color is photonic crystal structures, which are periodically structured dielectric materials with a regularly repeated modulation of refractive index on a particular length scale, which creates a forbidden gap to prevent propagation of certain wavelengths of light. Responsive photonic crystals, which can change their color in response to external stimuli such as magnetic field, have attracted much attention due to their important uses in areas such as color displays, inks and paints, and many active components in optical devices.[23, 24]

However, the complicated synthesis process of periodic structures limits their practical applications on a large scale. Furthermore, the design of multiple structural colors with a wide viewing angle is also a big problem because the color from Bragg diffraction is largely dependent on the viewing direction, which could limit the applications that require broad viewing angles, such as displays, printed media, optical devices and sensor. As an angle-independent color effect, optical response from resonant Mie scattering of hollow nanostructures attract much attention. In 2009, Ye and co-workers reported that magnetite hollow spheres with a diameter of 650 nm and shell thickness of 40 nm exhibit an unexpected green color, which was interpreted in terms of the Mie scattering on the inhomogeneous and low-density structure of the hollow spheres with a characteristic diameter that is comparable to the wavelength of the visible light.[25] Retsch et al. reported that hollow silica NPs with thin shells also exhibited unexpected colorations such as blue and green when placed on a dark background.[26] The experimentally measured reflectance spectra is in good agreement with the theoretically calculated spectra according to the Mie theory. The transport mean free path of light could be significantly increased, allowing the resonantly scattered light to escape the powder with reduced multiple scattering. The backscattered efficiency is good enough to significantly interact with the incident light, while the transport mean free path has become large enough to allow the resonantly scattered light to escape the powder with minimum multiple scattering. A dark background or black additives are usually required to help visualizing the color and enhance the color contrast by suppressing incoherent and multiple scattering.

1.4 Structural engineering of optical nanomaterials

The LSPR properties of noble metal nanomaterials are highly dependent on their structures, including shape, size and surrounding materials. The structural engineering of metal NPs thus becomes significant to tune their optical properties. One efficient and maybe most common way to tune the structures is through controlled colloidal synthesis.[4] Here in this thesis, colloidal nanostructures of Au and Ag are of particular interest because of their visible-to-near-infrared tunable plasmonic features, high chemical stability, and the enormous success in colloidal synthesis to finely control their growth. In the following part, structural engineering through seeded growth strategy, including the size control over nanospheres and the shape control over nanospheres and nanorods, will be discussed.

Back in 1857, Michael Faraday prepared the first stable suspension of Au colloids by reducing Au chloride with phosphorus in water.[27] Some of his original samples are still preserved and on display at the Faraday Museum in London. One of the most popular protocols for preparing Au nanospheres (~15 nm) is based on the reduction of $HAuCl_4$ by citrate in water, which was first described in 1951 by Turkevitch and is now commonly referred to as the "Turkevitch method".[28] In this method, citrate serves as both a reducing agent and an anionic stabilizer. To produce Au nanospehres with desired sizes, a "seeded growth" strategy, also often referred to as "seed-mediated growth" in literature, was first proposed by Murphy et al.[29, 30] This strategy has been successfully extended to produce various metal NPs of diverse chemical compositions, such as nanospheres, nanocubes, nanorods, nanoplates, and nanowires.[31, 32]

A typical seeded growth method involves the preparation of metal NPs as seeds and subsequent growth in reaction solution composed of metal precursors, reducing agents, and capping agents. Compared with the conventional one-step method, a well-controlled growth step can be separated from the nucleation of the seeds, allowing a better control over the size and size distribution and a better understanding on the shape evolution mechanism. The seeded growth strategy also makes it possible to prepare metal nanocrystals with desired shapes by introducing different capping ligands during the growth stage. Therefore, seeded growth method has been widely used as a versatile tool for rational design and synthesis of metal nanostructures of various compositions and morphologies.

Ideally speaking, the size of Au nanospheres could be simply tuned by controlling the ratio between the seed and the precursor. However, it usually requires multiple steps of growth to achieve a significant size increase as it needs to keep low concentrations of metal precursors to reduce self-nucleation, which takes a great deal of time, energy and labor. Our group have recently developed a one-step seeded growth protocol for the synthesis of Au NPs with tunable diameters from ~10 nm to ~200 nm.[33] In this unique system, self-nucleation is greatly suppressed despite high precursor concentration by stabilizing the metal precursors with a strong coordinating ligand (KI) and an additional capping ligand (PVP). As illustrated in Figure 1.3, seeded growth at high precursor concentrations without self-nucleation can be achieved by stabilizing precursors through complexation with strong ligands, which greatly decreases the concentration of the equilibrium Au^0 "monomers" in the reaction to a value much lower than the nucleation

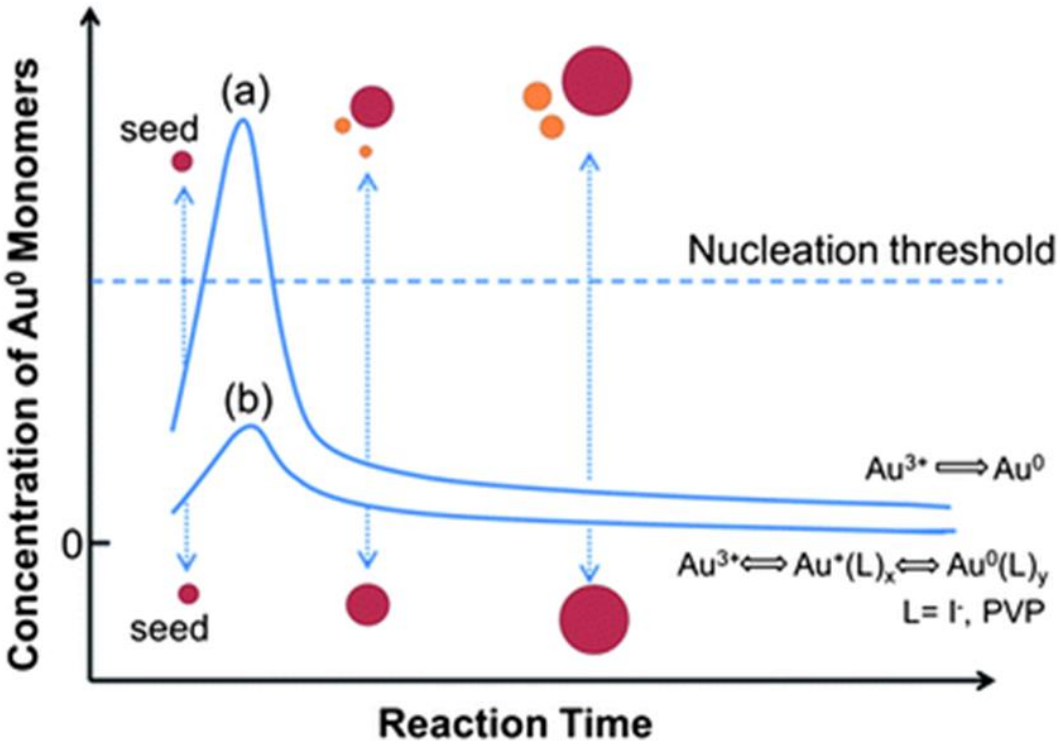

Figure 1.3 Schematic diagram depicting the stages of the growth of Au nanoparticles in a seeded synthesis without (a) and with (b) self-nucleation being suppressed by additional coordinating ligands. Adapted with permission from ref. 33.

threshold.[33] The one-step seeded growth method avoids multiple steps and enables potential large-scale production. Based on a similar concept, monodispersed Ag quasi-nanospheres with size tunable in a range of 19-140 nm through a one-step seeded growth strategy.[34] In this system, acetonitrile is selected as a coordinating ligand to Ag(I) salt to suppress the self-nucleation. In addition, reaction temperature is further controlled to delicately balance the reaction kinetics to suppress the self-nucleation of Ag because the addition of Au seeds significantly accelerates the reduction reaction. By employing this strategy and using Au seeds of different sizes, Au@Ag core/shell nanospheres with a variety of sizes as well as Au-to-Ag ratios could be readily obtained.[35] The conversion of Au@Ag core/shell nanospheres into Ag/Au alloy nanospheres will be discussed in Chapter 3 in detail.

In addition to nanospheres, nanorods have drawn much attention because of their high anisotropy and promising applications in many fields. Impressive progress has been achieved in Au NRs synthesis in the past two decades, including template-directed method, electrochemical method, and seed-mediated method.[36, 37] The most common method is the seed-mediated method, which was developed independently by Murphy et al. and El-Sayed et al.[38, 39] In a typical growth, Au seeds of ~1.5 nm are first prepared by reducing $HAuCl_4$ with $NaBH_4$ in an aqueous cetyltrimethylammonium bromide (CTAB) solution. The growth solution is obtained by reducing Au(III) complex ions to Au(I) complex ions with ascorbic acid also in an aqueous CTAB solution. A certain amount of the seed solution is then added to catalyze the further reduction of Au(I) complex ions to form Au NRs. The addition of $AgNO_3$ into the growth solution can greatly improve the

yields of Au NRs and allow for the rough control of their aspect ratios with unclear mechanisms. In addition, the size and shape of Au NRs can be tailored by carefully adjusting the growth conditions, such as the composition of the surfactant, the pH of the growth solution, and the growth temperature. Recently, Murray's group reported a dramatically improved synthesis of colloidal Au NRs using a binary surfactant mixture composed of CTAB and sodium oleate (NaOL),[40] which will be employed in this thesis. In contrast to Au NRs, which have been greatly explored regarding their synthesis, there has been only limited progress in preparing Ag NRs with uniform shapes, narrow size distributions, and tunable LSPRs. Thanks to the impressive progress in the preparation of Au NRs, the difficulties in direct synthesis of Ag NRs can be circumvented by depositing Ag on the Au NRs to form Au@Ag core/shell NRs. Niidome et al. have successfully prepared Au@Ag core/shell nanocuboids by reducing $AgNO_3$ form Ag shell on Au NRs in cetyltrimethylammonium chloride (CTAC) solutions.[41]

Besides the shape and size control through seeded growth approach, the optical properties of Au and Ag nanostructures can also be structurally engineered by coating a shell layer to form core-shell nanostructures. The shell coating can effectively tune the LSPRs owing to the locally changed dielectric environments. Core-shell nanostructures such as Au@TiO_2 and Ag@Cu_2O have shown fascinating optical properties compared with their core structures.[42] We will discuss in Chapter 4 in detail. In addition to morphology control over metallic nanostructures, structural engineering of dielectric materials can also be employed to tune the structural colors. As mentioned above, the unique structural features of hollow shells with appropriate void space and shell thickness

result in colors based on resonant Mie scattering. The rational design and synthesis of hollow structured materials are thus of great importance, which will be introduced in detail in Chapter 3.

1.5 Focus of this dissertation

The fundamental issues on LSPRs of Au and Ag nanostructures as well as brief overview on structural engineering of optical nanomaterials have been discussed. The essence of this dissertation is related to the rational design, fabrication, and utilization of various optical nanomaterials. This dissertation discusses our efforts in the engineering of optical nanomaterials and their applications in optical devices. It can be divided into three consecutive stages: (1) controllable synthesis of Au/Ag nanostructures with desired morphology and optical properties; (2) improved understanding on the resorcinol formaldehyde resin spheres toward better control over hollow structures; (3) design and fabrication of optical nanomaterials for practical applications based on (1) and (2).

In Chapter 2, fully alloyed Ag/Au nanorods will be demonstrated by adopting a high-temperature annealing approach. Optimized annealing temperature will be obtained and the stability of the obtained Ag/Au alloy nanorods upon chemical etching will be investigated. Tunable LSPR band position and intensity, which are very different from Au nanorods, have been achieved by careful engineering on the rod dimensions and chemical compositions. In addition to the synthetic control over the tuning of LSPR properties, the polarization-dependent property of alloy NRs will be investigated. Finally, colloidal nanoporous Au-Ag alloy nanorods will be fabricated and studied.

Chapter 3 represents a systematic study on the surface properties and structures of resorcinol formaldehyde resin spheres and their use as self-templates and reactive templates. In the introduction part, an overview of hollow structures will be presented. Three parts are divided for better discussions. First, surface charges and chemical structures of resorcinol formaldehyde resin will be characterized, followed by a proposed formation mechanism. Their use as hard templates and coating materials to create novel nanostructures will be discussed. Then, the extension of the surface-protected etching strategy toward hollow resorcinol formaldehyde resin capsules will be presented. Finally, template-engaged redox etching approach will be applied to the synthesis of hollow MnO_2 spheres by using resorcinol formaldehyde resin spheres as reactive templates. Visible resonant Mie scattering of hollow MnO_2 spheres will be also demonstrated.

In Chapter 4, we present two scenarios regarding the structural engineering over nanostructures for optical applications. The LSPR dependence on the surrounding refractive index is first introduced, which is related to all the three scenarios. In the first scenario, a dichroic film on a mirrored substrate is proposed and demonstrated by using metal@shell architectures. Multi-colored dichroic films will be developed by manipulating the core and shell materials. An anti-counterfeiting device will be demonstrated based on the dichroic films. In the second part, the drying process of hollow TiO_2 shells will be investigated by monitoring the transmittance evolution. The LSPR of Au NPs are employed to monitor the drying process by incorporating them into hollow structures. A drying model for the hollow shells is finally proposed.

1.6 References

1. Talapin, D. V.; Lee, J.-S.; Kovalenko, M. V.; Shevchenko, E. V. *Chemical reviews* **2010,** 110, (1), 389-458.

2. Burda, C.; Chen, X.; Narayanan, R.; El-Sayed, M. A. *Chemical reviews* **2005,** 105, (4), 1025-1102.

3. Dahl, M.; Liu, Y.; Yin, Y. *Chemical reviews* **2014,** 114, (19), 9853-9889.

4. Yin, Y.; Alivisatos, A. P. *Nature* **2005,** 437, (7059), 664-670.

5. Chen, X.; Mao, S. S. *Chemical reviews* **2007,** 107, (7), 2891-2959.

6. Alivisatos, A. P. *Science* **1996,** 271, (5251), 933-937.

7. Cao, Y. C.; Jin, R.; Mirkin, C. A. *Science* **2002,** 297, (5586), 1536-1540.

8. Simon, P.; Gogotsi, Y. *Nat Mater* **2008,** 7, (11), 845-854.

9. Arico, A. S.; Bruce, P.; Scrosati, B.; Tarascon, J.-M.; van Schalkwijk, W. *Nat Mater* **2005,** 4, (5), 366-377.

10. Zhong, W. *Analytical and Bioanalytical Chemistry* **2009,** 394, (1), 47-59.

11. Zhang, Q.; Uchaker, E.; Candelaria, S. L.; Cao, G. *Chemical Society reviews* **2013,** 42, (7), 3127-3171.

12. Henry, A.-I.; Bingham, J. M.; Ringe, E.; Marks, L. D.; Schatz, G. C.; Van Duyne, R. P. *The Journal of Physical Chemistry C* **2011,** 115, (19), 9291-9305.

13. Ray, P. C. *Chemical reviews* **2010,** 110, (9), 5332-5365.

14. Zhang, J. Z., *Optical properties and spectroscopy of nanomaterials*. World Scientific: Hackensack, NJ [etc.], 2009.

15. Peng, X.; Manna, L.; Yang, W.; Wickham, J.; Scher, E.; Kadavanich, A.; Alivisatos, A. P. *Nature* **2000,** 404, (6773), 59-61.

16. Willets, K. A.; Van Duyne, R. P. *Annu Rev Phys Chem* **2007,** 58, 267-297.

17. Eustis, S.; El-Sayed, M. A. *Chemical Society reviews* **2006,** 35, (3), 209-217.

18. Kelly, K. L.; Coronado, E.; Zhao, L. L.; Schatz, G. C. *The Journal of Physical Chemistry B* **2003,** 107, (3), 668-677.

19. Garcia, M. A. *Journal of Physics D: Applied Physics* **2011,** 44, (28), 283001.

20. Liz-Marzan, L. M.; Murphy, C. J.; Wang, J. *Chemical Society reviews* **2014,** 43, (11), 3820-3822.

21. Han, X.; Goebl, J.; Lu, Z.; Yin, Y. *Langmuir : the ACS journal of surfaces and colloids* **2011,** 27, (9), 5282-5289.

22. Kim, H.; Ge, J.; Kim, J.; Choi, S.-e.; Lee, H.; Lee, H.; Park, W.; Yin, Y.; Kwon, S. *Nat Photon* **2009,** 3, (9), 534-540.

23. Ge, J.; Hu, Y.; Biasini, M.; Beyermann, W. P.; Yin, Y. *Angewandte Chemie International Edition* **2007,** 46, (23), 4342-4345.

24. Ge, J.; Yin, Y. *Angewandte Chemie International Edition* **2011,** 50, (7), 1492-1522.

25. Ye, Q.-L.; Yoshikawa, H.; Bandow, S.; Awaga, K. *Appl Phys Lett* **2009,** 94, (6), 063114.

26. Retsch, M.; Schmelzeisen, M.; Butt, H.-J.; Thomas, E. L. *Nano Letters* **2011,** 11, (3), 1389-1394.

27. Faraday, M. *Philosophical Transactions of the Royal Society of London* **1857,** 147, 145-181.

28. Turkevich, J.; Stevenson, P. C.; Hillier, J. *Discussions of the Faraday Society* **1951,** 11, (0), 55-75.

29. Jana, N. R.; Gearheart, L.; Murphy, C. J. *Langmuir : the ACS journal of surfaces and colloids* **2001,** 17, (22), 6782-6786.

30. Jana, N. R.; Gearheart, L.; Murphy, C. J. *Chemistry of Materials* **2001,** 13, (7), 2313-2322.

31. Gao, C.; Goebl, J.; Yin, Y. *Journal of Materials Chemistry C* **2013,** 1, (25), 3898-3909.

32. Xia, Y.; Gilroy, K. D.; Peng, H.-C.; Xia, X. *Angewandte Chemie International Edition* **2017,** 56, (1), 60-95.

33. Gao, C.; Vuong, J.; Zhang, Q.; Liu, Y.; Yin, Y. *Nanoscale* **2012,** 4, (9), 2875-2878.

34. Liu, X.; Yin, Y.; Gao, C. *Langmuir : the ACS journal of surfaces and colloids* **2013,** 29, (33), 10559-10565.

35. Gao, C.; Hu, Y.; Wang, M.; Chi, M.; Yin, Y. *Journal of the American Chemical Society* **2014,** 136, (20), 7474-7479.

36. Chen, H.; Shao, L.; Li, Q.; Wang, J. *Chemical Society reviews* **2013,** 42, (7), 2679-2724.

37. Hu, M.; Chen, J.; Li, Z.-Y.; Au, L.; Hartland, G. V.; Li, X.; Marquez, M.; Xia, Y. *Chemical Society reviews* **2006,** 35, (11), 1084-1094.

38. Gole, A.; Murphy, C. J. *Chemistry of Materials* **2004,** 16, (19), 3633-3640.

39. Nikoobakht, B.; El-Sayed, M. A. *Chemistry of Materials* **2003,** 15, (10), 1957-1962.

40. Ye, X.; Zheng, C.; Chen, J.; Gao, Y.; Murray, C. B. *Nano Letters* **2013,** 13, (2), 765-771.

41. Okuno, Y.; Nishioka, K.; Kiya, A.; Nakashima, N.; Ishibashi, A.; Niidome, Y. *Nanoscale* **2010,** 2, (8), 1489-1493.

42. Jiang, R.; Li, B.; Fang, C.; Wang, J. *Advanced Materials* **2014,** 26, (31), 5274-5309.

Chapter 2

Strong, Stable, and Tunable Surface Plasmon Resonances of Fully Alloyed Ag/Au Nanorods

2.1 Introduction

Colloidal Au and Ag nanostructures have been a subject of intensive research for their fascinating localized surface plasmon resonance (LSPR) properties, which arise from the collective oscillations of the free electrons confined to the nanoscale.[1-3] Nanomaterials of Au and Ag have been proven to be good candidates for applications in catalysis,[4] surface enhanced Raman scattering (SERs),[5] biosensors,[6] and plasmonics.[7] The LSPR properties of plasmonic materials strongly depend on their chemical composition, size, shape, local dielectric environment, and electromagnetic interactions with proximate particles. The contents in this Chapter are mainly related to the dependence of elemental composition as well as the shape of metal NPs on the LSPR properties.

In terms of plasmonics, it is important to choose a metal that can support a strong LSPR at the desired resonance wavelength. The ability of a metal nanoparticle to support LSPR is dependent on its dielectric function, which includes a real part and an imaginary part, both of which vary with excitation wavelength.[2] The dielectric function of a material reflects the unique interaction between its electrons and the light. Quality factor is usually used to describe the LSPR strength, where a higher quality factor indicates stronger plasmon resonances.[8] For example, the aluminum only shows large quality factor in the

ultraviolet (UV) region, suggesting aluminum is suitable for UV plasmonics. Among all the plasmonic metals, Ag has the largest quality factor across most of the spectrum from 300 to 1200 nm. Interband transitions, where electrons are excited from the conduction band to higher energy levels, also play an important role in dampening the LSPRs.[9] The interband transitions typically occur at much higher frequencies than the LSPRs. For Au and Cu, those transitions limit the LSPR excitation to wavelengths longer than 500 and 600 nm, respectively.[10]

In addition to the elemental dependence, particle shape also plays an important role in governing the wavelength of LSPR bands. In comparison with spherical ones, nonspherical nanocrystals exhibit anisotropic optical and electronic responses that are determined by their topological aspects. Great effort has therefore been devoted to controlling the shape of noble metal NPs, varying from spheres to rods, cubes, plates, and wires, which greatly broaden the range of the LSPR wavelength. Among those nonspherical NPs, nanorods (NRs), especially Au NRs, have been receiving extensive attention owing to their tunable plasmonic properties and related promising applications in many fields,[11-13] such as photothermal therapy,[11, 14, 15] sensing,[16, 17] SERS,[18] and so forth. There are two plasmon modes in Au NRs. One is the longitudinal LSPR mode associated with the electron oscillations along the length axis, and the other is the transverse LSPR mode excited by light polarized along the transverse direction of the rod. The plasmon wavelength of the longitudinal mode can be synthetically tuned across a broad spectral range, covering the visible and near infrared regions by tailoring their aspect ratios.

Nanocrystals of Ag, which has the largest quality factor across most of the spectrum, have been widely studied and utilized to enhance Raman scattering and fluorescence. Compared with Au NPs, Ag NPs exhibit much stronger electric field enhancements. Simulation results have shown that the field intensity enhancement factors of the Ag NRs are 3.5-6.8 times those of the Au NRs with same size.[19] Moreover, Ag can support LSPR in the near-UV spectral range due to its higher interband transition energy when compared with Au. In fact, plasmon resonances of Ag NRs are able to cover the whole visible spectra, making them promising for applications requiring LSPRs in the visible range, such as visible photocatlytic reactions and magnifying superlens.[20-22] However, there has been only limited progress in preparing Ag NRs with uniform shapes, narrow size distributions, and tunable longitudinal plasmon wavelengths, which would severely hinder the use of their attractive plasmonic properties in many plasmon-based applications. [23-25]

Thanks to the impressive progress in the preparation of Au NRs, the difficulties in direct synthesis of Ag NRs can be circumvented by depositing Ag on the Au NRs to form Au@Ag core/shell NRs.[19, 26] The longitudinal mode of resulted Au@Ag NRs can be finely tailored through varying either the thickness of Ag shell (Ag to Au ratio) or the aspect ratio of core Au NRs. Although Ag NRs have intriguing plasmonic properties, poor chemical and structural stability limits their wide practical applications. The structures and LSPR properties of Ag NPs are subject to changes upon exposing to water, halides, oxidative agents, and UV irradiation.[27-29] For instance, Ag NRs are rather instable and change automatically into nanospheres in aqueous solutions.[23, 30] To this end,

stable Ag NRs, which are resistant to oxidation and morphological changes, are highly desired.

Several methods have been developed in previous studies to stabilize Ag NPs mainly through coating a protective layer such as silica.[31, 32] However, the overlayer is often vulnerable to external etchants and cannot provide sufficient protection. Deposition of Au onto Ag nanocrystals usually causes partial dissolution of Ag due to the replacement reaction between Ag and Au precursors.[33] Replacement reaction-free coating of Au on Ag requires delicate control,[34] while thicker coating of Au will diminish the plasmonic activity of Ag. Therefore, an alternative and perhaps more effective way is to homogeneously alloy Ag with a chemically inert plasmonic metal such as Au. Our group recently demonstrated an effective synthesis strategy based on interfacial atomic diffusion of Ag and Au in Au@Ag core/shell nanospheres.[35] Fully alloyed Ag/Au nanospheres with high compositional homogeneity ensured by annealing at high temperatures have been obtained, which exhibited large extinction cross sections, extremely narrow bandwidths, and remarkable stability in harsh chemical environments. As no conventional surfactants can survive at high temperature such as 1000 °C, a layer of silica is coated on the Au@Ag core/shell nanospheres prior to their annealing to serve as a high-temperature-resistant "surfactant" to prevent particle aggregations.

In this Chapter, the excellent plasmonic property of Ag and the great stability of Au are combined and realized in rods-like nanostructures. More specifically, Au@Ag core/shell NRs are converted into fully alloyed Ag/Au NRs through thermal treatment under the protection of silica to avoid agglomerations. An optimized annealing

temperature has been found to be around 800 °C. Above that temperature, anisotropic NRs tend to fuse into spherical particles, while lower temperature annealing cannot guarantee the chemical stability. The resulted alloy NRs exhibit strong plasmon resonances and superior chemical stability in harsh etchant. In contrast to Au NRs, whose transverse mode is usually located at ~520 nm, our alloy NRs show a tunable LSPR band positions for both transverse mode and longitudinal mode by simply controlling either Ag shell thickness or aspect ratio. Moreover, the peak intensity ratio between the two resonance modes could also be adjusted and the intensity of transverse mode could be even stronger than that of longitudinal mode. The polarization-dependent optical response of the alloy nanorods is also studied by incorporating them within poly(vinyl alcohol) thin films and aligning them by heating and stretching the nanocomposite films, which enables selective excitation of the plasmon modes. In addition to Au/Ag alloy NRs, we also report a dealloying process for the fabrication of porous Au-Ag alloy NRs containing abundant inherent hotspots.

2.2 Experimental

2.2.1 Synthesis of Au NRs and Au@Ag core/shell NRs

Au NRs were prepared using a seed-mediated growth method in a binary surfactant mixture composed of CTAB and NaOL according to a previously reported protocol from Murray's group.[36] In a typical synthesis, 40 mg $HAuCl_4 \cdot 3H_2O$ was used and the obtained Au NRs were concentrated and re-dispersed in 10 ml H_2O. The aspect ratios can be tuned by adjusting the pH value of the growth solution as well as the amount of seed solution. Au@Ag core/shell NRs were synthesized through controlled

epitaxial growth of Ag on Au NRs in the presence of CTAC as a surface capping ligand according to a reported procedure with slight modification.[26] Specifically, each aliquot (0.64 ml) of the Au NRs solution was centrifuged and re-dispersed into 8 ml of aqueous CTAC solutions (0.08 M). Subsequently, various amount (0.2 ml to 2 ml) of $AgNO_3$ (0.01 M) were added into the Au NRs dispersions, followed by the addition of ascorbic acid solutions (0.1 M). The volume of the ascorbic acid solution was a half of the $AgNO_3$ solution. The resultant solutions were kept in a water bath at 65 °C for 3 h. Au@Ag core/shell NRs were collected and re-dispersed in 4 ml of H_2O.

2.2.2 Silica coating

Au@Ag core/shell NRs can be easily coated with silica via a modified Stober method. Typically, to the 4ml of the core/shell nanoparticle solution was added 60 ml of isopropanol and 8 ml of water. After that, 120 µl of TEOS and 3 ml of diethylamine were added in sequence under stirring, and the reaction was allowed to proceed for 2 h. A colloid of Au@Ag@SiO_2 NPs was obtained after centrifugation and redispersion.

2.2.5 Annealing and silica removal

In a standard process, the Au@Ag@SiO_2 NPs were dried and annealed at 800 °C for 3 h in a tubular furnace under the protection of an Ar atmosphere. The sample after annealing was re-dispersed in 40 ml of a water solution containing 1.25 wt% PVP (Mw=10 000), 50 mM diethylamine, and 5 mM NaOH, and the resulting dispersion was refluxed for 1 h in a nitrogen atmosphere to ensure complete removal of the silica shell and restabilization of the alloy NRs with PVP. Ag/Au alloy NRs were then collected by centrifugation and re-dispersed in water.

2.2.5 Synthesis of porous Au-Ag nanorods by dealloying

In a typical dealloying process, Ag/Au alloy NRs were dispersed in an aqueous CTAC solution (2 ml, 0.01 M), followed by adding a diluted $FeCl_3$ solution (3 ml, 5 mM). After 5 min of reaction, the resulting porous Au-Ag NRs were collected by centrifugation and re-dispersed in water.

2.2.6 Characterizations

The transmission electron microscopy (TEM) images were taken with a Philips Tecnai 12 transmission electron microscope operating at 120 kV. Ultraviolet-visible-near IR (UV-vis-NIR) spectra for Au NRs were measured with a Cary 500 UV-Vis-NIR spectrophotometer. All other spectra were measured with an Ocean Optics HR2000 CG-UV-NIR high resolution spectrometer.

2.3 Results and discussion

Figure 2.1a outlines the general synthesis strategy for the preparation of Ag/Au alloy NRs, which involves coating of the Au@Ag core/shell NRs with a protection layer of silica and subsequent annealing under an Ar atmosphere at high temperature. In a typical process, Au NRs were prepared using a seed-mediated growth method in a binary surfactant mixture composed of CTAB and NaOL according to a previously reported protocol from Murray's group.[36] Their average length and diameter determined from the TEM characterization (Figure 2.1b) are 101.6 ± 7.5 nm and 18.2 ± 1.1 nm, respectively. Au@Ag core/shell NRs were then prepared through controlled epitaxial overgrowth of Ag on Au NRs in the presence of CTAC as a surface capping ligand. As shown in Figure 2.1 b and c, after deposition of Ag, cylindrical Au NRs are converted to uniform cuboidal

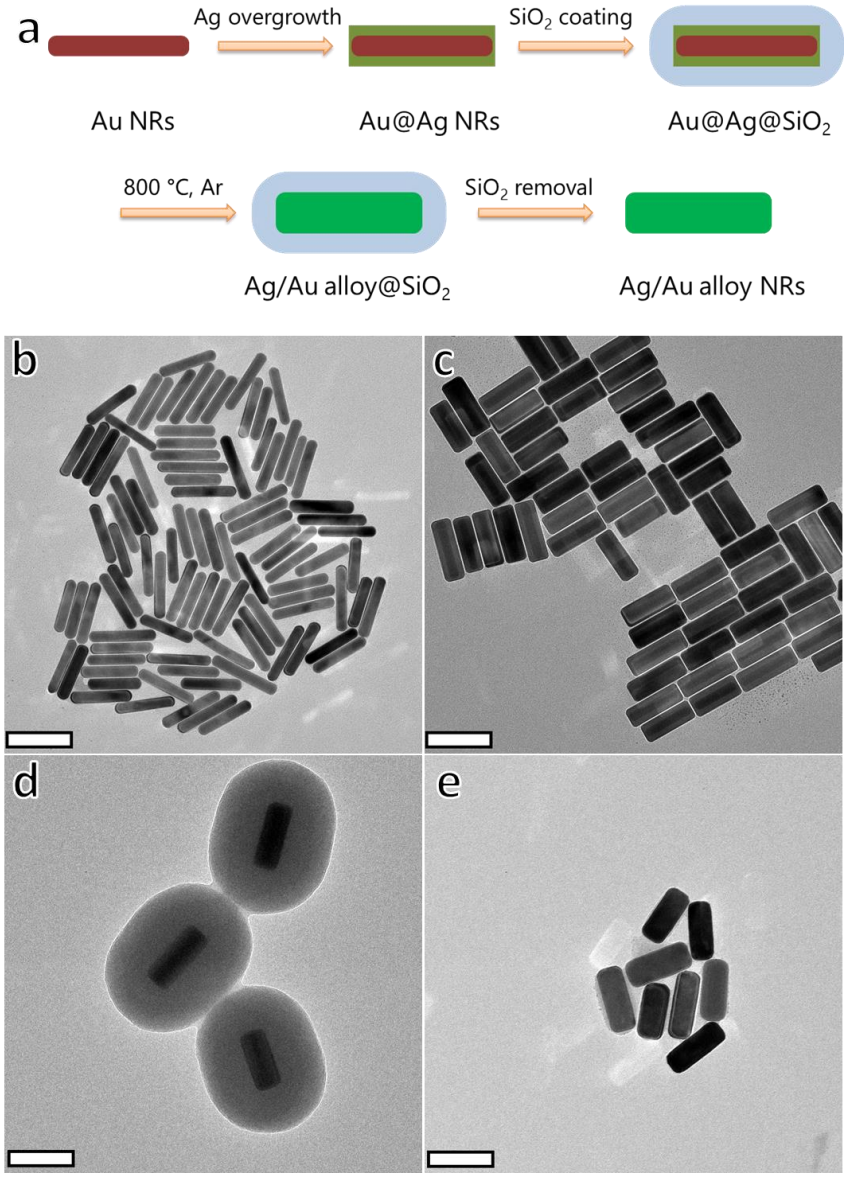

Figure 2.1 (a) Schematic illustration for the preparation of Ag/Au alloy NRs. TEM images showing the rod-like morphology at different synthesis stages, (b) Au NRs, (c) Au@Ag core/shell nanocuboids, (d) Au@Ag@SiO_2, and (e) Ag/Au alloy NRs. The scale bar is 100 nm.

Au@Ag core/shell NRs with sharp edges and corners. The Ag shells at the sides of the NRs are observed to be thicker than those at the ends, resulting in a decrease in the aspect ratio from 5.59 ± 0.50 to 2.77 ± 0.22. A layer of silica that serves as high-temperature-resistant "surfactant" was then coated on the core/shell NRs (Figure 2.1d), following which Au@Ag@SiO_2 NRs were annealed at 800 °C for 3 hours to ensure homogeneously mixing of Au and Ag at the atomic scale.[35] After silica removal in a solution of NaOH, a stable colloid of Ag/Au alloy NRs were finally obtained (Figure 2.1e).

Figure 2.2 shows the corresponding photograph and UV-vis-NIR extinction spectra of the Ag/Au alloy NRs and their synthesis intermediates. After Ag deposition, the color of NRs changed from red to yellow-green, and further changed to striking blue-green after alloying process. In the corresponding extinction spectra, the longitudinal plasmon resonance mode of Au NRs is located at 996 nm, with a full width at half maximum (FWHM) of ~165 nm, indicating the narrow size distribution of NRs. After epitaxial growth of Ag, the core/shell NRs exhibit four distinct peaks at 727, 434, 391, and 344 nm, which are ascribed to the longitudinal and transverse dipolar plasmon modes, and two octupolar plasmon modes, respectively.[19] The blue-shift of the resonance peak from 996 nm to 727 nm is caused by the increased effect of the optical properties from Ag as well as the decreased aspect ratios. The longitudinal resonance mode is further blue-shifted to 663 nm after high-temperature alloying, which could be attributed to both the permittivity changes upon alloying and slight reduction of aspect ratios. In the low-energy region of the spectrum, a sharp mono-peak at 421 nm evolves, which belongs

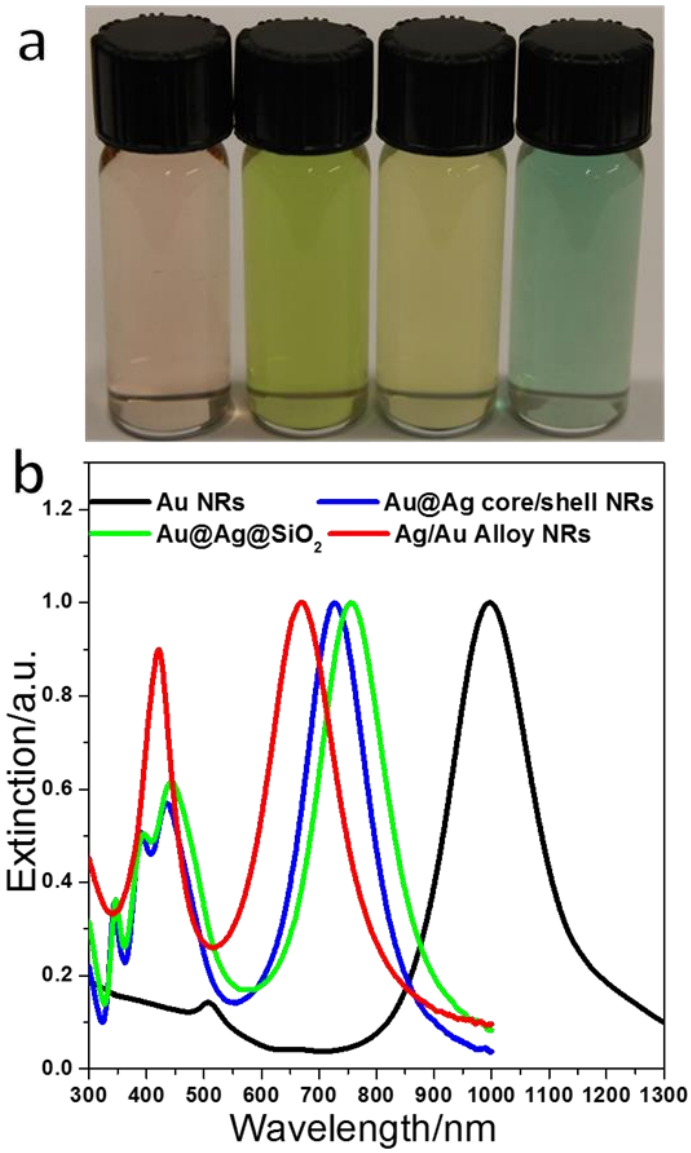

Figure 2.2 (a) Photograph showing solutions containing Au NRs, Au@Ag core/shell NRs, Au@Ag@SiO_2, and Ag/Au alloy NRs (left to right) and (b) the corresponding normalized extinction spectra of the samples as shown in Figure 2.1.

to the transverse dipolar mode of alloy NRs, indicating high-temperature annealing could reshape the cuboidal NRs. Noteworthy is that both resonance peaks in this work are very sharp with FWHM of ~136 and ~58 nm for longitudinal and transverse mode respectively, which is different from previously reported Ag NRs exhibiting broad extinction peaks due to wide size distribution and faceted geometry.[25, 37]

Compared with the preparation of Ag/Au alloy nanospheres, relatively lower annealing temperature was adopted in this work.[35] Different from isotropic nanospheres, anisotropic Au and Ag NRs tend to fuse into spherical particles at higher annealing temperatures. It was also reported that Ag NRs and nanocubes would undergo sublimation under high-temperature treatment, while Au NRs would shrink and fuse into spheres.[22, 38, 39] As can be seen from the TEM image in Figure 2.3a, annealing at 1000 ℃ led to shrinkage of NRs into spherical particles. Alloy nanospheres and Au nanospheres due to the possible sublimation of Ag are both present in the sample. The shape transformation as well as the incomplete shape indicates the loss of Ag and the structure instability of NRs at 1000 °C. When annealing at 900 ℃, alloy NRs are obtained but with one incomplete end due to the sublimation of Ag atoms. Alloying at 800 °C yields complete NRs with no apparent sublimation of Ag. Those results are consistent with the UV-vis-NIR extinction spectra in Figure 2.3d. Only one plasmon peak is exhibited for the sample annealed at 1000 °C because of the spherical shape of the fused metal particles. Compared with the spectra of alloy NRs annealed at 800 °C, the blue-shift of the LSPR peaks for the alloy NRs obtained at 900 ℃ suggests the shortening of NRs in length and the decreasing in aspect ratios. Annealing at lower temperature such as 650 °C could also

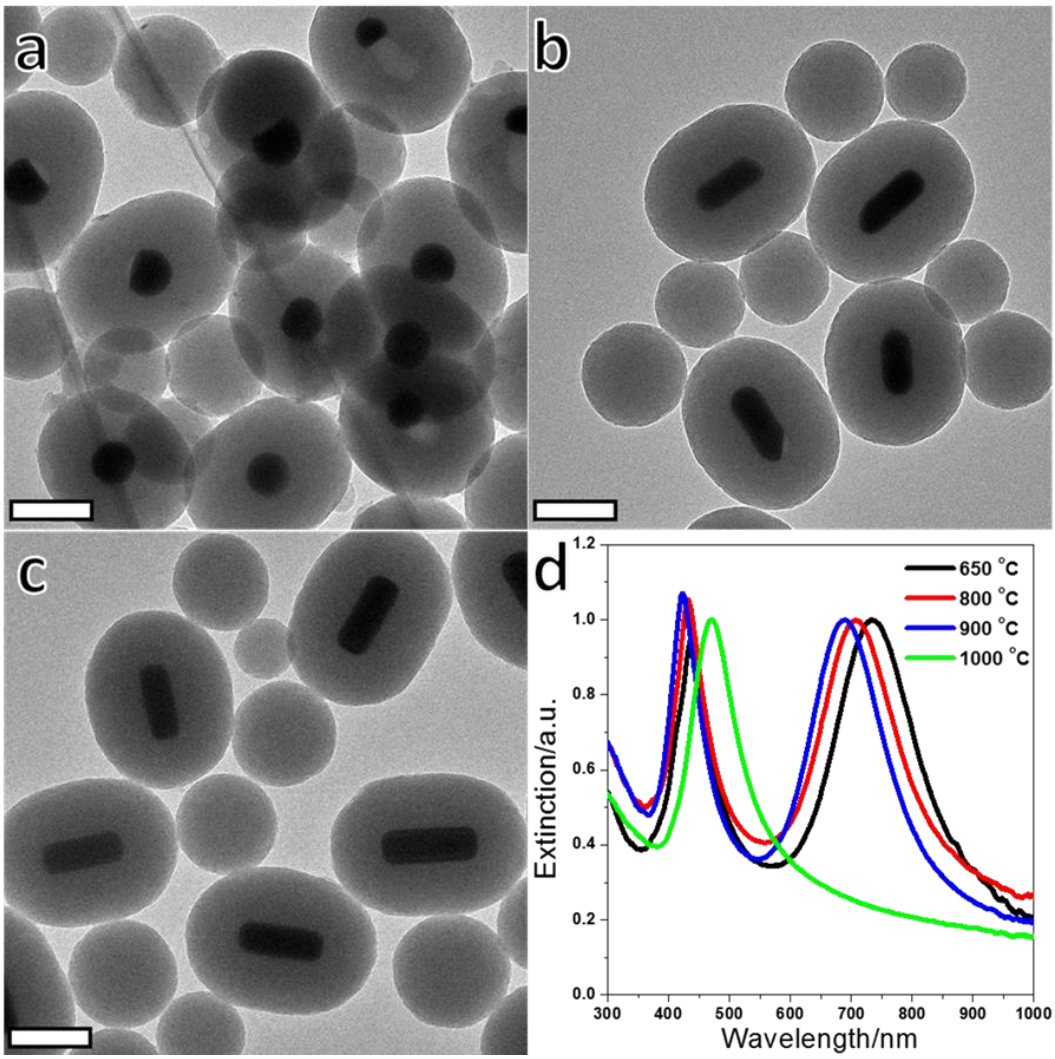

Figure 2.3 TEM images showing the sample of Ag/Au alloy@SiO2 obtained at various temperatures, (a) 1000 °C, (b) 900 °C, and (c) 800 °C. (d) The corresponding normalized extinction spectra. The scale bar is 100 nm.

increase the diffusion rates of Ag and Au atoms and thus facilitate the alloying process. However, our previous work on the alloyed nanospheres suggests higher temperature treatment would benefit the chemical stability of the resultant alloy NPs.[35] To this end, we choose an intermediate temperature of 800 °C for the thermal annealing of NRs. Alloy NRs obtained at that temperature are 105.3 ± 8.9 nm long and 44.7 ± 4.5 nm wide. Compared with the core/shell NRs (108.3 ± 6.8 nm in length and 39.1 ± 2.0 nm in diameter), the aspect ratio slightly shrank from 2.77 ± 0.22 to 2.38 ± 0.32 after heat treatment.

Besides their strong LSPRs, the Ag/Au alloy NRs also displayed excellent stability against chemical etching in a strong oxidative environment. The chemical stability of Au@Ag core/shell NRs and Ag/Au alloy NRs were examined in a mixture of H_2O_2 and ammonia by monitoring their LSPRs band changes. The mixed solvent of H_2O_2 (0.5 M) and ammonia (0.4 M), in which H_2O_2 plays a role in oxidizing Ag while ammonia accelerates the dissolution of Ag by forming soluble $[Ag(NH_3)_2]^+$ complexes, is believed to be a harsh etchant to rapidly dissolve metallic Ag (within 1 s).[35, 40] As depicted in Figure 2.4a, the optical features of Au@Ag core/shell NRs quickly vanished upon exposure to the etchant, leaving behind characteristic extinction peaks only from Au NRs. Dramatic decreases in peak intensities in Figure 2.4a, on the other hand, confirmed that Ag could support much stronger LSPRs than Au as same number of NRs occurred in the solution. Upon high-temperature alloying, those NRs could survive in the strong oxidative etchant with only minor losses in plasmon band intensities (Figure 2.4b). After 12 h of etching, the peak intensities were well maintained at 92% and 90% of the original

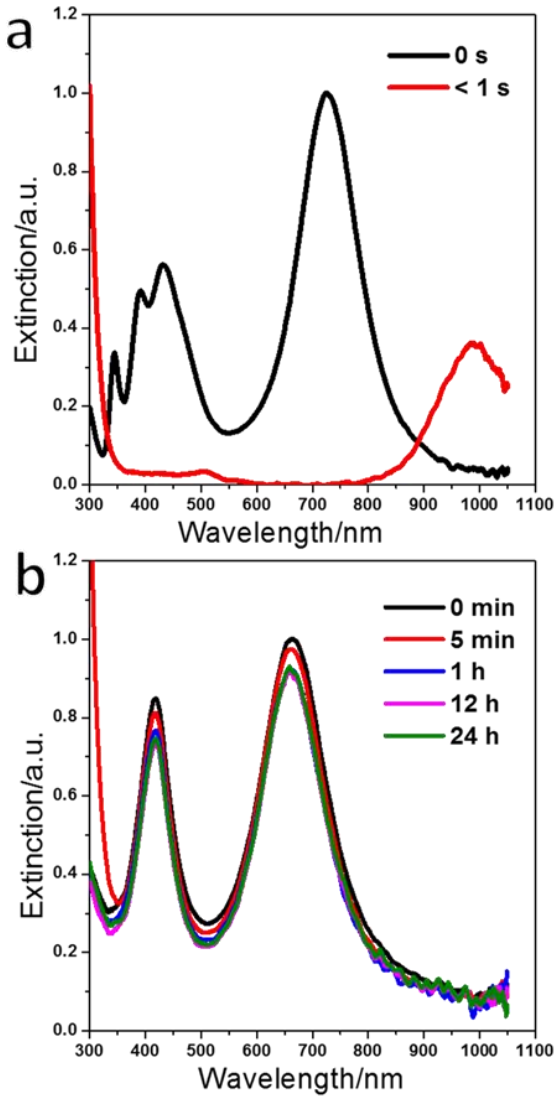

Figure 2.4 UV-vis-NIR spectra showing the chemical stability of (a) Au@Ag core/shell NRs and (b) Ag/Au alloy NRs in a harsh etchant solution which contains H_2O_2 (0.5 M), $NH_3 \cdot H_2O$ (0.4 M), and PVP (surfactant, 0.5 wt %, Mw = 10 000). Initial spectra of the NRs (labeled as 0 s or 0 min in the Figure) were recorded in the absence of H_2O_2 and $NH_3 \cdot H_2O$, with their volumes made up by water.

values with no further decay within additional 12 h for longitudinal and transverse plasmon modes, respectively. Apparently, the more Ag that are present in the alloy particles, the less stable they will be. Therefore, in the later discussion, we only focus on the tunability of LSPR band positions for alloy NRs regardless of their stability.

As LSPR band positions are determined by both the elemental composition and aspect ratio of NRs, LSPR modes of the resultant alloy NRs could be readily controlled by varying the ratio between the amounts of Ag precursor and Au NRs involved in a synthesis. As shown in Figure 2.5 a, c, e, and g, various Au@Ag core/shell NRs were obtained by adding different amounts of $AgNO_3$ into reaction solutions containing the same number of Au NRs. Those core/shell cuboidal NRs were all converted to alloy NRs in the absence of sharp corners and edges (Figure 2.5 b, d, f, and h) through high-temperature annealing. As plotted in Figure 2.5 i, the thickness of Ag shells at the sides increased more than that at the end, resulting in that aspect ratios of the core/shell NRs decreased gradually from 4.01 to 3.32, 2.38, 2.29, and 2.16, as the amounts of $AgNO_3$ was increased from 400 to 800, 1200, 1600, and 2000 μl, respectively. Their plasmonic properties are plotted in Figure 2.6. As shown in Figure 2.6a and b, the Au@Ag core/shell NRs exhibited four resonance peaks while their alloy counterparts showed two distinct plasmon bands. The longitudinal plasmon bands of the resultant alloy NRs underwent a blue-shift from 736 nm to 648 nm as increasing the amount of Ag, which promises a simple yet effective way to tune resonant peaks due to wide size distribution and faceted geometry. As depicted in Figure 2.6c, the longitudinal extinction peaks in

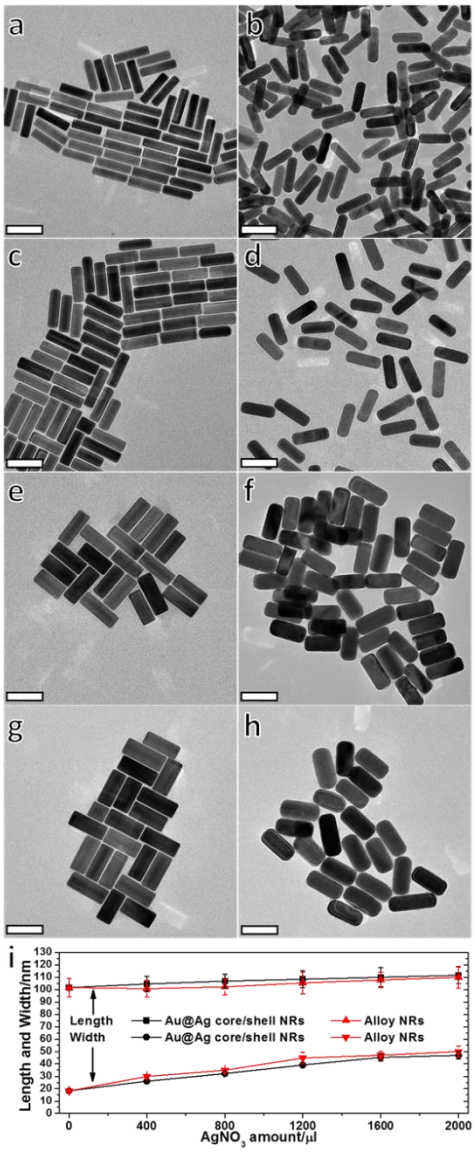

Figure 2.5 TEM images of Au@Ag core/shell NRs (a, c, e, and g) and the corresponding Ag/Au alloy NRs (b, d, f, and h). The core/shell NRs (a, c, e, and g) were produced from the growths with 400, 800. 1600, and 2000 μl of $AgNO_3$ solution at 0.01 M, respectively. The scale bar is 100 nm. (i) Plot of length and width as a function of the volume of $AgNO_3$ precursor.

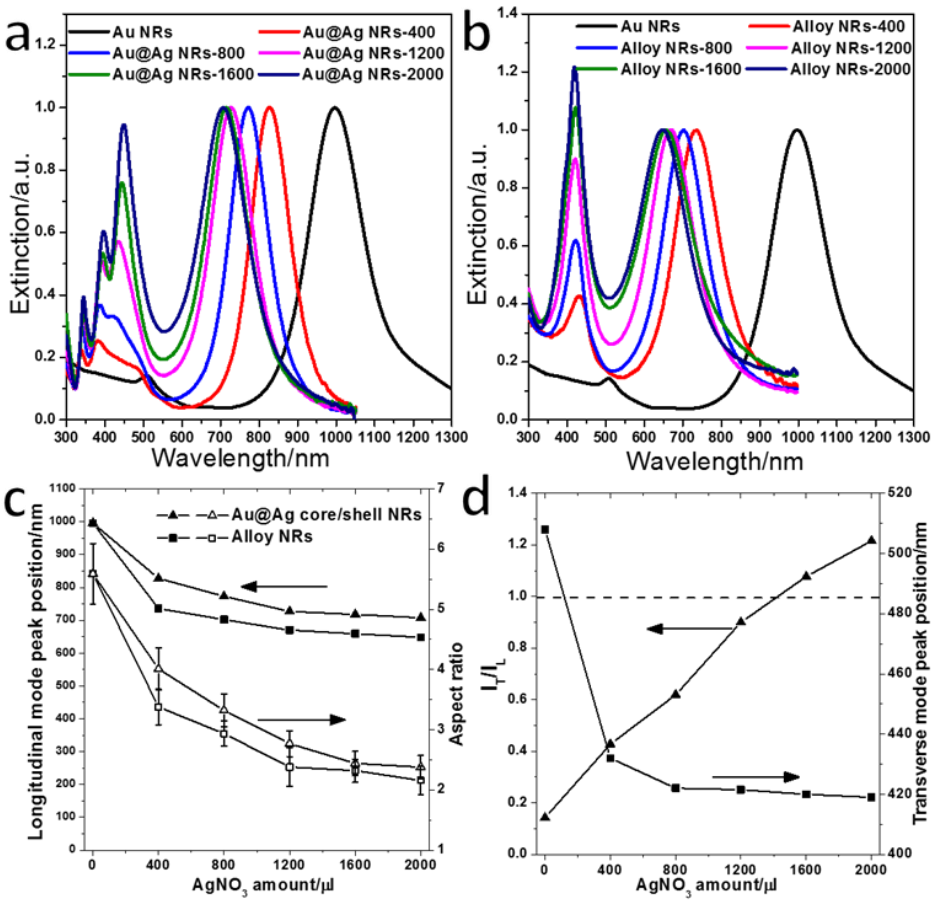

Figure 2.6 UV-vis-NIR extinction spectra for (a) Au@Ag core/shell NRs and (b) Ag/Au alloy NRs shown in Figure 2.1 and Figure 2.5. Dependence of resonance peak positions, peak intensity ratios, and aspect ratios on the volume of the $AgNO_3$ precursor. (c) Longitudinal peak positions and aspect ratio versus the volume of the $AgNO_3$ precursor. (d) Transverse peak positions and intensity ratio between transverse and longitudinal modes versus the volume of the $AgNO_3$ precursor. The dash line in (d) indicates the equal intensities of the transverse and longitudinal modes.

both cases blue-shifted first rapidly and then slowly, which is consistent with the variations of aspect ratio.

It is known that the plasmon wavelength of the longitudinal mode for Au NRs can be synthetically tuned through simply tailoring their aspect ratios.[11, 41] The transverse plasmon band is however insensitive to the size of Au NRs, resulting in less tunability on the peak positions. On the other hand, the peak intensity of the transverse mode is much weaker than that of the longitudinal mode (with a ratio of 0.14 to 1 in this work) for the case of Au NRs. In contrast to Au NRs, the transverse mode of our Ag/Au alloy NRs can be adjusted in the aspect of peak positions as well as peak intensities as shown in Figure 2.6 b and d. With an increase of Ag amount, the peak positions can be altered from ~510 to ~420 nm owing to the joint contribution from Au and Ag, suggesting great tunability on both transverse and longitudinal modes. Thanks to the smaller dielectric function of elemental Ag than that of elemental Au, Ag is able to support stronger plasmon resonances. As indicated in Figure 2.6 b and d, the peak intensity ratios between transverse and longitudinal band (I_T/I_L) increase gradually from 0.14 to 1.22 when increasing the Ag volumes, indicating our Ag/Au alloy NRs can support strong transverse mode with comparable to or even higher intensities than longitudinal one.

Considering that the longitudinal mode is greatly dependent on the aspect ratio of NRs, we can further tune the LSPR modes through starting with Au NRs with different aspect ratios. As an example, Au NRs (~78 nm in length and ~25 nm in diameter) with aspect ratio of ~3.16 were successfully prepared (Figure 2.7a). As shown in Figure 2.7b and c, shorter Au@Ag core/shell NRs could be readily converted into alloy NRs with an

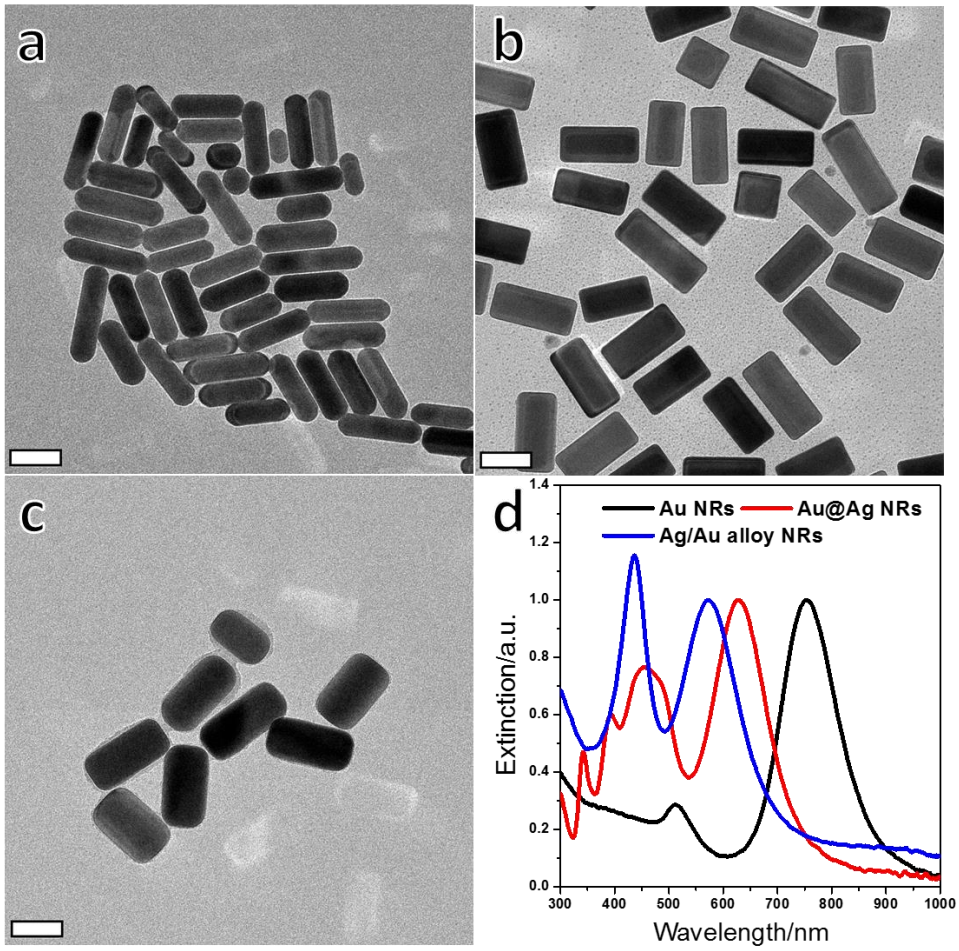

Figure 2.7 TEM images for (a) Au NRs, (b) Au@Ag NRs, and the resultant (c) Ag/Au alloy NRs; The scale bar is 50 nm. (d) the corresponding UV-vis-NIR extinction spectra.

aspect ratio of ~1.86. The longitudinal extinction peaks blue-shifted from ~754 nm to ~628 nm after overgrowth of Ag and further moved to ~571 nm upon thermally alloying (Figure 2.7d). These results suggest that the resulted alloy NRs in this work could exhibit plasmon modes through the whole visible spectrum with narrow extinction peaks.

Polarization effects provide a useful method for modulating the optical response of light in nanorods.[42] The polarization-dependent optical response of Au NRs has been widely explored.[42-44] Polarized light can be used to excite separately the longitudinal or transverse LSPR mode of a nanorod if the rods are macroscopically oriented. For colloidal suspensions of pure nanorods, one will always observe an average over the possible orientation with both longitudinal and transverse resonance bands in the spectrum. Our group have previously reported the dynamic and reversible tuning of the plasmonic property of Au NRs by controlling their orientation using external magnetic fields. The magnetic orientation control enables instant and selective excitation of the plasmon modes of AuNRs through the manipulation of the field direction relative to the directions of incidence and polarization of light. However, transverse mode of Au NRs limits the modulation of light at ~520 nm. Unlike Au NRs, our alloy NRs showed tunable transverse peak positions between ~510 and 420 nm, allowing broader modulation of light. As one demonstration, alloy NRs were homogeneously incorporated within PVA thin films according to previous reports. When stretching the composite thin films, the alloy NRs tend to align in the stretched direction driven by the elongation of the PVA polymer molecules. Under normal light illumination, both plasmon modes are excited for stretched composite films. As shown in Figure 2.8, the two plasmon modes can be

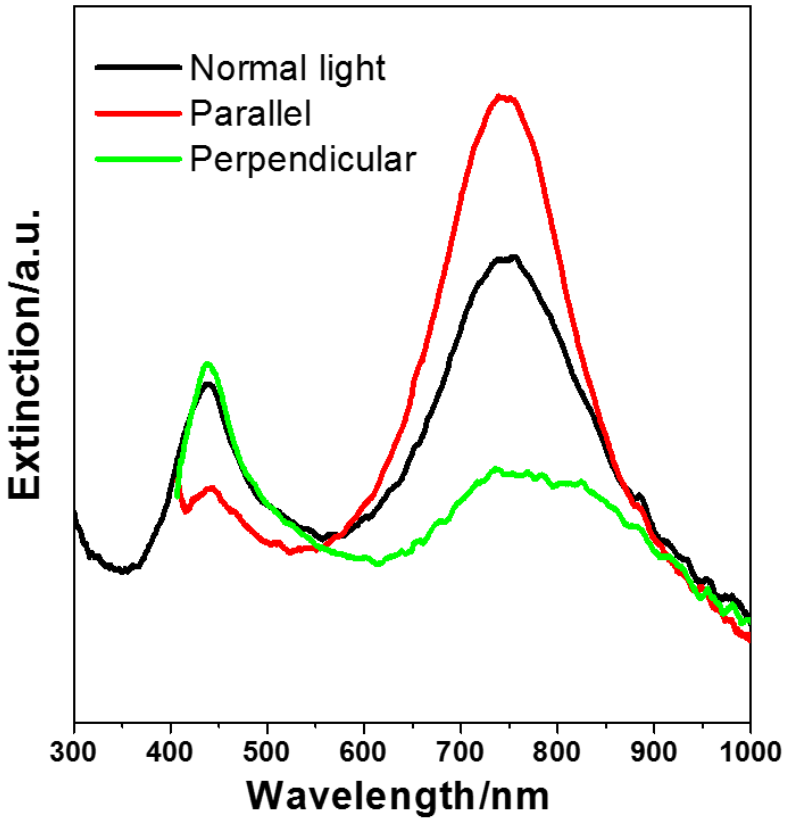

Figure 2.8 UV-vis -NIR extinction spectra of PVA films containing Ag/Au alloy NRs: stretched with normal light (black), stretched with parallel (red) and perpendicular polarization (green).

selectively excited under illumination of polarized light. The longitudinal mode is selectively excited when the polarized light is parallel to the stretch direction, whereas the transverse one (~425 nm) is excited when the polarized light is perpendicular to the stretch direction.

Nanoporous Au NPs have attracted great attention owing to their unique porous structures and widespread applications such as SERS and catalysis.[45-47] Porous Au NPs are usually prepared on the substrate by first patterning Au-Ag alloy nanostructures followed by a chemical or electrochemical dealloying process, which may make it difficult to achieve large-scale production for many practical applications. It is thus highly desirable to develop a robust colloidal synthesis method for large-scale fabrication of nanoporous Au particles. We have previously reported a dealloying process for the fabrication of porous Au-Ag alloy NPs containing abundant inherent hotspots, which were encased in ultrathin hollow silica shells so that the need of conventional organic capping ligands for stabilization is eliminated, producing colloidal plasmonic NPs with clean surface and thus high accessibility of the hotspots.[48] The dealloying process was completed in a concentrated nitric acid, which is a strong oxidizer and may be harder to control the etching of Ag. Here we choose a relatively mild etchant, $FeCl_3$, to convert the Ag/Au alloy NRs into porous Au-Ag NRs. $FeCl_3$ is believed to oxidize metallic Ag to form AgCl precipitates, which can be washed away by CTAC solution or NaCl solution.[40] As shown in Figure 2.9a, the bright green color of alloy NRs changed to dark greenish color after adding the etchant of $FeCl_3$. The two strong LSPR peaks of alloy NRs disappear after dealloying and the resultant colloidal porous Au-Ag NRs exhibit

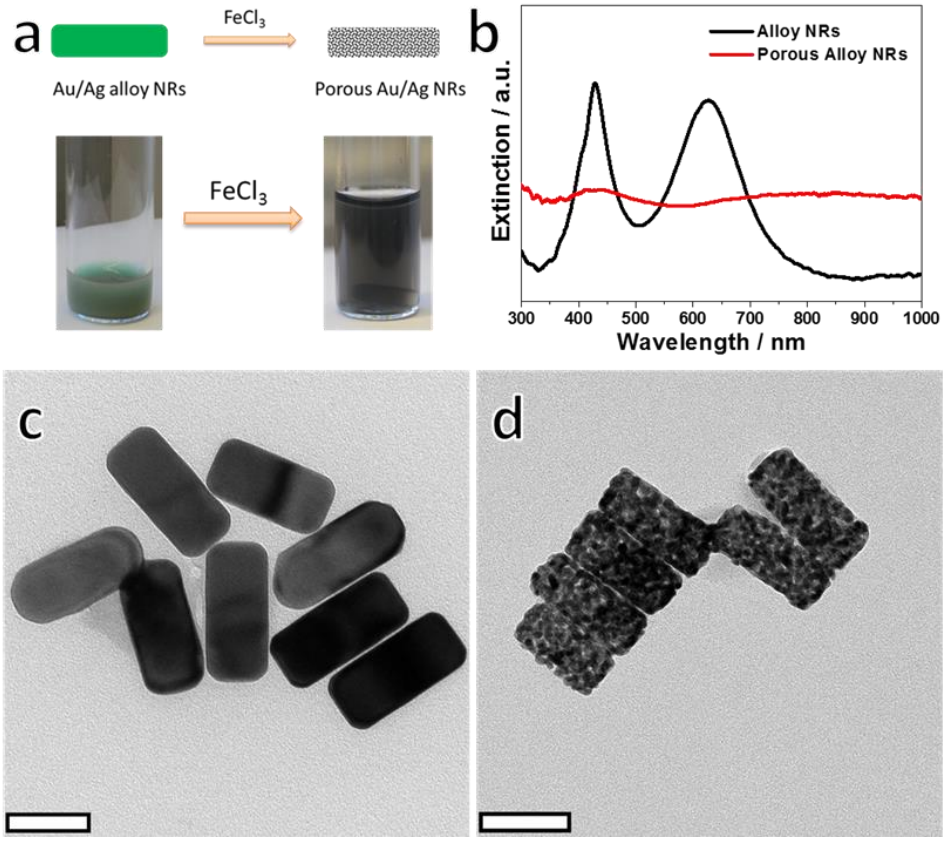

Figure 2.9 (a) Schematic illustration for the preparation of porous Au-Ag alloy NRs and the corresponding digital images showing the color of the dispersions; (b) UV-vis-NIR extinction spectra for alloy NRs and porous alloy NRs; (c) and (d) TEM images showing Ag/Au alloy NRs and porous Au-Ag alloy NRs, respectively. The scale bar is 50 nm.

strong scattering across the UV-vis spectra with no apparent extinction peaks (Figure 2.9b). Figure 2.9c and d shows the TEM images of alloy NRs and porous NRs, respectively. The average diameter decreases from 42 nm to 35 nm and the average length decreases from 89 nm to 80 nm, indicating the shrinkage of the NRs after dealloying, which is consistent with the literature report.[48] In addition to SERS, the colloidal porous Au-Ag NRs may find use in drug delivery and optical coherent tomography because of their porous structure and fascinating optical properties.

2.4 Conclusion

In conclusion, fully alloyed Ag/Au NRs combining the excellent plasmonic property of Ag and the great stability of Au have been demonstrated by a high-temperature annealing process. Compared with Au@Ag core/shell NRs, the resultant alloy NRs exhibit significantly improved stability against harsh corrosive environment. Their aspect ratios and thus the longitudinal LSPR peak positions could be readily tuned by either varying the ratio between the amounts of Ag precursor and Au NRs involved in a synthesis or starting with Au NRs of different aspect ratios, while the peak positions of the transverse mode could also be easily adjusted between ~510 nm and ~420 nm. In comparison with Au NRs, our alloy NRs showed widely tunable peak intensity ratios between the transverse and longitudinal modes. In addition, we further demonstrated the polarization-dependent optical properties of the alloy NRs, which can bring modulation of light with broader range. Considering the strong, stable, and highly tunable longitudinal and transverse LSPR properties, our alloy NRs hold potential in both fundamental spectroscopic studies that combine both molecular and plasmon resonance

effects, and many plasmonic applications, such as solar energy conversion, photothermal therapy, and plasmon enhanced fluorescence. Our ongoing work has shown that the alloy NRs exhibit higher photothermal heating efficiency than Au NRs with minimal cytotoxicity. This high-temperature annealing strategy may be served as a general method to fabricate alloy NPs such as Pt, Pd, and Cu to produce unique optical responses and high-performance catalysts. In addition, we have also developed a colloidal route toward the synthesis of porous Au-Ag alloy NRs with high-density of coupling spots by dealloying the Ag/Au alloy NRs in an etchant of $FeCl_3$ solution.

2.5 References

1. Daniel, M.-C.; Astruc, D. *Chemical reviews* **2004,** 104, (1), 293-346.

2. Rycenga, M.; Cobley, C. M.; Zeng, J.; Li, W.; Moran, C. H.; Zhang, Q.; Qin, D.; Xia, Y. *Chemical reviews* **2011,** 111, (6), 3669-3712.

3. Hu, M.; Chen, J.; Li, Z.-Y.; Au, L.; Hartland, G. V.; Li, X.; Marquez, M.; Xia, Y. *Chemical Society reviews* **2006,** 35, (11), 1084-1094.

4. Hashmi, A. S. K.; Hutchings, G. J. *Angewandte Chemie International Edition* **2006,** 45, (47), 7896-7936.

5. Willets, K. A.; Van Duyne, R. P. *Annu Rev Phys Chem* **2007,** 58, 267-297.

6. Hong, Y.; Huh, Y.-M.; Yoon, D. S.; Yang, J. *Journal of Nanomaterials* **2012,** 2012, 13.

7. Liz-Marzan, L. M.; Murphy, C. J.; Wang, J. *Chemical Society reviews* **2014,** 43, (11), 3820-3822.

8. LeRu, E. C.; Etchegoin, P. G. *Principles of Surface-Enhanced Raman Spectroscopy: And Related Plasmonic Effects* **2009**, 1-663.

9. Perner, M.; Bost, P.; Lemmer, U.; von Plessen, G.; Feldmann, J.; Becker, U.; Mennig, M.; Schmitt, M.; Schmidt, H. *Phys Rev Lett* **1997,** 78, (11), 2192-2195.

10. Wang, H.; Tam, F.; Grady, N. K.; Halas, N. J. *The Journal of Physical Chemistry B* **2005,** 109, (39), 18218-18222.

11. Huang, X.; Neretina, S.; El-Sayed, M. A. *Advanced Materials* **2009,** 21, (48), 4880-4910.

12. Chen, H.; Shao, L.; Li, Q.; Wang, J. *Chemical Society reviews* **2013,** 42, (7), 2679-2724.

13. Xia, Y.; Xiong, Y.; Lim, B.; Skrabalak, S. E. *Angewandte Chemie International Edition* **2009,** 48, (1), 60-103.

14. Huang, X.; El-Sayed, I. H.; Qian, W.; El-Sayed, M. A. *Journal of the American Chemical Society* **2006,** 128, (6), 2115-2120.

15. Abadeer, N. S.; Murphy, C. J. *The Journal of Physical Chemistry C* **2016,** 120, (9), 4691-4716.

16. Wang, L.; Zhu, Y.; Xu, L.; Chen, W.; Kuang, H.; Liu, L.; Agarwal, A.; Xu, C.; Kotov, N. A. *Angewandte Chemie International Edition* **2010,** 49, (32), 5472-5475.

17. Vigderman, L.; Khanal, B. P.; Zubarev, E. R. *Advanced Materials* **2012,** 24, (36), 4811-4841.

18. Alvarez-Puebla, R. A.; Agarwal, A.; Manna, P.; Khanal, B. P.; Aldeanueva-Potel, P.; Carbó-Argibay, E.; Pazos-Pérez, N.; Vigderman, L.; Zubarev, E. R.; Kotov, N. A.; Liz-Marzán, L. M. *Proceedings of the National Academy of Sciences* **2011,** 108, (20), 8157-8161.

19. Jiang, R.; Chen, H.; Shao, L.; Li, Q.; Wang, J. *Advanced Materials* **2012,** 24, (35), OP200-OP207.

20. Li, B.; Gu, T.; Ming, T.; Wang, J.; Wang, P.; Wang, J.; Yu, J. C. *Acs Nano* **2014,** 8, (8), 8152-8162.

21. Smolyaninov, I. I.; Hung, Y. J.; Davis, C. C. *Science* **2007,** 315, (5819), 1699-1701.

22. Huang, J.; Zhu, Y.; Liu, C.; Zhao, Y.; Liu, Z.; Hedhili, M. N.; Fratalocchi, A.; Han, Y. *Small* **2015,** 11, (39), 5214-5221.

23. Jana, N. R.; Gearheart, L.; Murphy, C. J. *Chemical Communications* **2001**, (7), 617-618.

24. Luo, M.; Huang, H.; Choi, S.-I.; Zhang, C.; Silva, R. R. d.; Peng, H.-C.; Li, Z.-Y.; Liu, J.; He, Z.; Xia, Y. *Acs Nano* **2015,** 9, (10), 10523-10532.

25. Pietrobon, B.; McEachran, M.; Kitaev, V. *Acs Nano* **2009,** 3, (1), 21-26.

26. Okuno, Y.; Nishioka, K.; Kiya, A.; Nakashima, N.; Ishibashi, A.; Niidome, Y. *Nanoscale* **2010,** 2, (8), 1489-1493.

27. Jiang, X.; Zeng, Q.; Yu, A. *Langmuir : the ACS journal of surfaces and colloids* **2007,** 23, (4), 2218-2223.

28. An, J.; Tang, B.; Zheng, X.; Zhou, J.; Dong, F.; Xu, S.; Wang, Y.; Zhao, B.; Xu, W. *The Journal of Physical Chemistry C* **2008,** 112, (39), 15176-15182.

29. Zhang, Q.; Ge, J.; Pham, T.; Goebl, J.; Hu, Y.; Lu, Z.; Yin, Y. *Angewandte Chemie* **2009,** 121, (19), 3568-3571.

30. Damm, C.; Segets, D.; Yang, G.; Vieweg, B. F.; Spiecker, E.; Peukert, W. *Small* **2011,** 7, (1), 147-156.

31. Sotiriou, G. A.; Sannomiya, T.; Teleki, A.; Krumeich, F.; Vörös, J.; Pratsinis, S. E. *Advanced Functional Materials* **2010,** 20, (24), 4250-4257.

32. Xue, C.; Chen, X.; Hurst, S. J.; Mirkin, C. A. *Advanced Materials* **2007,** 19, (22), 4071-4074.

33. Murshid, N.; Gourevich, I.; Coombs, N.; Kitaev, V. *Chemical Communications* **2013,** 49, (97), 11355-11357.

34. Yang, Y.; Liu, J.; Fu, Z.-W.; Qin, D. *Journal of the American Chemical Society* **2014,** 136, (23), 8153-8156.

35. Gao, C.; Hu, Y.; Wang, M.; Chi, M.; Yin, Y. *Journal of the American Chemical Society* **2014,** 136, (20), 7474-7479.

36. Ye, X.; Zheng, C.; Chen, J.; Gao, Y.; Murray, C. B. *Nano Letters* **2013,** 13, (2), 765-771.

37. Wiley, B. J.; Chen, Y.; McLellan, J. M.; Xiong, Y.; Li, Z.-Y.; Ginger, D.; Xia, Y. *Nano Letters* **2007,** 7, (4), 1032-1036.

38. Khalavka, Y.; Ohm, C.; Sun, L.; Banhart, F.; Sönnichsen, C. *The Journal of Physical Chemistry C* **2007,** 111, (35), 12886-12889.

39. Ding, Y.; Fan, F.; Tian, Z.; Wang, Z. L. *Small* **2009,** 5, (24), 2812-2815.

40. Lu, X.; Au, L.; McLellan, J.; Li, Z.-Y.; Marquez, M.; Xia, Y. *Nano Letters* **2007,** 7, (6), 1764-1769.

41. Link, S.; Mohamed, M. B.; El-Sayed, M. A. *The Journal of Physical Chemistry B* **1999,** 103, (16), 3073-3077.

42. Pérez-Juste, J.; Rodríguez-González, B.; Mulvaney, P.; Liz-Marzán, L. M. *Advanced Functional Materials* **2005,** 15, (7), 1065-1071.

43. Wang, M.; Gao, C.; He, L.; Lu, Q.; Zhang, J.; Tang, C.; Zorba, S.; Yin, Y. *Journal of the American Chemical Society* **2013,** 135, (41), 15302-15305.

44. van der Zande, B. M. I.; Pagès, L.; Hikmet, R. A. M.; van Blaaderen, A. *The Journal of Physical Chemistry B* **1999,** 103, (28), 5761-5767.

45. Ding, Y.; Kim, Y. J.; Erlebacher, J. *Advanced Materials* **2004,** 16, (21), 1897-1900.

46. Xu, C.; Su, J.; Xu, X.; Liu, P.; Zhao, H.; Tian, F.; Ding, Y. *Journal of the American Chemical Society* **2007,** 129, (1), 42-43.

47. Qian, L. H.; Yan, X. Q.; Fujita, T.; Inoue, A.; Chen, M. W. *Appl Phys Lett* **2007,** 90, (15), 153120.

48. Liu, K.; Bai, Y.; Zhang, L.; Yang, Z.; Fan, Q.; Zheng, H.; Yin, Y.; Gao, C. *Nano Letters* **2016,** 16, (6), 3675-3681.

Chapter 3

Colloidal Resorcinol Formaldehyde Resin Spheres: beyond Stöber Synthesis

3.1 Introduction

Colloidal synthesis routes are believed to be a superior approach for the preparation of nanostructured materials with precise control over the morphology and composition, narrow size distribution, complex architectures, and multi-functionality.[1-3] In addition, colloidal nanomaterials are handled in solutions and are easily incorporated into applications in which dispersability is required. Last but not the least, the low cost and easy scalability through common chemistry equipment allows for the mass production of colloidal nanoparticles for commercialization. With the development of various colloidal synthetic strategies over the past few decades, researchers are able to produce a widespread of nanomaterials with various controllable morphologies, including solid and hollow nanoparticles in different dimensions, such as nanospheres and nanoshells, nanorods and nanotubes, etc.[4] In contrast to their solid counterparts, hollow nanostructures, owing to the combination of shells and void spaces, offer additional properties, such as large surface area, low density, and high loading capacity, that can be well utilized for rational design of novel functional materials toward many desired applications, including energy storage, photothermal therapy, nanoreactors, catalysis, and so forth.[4-7]

Three major categories of synthetic approaches for hollow nanostructures are usually divided, namely (1) hard templating method, (2) soft templating method, and (3) self-templating method.[4, 5] Several self-templating approaches have been developed based on different principles, including Ostwald ripening, the Kirkendall effect, galvanic replacement, surface-protected etching, and so on. Thus, covering all the synthetic strategies would be beyond the scope of this thesis, so discussion will center on both hard templating method and surface-protected etching approach that are relevant to the work presented here.

Hard templating method is conceptually straightforward. Typically, hard templates are first synthesized, followed by coating with a layer of targeted materials. After selective removal of the core templates and/or post-treatment, hollow nanostructures are then obtained. A surface modification step changing the surface functionality is usually required to achieve a successful coating. Silica is one of the most commonly employed hard templates due to low cost, high uniformity, and tunable size. Colloidal silica spheres with size ranging from 50 nm to 2 μm are usually prepared through Stöber method by hydrolyzing silica precursor tetraethyl orthosilicate (TEOS) in a mixture solvent of ethanol and water in the presence of ammonia solution.[8] To facilitate the coating process, the surface property of silica can be easily modified with various functional groups, including amine, carboxylate, siliane, etc.[4] HF and NaOH are two mostly used acid and base etchant, respectively, to remove silica template.

TiO_2 is considered to be one of the most useful semiconducting metal oxides and has been fervently investigated over the past few decades due to its applications in

sensing, energy storage, and photocatalysis.[9-11] One effective way to enhance the performances (e.g. photocatalytic, electrochemical, etc.) of TiO_2 is to produce hollow structures with high surface area and pore volume.[12-16] Hollow TiO_2 spheres can be synthesized by templating against colloidal silica spheres. With hydroxypropyl cellulose (HPC) as the surfactant, a layer of amorphous titania is deposited on the silica surface to form SiO_2@TiO_2 nanocomposites through the sol-gel reaction of titanium tert-butoxide (TBOT).[13] The silica template is then removed in an aqueous solution of NaOH, resulting a hollow structure of amorphous TiO_2. Post-treatment such as acid washing and calcination produces well-defined hollow TiO_2 spheres with high surface area and mesoscale pores in shells. Our group also demonstrated a 'silica-protected calcination' process, in which SiO_2@TiO_2 nanocomposites were calcined under the protection of a silica layer that limits the growth of TiO_2 and produces mesoscale porosity.[13, 17]

Hollow nanostructures with carbon shells have attracted considerable attention in catalysis and energy storage because of the unique properties of carbon shells, such as high surface area, high structural and mechanical stability, and good electrical conductivity. To produce hollow carbon spheres, the coating of silica templates with appropriate carbon precursors is a very effective strategy. Many attentions have been paid to nanostructured resorcinol-formaldehyde (RF) resins as a precursor of carbon materials. Since Lu and co-workers' seminal report on the synthesis of monodisperse RF resin colloidal spheres through an extended Stöber process in 2011, RF resin has been widely used to make core-shell nanocomposites because of the simple setup and excellent reproducibility.[18] Our group has developed a general sol-gel process to form a coating of

RF resin on inorganic nanostructures of various compositions and morphologies.[19] By modifying the silica surface with a cationic surfactant, cetyltrimethylammonium bromide (CTAB), RF resin can absorb onto silica spheres and form a uniform shell. SiO_2@RF core@shell composites can be readily converted into SiO_2@C by heating at a high temperature in an inert atmosphere (e.g. N_2). The as-obtained SiO_2@C composites could be readily converted into hollow carbon shells through a simple NaOH etching process. In addition to templating against silica spheres, hollow carbon shells with tubular structures have also been synthesized by employing rod-like nickel-hydrazine complexes as hard template, followed by etching the core in HCl solution.[20]

Direct synthesis without the need of additional templates is preferred in practical applications due to significantly reduced production cost and the ease of scaling up.[4, 21, 22] In contrast to hard templating methods, the templates used in self-templating methods are not only the templates used to create inner hollow structures, but also the integrant composition of the outer shells. Our group introduced the concept of 'surface-protected etching' in 2008, which involves enhancing the relative stability of the surface layer of a single-component nanostructure to make it more stable than the interior and subsequent preferential etching of interior material using an appropriate etching agent.[23, 24] For instance, sol-gel derived solid silica spheres are coated with PVP, whose carbonyl groups can form strong hydrogen bonds with the hydroxyl groups on the silica surface and thus protect the near surface layer. Hollow silica spheres with porous shells are produced by selectively etching the interior of the silica spheres using NaOH. Our group also demonstrated the preparation of TiO_2 microcapsules by heating sol-gel-derived TiO_2

microspheres with poly(acrylic acid) (PAA) in a diethylene glycol (DEG) solution. In this case, DEG acted as an etching agent to transform TiO_2 into soluble titanium glycolate, while PAA served as a cross-linker to connect adjacent NPs into a stable shell. By rationally choosing the reaction components, many hollow nanostructures, such as Prussian blue and Cu_2O, have been realized using the concept of surface-protected etching.[25, 26]

Hollow nanostructures possess fascinating properties such as large surface area, low density, abundant inner void space, and reduced length for both mass and charge transport. The presence of nanoscale hollow interiors with functional shells endows them with technological significance in energy storage and conversion, phtocatalysis, gas sensing, and biomedicine.[4, 5] For example, the above mentioned mesoporous TiO_2 hollow nanostructures with high surface area showed significantly enhanced photocatalytic activity when used as photocatalysts for the degradation of Rhodamine B under UV irradiation.[12] As an anode material, porous TiO_2 shells with precisely controlled carbon incorporation, which combines the advantages of porous shells (beneficial to the diffusion of the lithium ions) and high conductivity of carbon materials, exhibited significantly improved rate capability and cycling performance for lithium ion batteries.[27]

'Mold clay to form a bowl. It is the empty space which makes the bowl useful.' The proverb from Laozi, an ancient Chinese philosopher, expresses the essence of using the inner void space for multiple applications, including nanoreactors and photonics. By taking advantage of the void space, our group developed a general method for the synthesis of noble metal nanorods, such as Au, Ag, Pt, and Pd.[28] The rod-like void space

in silica nanotubes, which are synthesized by templating against nickel-hydrazine nanorods, provides a versatile platform for the preparation of nanorods. After gold seeds loading, seeded growth of noble metals, and removal of silica shells, high-quality metal nanorods with tunable aspect ratios could be readily obtained, which proves the empty space making silica nanotubes useful. In addition to the utilization of hollow nanostructures as nanoreactors, the void space can also bring attractive optical properties. Optical response from resonant Mie scattering of hollow nanostructures attract much attention. Hollow silica nanoparticles with thin shells exhibited unexpected colorations such as blue and green when placed on a dark background.[29] The experimentally measured reflectance spectra is in good agreement with the theoretically calculated spectra according to the Mie scattering model. The transport mean free path of light could be significantly increased, allowing the resonantly scattered light to escape the powder with reduced multiple scattering. The visible Mie scattering phenomena can also be observed for hollow magnetite spheres and hollow titania spheres.[30, 31] A dark background is usually required to absorb the forward scattered light, making the back scattered light with better contrast. Hollow magnetite spheres showed bright green color in the absence of dark background as the intrinsic color of magnetite is black itself. Our group have demonstrated a series of hollow TiO_2 shells with different void spaces showed various bright colors such as blue and green by incorporating small amount of carbon derived from HPC surfactant.

Since the pioneering work reported by Werner Stöber and his team in 1968, the so-called Stöber method has been the most widely used sol-gel approach to produce

colloidal silica spheres with controllable particle size and narrow size distribution.[8] In a typical Stöber process, tetraethyl orthosilicate (TEOS) is hydrolyzed and subsequently condensed in alcohol/water mixture in the presence of ammonia as a catalyst. In addition, the Stöber method has also been widely explored to form silica coating on various colloidal nanoparticles to enhance their chemical and colloidal stability. RF resin polymers are highly crosslinked and have served as excellent precursors for carbon materials.[32] RF resin derived carbon materials have exhibited attractive properties such as low cost, high surface areas, and remarkable electrical conductivity, leading to intensive studies in the fields of energy storage and catalysis.[32] Pekala and co-workers are among the first to report the synthesis of RF aerogels via organic sol-gel procedure which is analogous to silicate sol-gel process.[33] Recently, Lu and co-workers have further demonstrated that monodispersed polymeric spheres of RF resin can be successfully fabricated by an extension of the Stöber method owing to their similar sol-gel chemistries.[18] In addition to the synthesis of colloidal RF spheres, coating of RF resin on different colloidal nanostructures have also been realized by modifying the surface charge of the core materials using positively charged ligands such as CTAB.[19] As tons of studies have been conducted on colloidal silica, it is thus possible to gain a more rigorous understanding on colloidal RF particles by comparing the two systems. Furthermore, from the viewpoint of fundamental research, it is highly desirable to further investigate the similarities and differences beyond Stöber process.

In contrast to the one-step Stöber process for silica colloids, RF resin spheres are usually prepared first at room temperature and subsequently heated to form crosslinked

polymers. The subsequent gelation process includes the condensation reaction to form methylene and methylene ether bridged compounds.[32] However, the properties for the RF colloidal spheres obtained before and after crosslinking have not been well compared and reported to date. With new impetus towards carbon based nanomaterials for energy conversion and storage, it is therefore both timely and necessary to examine the properties in more detail with the goal of obtaining improved control over the RF structures.

In this Chapter, we first investigate the synthesis and surface properties of RF spheres through a comprehensive study, as described in Section 3.3. This significantly refined understanding allows us to better control the coating process. In Section3.4, we report an extension of the surface-protected etching process toward hollow RF capsules. In Section 3.5, we describe a template-engaged method which allows fast and facile preparation of hollow MnO_2 spheres, which exhibit bright colors due to the resonant Mie scattering.

3.2 Experimental

3.2.1 Synthesis of RF resin spheres

Colloidal RF resin spheres were synthesized based on the extension of Stöber method developed by Lu's group with some modifications. In a typical synthesis of RF spheres with size of 380 nm in diameter, 20 mg of resorcinol was dissolved in 28 ml of water, followed by adding 28 µl of formaldehyde solution. Ammonia aqueous solution (100 µl, 2.8%) was subsequently added to initiate the reaction. After 12 h of reaction at room temperature, colloidal RF spheres were obtained and re-dispersed in 20 ml of water

after centrifugation, which is denoted as w-RF (weakly crosslinked RF). To further crosslink the RF spheres, colloidal RF dispersion was refluxed at 100 °C for 12 h, which is then referred to as s-RF (strongly crosslinked RF). RF spheres with other sizes can be obtained following the protocols from literature.

3.2.2 Synthesis of TiO_2 and MnO_2 hollow spheres

TiO2 coating on RF spheres was made using an established procedure.[16] Briefly, colloidal RF spheres was washed with ethanol three times and re-dispersed in 20 ml of ethanol. To 5 ml of the RF/ethanol dispersion a mixture of ethanol (15 ml) and acetonitrile (7 ml) was added and mixed under vigorous stirring. After adding 0.2 ml of concentrated ammonia, a mixture of TBOT (0.2 ml), ethanol (3 ml), and acetonitrile (7 ml) was injected into the mixture. After 2 h of reaction, the RF@TiO_2 core-shell composites were collected by centrifugation, washed with ethanol, and re-dispersed in water. The RF templates were easily removed in an aqueous NaOH solution at room temperature.

RF@MnO_2 core-shell structures were prepared based on a template-engaged redox etching strategy. The as-prepared RF spheres were dispersed in 40 ml of water and mixed with a specific amount of aqueous $KMnO_4$ solution (0.2 M) under vigorous stirring. The redox reaction was continued for 4 h in order to make the reaction as complete as possible. The composites were collected by centrifugation, washed with water, and re-dispersed in water. Hollow MnO_2 spheres were obtained by etching away the RF template by NaOH at room temperature.

3.2.3 RF coating on silica and bowl-like RF capsules

RF coating on various nanostructures were prepared per a reported procedure with some modifications.[19] SiO_2 spheres with various sizes were prepared through a modified Stöber method. In a typical synthesis of silica spheres with size of 360 nm in diameter, 4.5 ml TEOS was injected into a mixture of 61.75 ml of ethanol, 24.75 ml of deionized water, and 9 ml of $NH_3 \cdot H_2O$ at room temperature under magnetic stirring. After reacting for 2 h, the colloidal spheres were collected by centrifugation, re-dispersed in 10 ml deionized water. The particle size could be tuned by changing the concentration of ammonium hydroxide as well as the solvent ratio. To form a complete RF coating on the silica spheres, to 0.5 ml of the above colloidal silica dispersion PVP solution (0.5 wt%, 10 ml) was added and stirred overnight to allow adsorption onto the silica surface. The solution was then washed and re-dispersed in 10 ml deionized water. In a typical RF coating process, the PVP coated silica spheres (10 ml) was added to a solution with resorcinol (0.02 g), formaldehyde (28 µl), and water (18 ml). The solution was stirred for ten minutes and an aqueous ammonia solution (2.8%, 0.1 ml) was added and the solution was stirred for 12 h at room temperature or 2 h at 50 °C. The SiO_2@RF composites were then collected by centrifugation, washed with water three times, and re-dispersed in water (20 ml). For poly-condensation of the RF layer, the SiO_2@RF water dispersion was refluxed for 4 h. To obtain the RF capsules, the silica core was removed by etching with a NaOH solution (1 ml, 2.5 M) at room temperature for 8 h.

3.2.4 Synthesis of FeOOH nanorods and FeOOH@RF core-shell structures

The synthesis of FeOOH nanorods is based on a previous report with small modifications.[34] Typically, 7.776 g of anhydrous $FeCl_3$ were dissolved in 80 mL water. The solution was added into 450 μL of 37% HCl and then centrifuged at 11000 rpm for 3 min for the removal of unsolvable precipitates. The purified solution was heated to 98 C in a 100 mL three-neck flask with refluxing and was then maintained for 16 h. The solid product was collected by centrifugation after the reaction and washed by water for several times. 50 mg of as-prepared FeOOH nanorods was dispersed in 20 ml of water, and 1 mL 0.1M PAA solution was added for the surface modification of nanorods. After overnight stirring, the nanorods were recovered by centrifugation and were re-dispersed in 10 ml of water. In a typical RF coating process, the PAA modified FeOOH nanorods (10 ml) was added to a solution with resorcinol (0.02 g), formaldehyde (28 μl), and water (18 ml). The solution was stirred for ten minutes and an aqueous ammonia solution (2.8%, 0.1 ml) was added and the solution was stirred for 12 h at room temperature or 2 h at 50 °C. The FeOOH@RF composites were then collected by centrifugation and re-dispersed in water (20 ml). The dispersion was refluxed for 4 h to further crosslink the RF polymer layer. To obtain the tubular RF structures, the FeOOH nanorods were removed by etching with HCl at room temperature for 12 h.

3.2.5 Synthesis of $Au@SiO_2$ and $Au@SiO_2$@RF core-shell structures

Au nanoparticles were prepared using the Turkevich method.[35] Briefly, 18 mg of hydrogen tetrachloroaurate trihydrate was dissolved in 30 ml of water and the solution was heated to reflux under magnetic stirring, followed by quick injection of 1 ml of

freshly prepared trisodium citrate aqueous solution (3 wt%). The refluxing was continued for 30 min and then the solution was cooled to room temperature. An aqueous solution of PVP (3 ml, 12.8 mg/ml) was added to the solution. The mixture was kept at room temperature for overnight under magnetic stirring, allowing PVP molecules to attach to Au nanoparticles. The PVP modified Au nanoparticles were then collected by centrifuging at 11,000 rpm for 45 min and re-dispersed in 5 ml of water. The Au nanoparticle dispersion (1 ml) was added to a solution with TEOS (0.86 ml), water (3.3 ml) and ethanol (23 ml). The solution was stirred for 10 min and an aqueous ammonia solution (28%, 0.65 ml) was injected. After 4 h of reaction under stirring, the Au@SiO2 core-shell nanocomposites were collected by centrifugation, washed with ethanol and re-dispersed in 20 ml of water. Au@SiO_2@RF sandwiched structures were prepared similarly to the preparation of SiO_2@RF core-shell particles. Briefly, 10 ml of Au@SiO_2 was mixed with resorcinol (0.02 g), formaldehyde (28 µl), and water (18 ml), followed by injecting 0.1 ml of ammonia solution (2.8%). The solution was stirred for 12 h at room temperature or 2 h at 50 °C. The solution was further refluxed at 100 °C for 4 h to facilitate the poly-condensation of RF and the sample was collected and washed with water. To obtain the Au@RF yolk-shell nanostructures, the silica core was removed by etching with a NaOH solution (1 ml, 2.5 M) at room temperature for 8 h.

3.2.6 Synthesis of Au@RF core-shell structures

The Au nanoparticle dispersion (0.2 ml) was mixed with water (27.8 ml), resorcinol (0.02g) and formaldehyde (28 µl) and the mixture was stirred for 10 min, followed by injecting 0.1 ml of ammonia solution (2.8%). The coating process continued

for 12 h at room temperature under magnetic stirring. The Au@RF core-shell particles were obtained after centrifugation and re-dispersed in water.

3.2.7 Synthesis of RF capsules through surface-protected etching approach

An extension of surface-protected etching approach was adopted to prepare RF capsules. 5 ml of the colloidal RF sphere dispersion was first diluted with 15 ml of water, followed by incubating the solution in a 50 °C water bath. After certain incubation time, the solution was cooled down to room temperature and subsequently 0.5 ml of HCl solution (1 M) was added. RF capsules were then obtained after centrifugation.

3.2.8 Characterizations

Morphology of the products was characterized by using a Tecnai T12 transmission electron microscope (TEM). A probe-type Ocean Optics HR2000CG-UV-NIR spectrometer was used to measure the UV-Vis extinction spectra and transmittance spectra. Zeta potential measurements of the colloidal dispersions were performed by using a Beckman Coulter Delsa Nano C Zeta Potential Analyzer. Fourier transform infrared spectroscopy (FTIR, Nicolet 6700) was used to characterize the chemical structure of the compounds. The crystal structure was determined by X-ray diffraction (XRD) analysis using a Bruker D8 Advance Diffractometer with Cu Kα radiation (λ = 1.5406 Å). The nitrogen adsorption-desorption isotherms of the hollow manganese oxide spheres were obtained at 77 K using with a Micromeritics ASAP 2020 Surface Area & Porosity Analyzer. The surface area was calculated from the adsorption isotherm using the multi-point BET method and the pore size distribution was determined by the BJH method from the adsorption isotherm.

3.3 A systematic study on the synthesis of RF spheres

In this study, colloidal RF resin spheres are synthesized based on an extended Stöber method developed by Lu et al. with some modifications.[18] The reported recipe involved two stages of synthesis occurring at 30 °C for 24 h and subsequently at 100 °C for 24 h in a Teflon-lined autoclave. The heating process is known to facilitate the poly-condensation process. We found that the spheres are formed in the first several hours and the sizes will not change after that. In our recipe, the colloidal RF spheres are collected and dispersed in water after 12 h of reaction at room temperature. For the poly-condensation process, we heated the colloidal RF dispersion at 100 °C for 12 h. As shown in Figure 1a, the color changed from light yellow to orange after refluxing, which is possibly due to some manner of oxidation occurring during the network formation process at high temperature.[36] The stability of w-RF and s-RF are evaluated in both base (NaOH) and acid (HCl) solutions, respectively. As shown in Figure 3.1a, the dispersion of w-RF spheres can be quickly dissolved in both NaOH and HCl solutions, resulting in clear solutions, while s-RF spheres are stable in both solutions. The color changes from orange to red after adding NaOH are believed to be caused by the sodium form of RF, where the hydroxyl groups (-OH) in the benzene rings are substituted by sodium (-ONa).[37]

The dissolution products in base and acid are analyzed by matrix-assisted laser desorption/ionization time of flight (MALDI-TOF) mass spectrometry, which is referred to as a “soft” ionization technique and causes minimal or no fragmentation.[38] The colloidal w-RF spheres are dissolved in aqueous NaOH and HCl solutions respectively

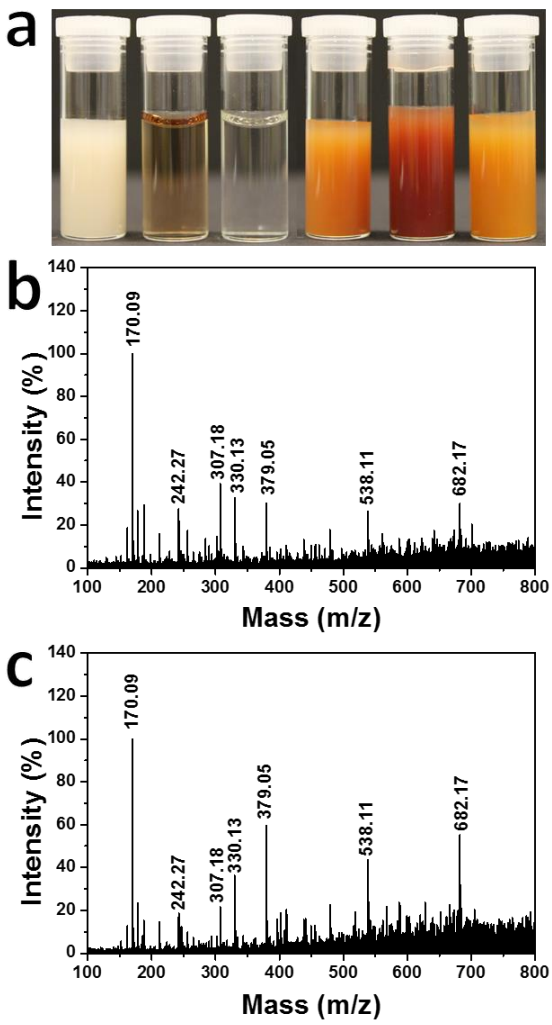

Figure 3.1 (a) Digital images showing the stability of w-RF and s-RF spheres in aqueous solution of NaOH and HCl. They are w-RF, w-RF dissolved in NaOH, w-RF dissolved in HCl, s-RF, s-RF with NaOH, and s-RF with HCl from left to right, respectively. MALDI-TOF mass spectrum of w-RF dissolved in (b) NaOH and (c) HCl. The intensities are normalized based on the strongest peak at 170.09 Da.

for MALDI-TOF measurement. Figure 3.1 b and c shows the MALDI-TOF mass spectra for the two cases, respectively, which exhibit same peak positions but with slight difference in peak intensities. The decomposed species are oligomers which could be mainly attributed to monomers, dimers and trimers, suggesting the weak connections inside the w-RF structures. This finding, on the other hand, may allow us to investigate the mechanism of the organic sol-gel network forming reaction of resorcinol and formaldehyde in a reverse manner. The strongest peak at 170 Da can be possibly attributed to the following structure, which indicates the addition reaction for resorcinol, formaldehyde, and ammonia. Ammonia is usually believed to be the catalyst and to provide a basic condition for the addition reaction of resorcinol and formaldehyde.[18] However, our study suggests that ammonia involves in the reaction and plays an

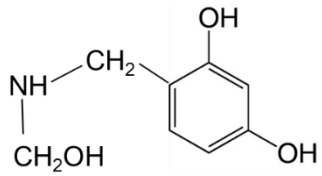

important role in the formation of RF spheres, which will be discussed later.

Colloidal silica spheres obtained through the classic Stöber method have been widely used as hard templates to prepare hollow nanostructures.[4] The most commonly used acid and base etchants to remove silica templates are HF and NaOH, respectively. Similar to silica, colloidal RF resin spheres have also been demonstrated as hard templates.[16] The most common way to remove RF core is to calcine RF@shell products in air at high temperature. However, many shell materials such as polymer and polyelectrolyte structures cannot survive and may lose their surface properties upon calcination. The amphoteric nature of w-RF spheres enables them as robust colloidal

templates. To demonstrate w-RF colloidal spheres as robust templates, hollow amorphous TiO_2 spheres are prepared by coating TiO_2 onto w-RF spheres and then dissolving the RF core in NaOH or HCl. Those amorphous TiO_2 shells collapse and form bowl-like structures because they are not rigid enough to support the hollow structures and thus collapsed into their internal cavities during drying. In contrast to silica colloids, which are inert to most shell precursors, RF spheres are believed to be reductive. For example, Zhang and co-workers reported that Ag^+ could be reduced by RF and form Ag nanoshell on RF.[39] Here we demonstrate that MnO_2 shells could be readily formed on RF spheres through reduction of $KMnO_4$ (Figure 3.2 c), which will be discussed in detail in section 3.5. After removal of w-RF core with NaOH, RF@MnO_2 core/shell structures were converted into porous MnO_2 shells (Figure 3.2d), which have been demonstrated as promising electrode materials for supercapacitors and lithium ion batteries.

We then investigate the surface properties of colloidal resin spheres by measuring zeta potential because it is a key indicator of the stability of colloidal nanoparticles. Zeta potential is a measure of the magnitude of the electrostatic or charge repulsion/attraction between particles, and is one of the fundamental parameters known to affect stability. Silica colloids prepared via Stöber method are well dispersed in water and negatively charged with a zeta potential value of -67 mV, which is attributed to the hydroxyl groups. Similar to silica colloids, the zeta potential for s-RF spheres also exhibits a negative value of -72 mV due to abundant phenolic hydroxyl groups. Although there are also plentiful of hydroxyl groups in w-RF spheres, the colloidal w-RF resin spheres are positively charged with a zeta potential value of 70 mV. Interestingly, we also found that the w-RF colloids

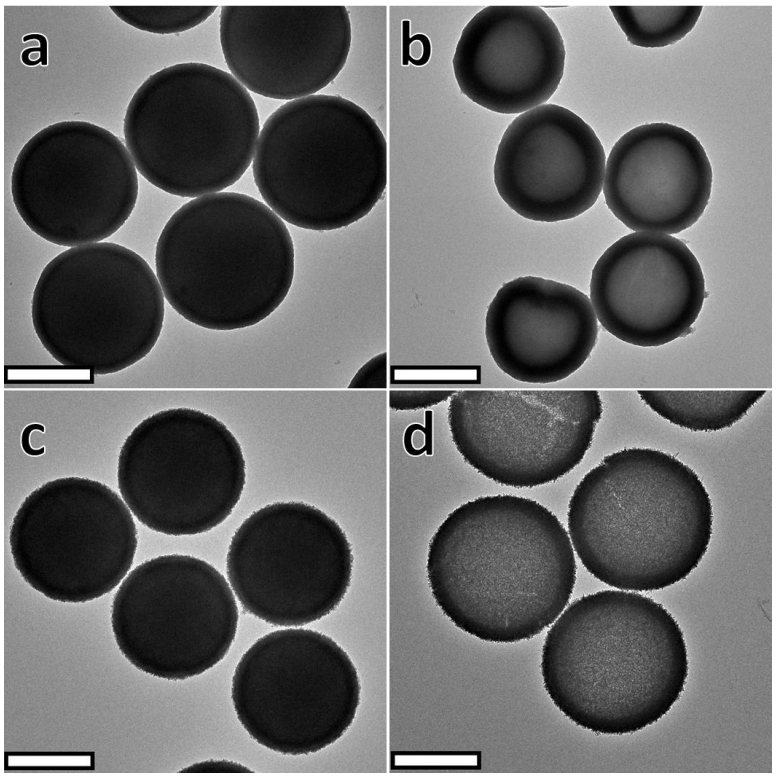

Figure 3.2 TEM images showing colloidal w-RF spheres serving as robust hard templates for the preparation of core-shell and hollow structures; (a) w-RF@TiO_2, (b) TiO_2 bowl-like hollow structures, (c) RF@MnO_2, (d) MnO_2 hollow spheres. The scale bar is 400 nm.

become instable and tend to form agglomerates during the storage, indicating the surface property changes upon storage.

As mentioned in Experimental, the difference between w-RF and s-RF spheres in the aspect of preparation is that s-RF spheres are the poly-condensed products of w-RF spheres at 100 °C, indicating that the poly-condensation process for w-RF spheres is not a simple condensation reaction in which the hydroxymethyl (-CH_2OH) derivatives are converted into methylene (-CH_2-)- and methylene ether (-CH_2OCH_2-)-bridged compounds. The most commonly used alkaline catalyst for the polymerization reaction of R with F is sodium carbonate (Na_2CO_3), which is important for the formation of the hydroxymethyl derivatives during the addition reaction. However, the addition and condensation reactions cannot explain the positive zeta potential of colloidal w-RF spheres because similar structures for w-RF and s-RF spheres would be obtained. Note that resorcinol and formaldehyde are mixed in water with ammonia presenting in our study. In contrast to sodium carbonate, Gils studied the reaction of resorcinol, formaldehyde, and ammonia in 1969 and found that ammonia reacts rapidly with formaldehyde to form an unstable intermediate which then reacts with resorcinol and forms white precipitates at room temperature.[40] He proposed the structure of the precipitates containing tertiary amine, which can lead to positive charges. To this end, we can attribute the positive charges to the amine groups. The MALDI-TOF mass spectra further confirms the existence of amine groups.

To investigate the surface changes in detail, we performed a time-evolved measurement of zeta potential. Briefly, freshly prepared colloidal w-RF spheres are

treated in water at a relatively high temperature (e.g. 50 °C) to facilitate the surface evolution, followed by collecting samples at different time and measuring their zeta potentials. Higher temperature (e.g. 100 °C) treatment is found to accelerate the evolution process. As plotted in Figure 3.3a, zeta potential gradually decreased from positive to negative as increasing incubation time. Zeta potential decreased from 76 mV to ~ 0 mV in 2 h and slowly decreased to -57 mV in 7 h. The amine groups and hydroxyl groups together determine the value of zeta potential. More amine groups, more positive charges. In principle, the amount of phenolic hydroxyl groups for w-RF and s-RF spheres should be the same, indicating the amount of amine groups is decreasing during heating. We believe that our new understanding on zeta potential evolution of colloidal w-RF spheres will shed light on using them as hard templates. For instance, freshly prepared w-RF spheres can be better dispersed in water for more uniform coatings. To slow down the surface evolution, w-RF spheres can be stored at lower temperature (e.g. 4 °C in refrigerator).

To study the chemical structure changes during the heating or curing process, samples collected at different stages are characterized by FT-IR spectroscopy (Figure 3.3b). Resorcinol, or 1,3-dihydroxybenzene, is a phenolic tri-functional compound, which can add formaldehyde in the 2-, 4-, and/or -6 positions in its aromatic ring.[32] For weakly crosslinked RF polymers, not all those three positions are substituted, which will be reflected on the FTIR spectra. Specifically, the w-RF resin spheres exhibit bands at 745, 787, 842, and 895 cm^{-1}, which could be ascribed to the out-of-plane and in-plane bending modes of hydrogen atoms in the aromatic rings, indicating a large population of

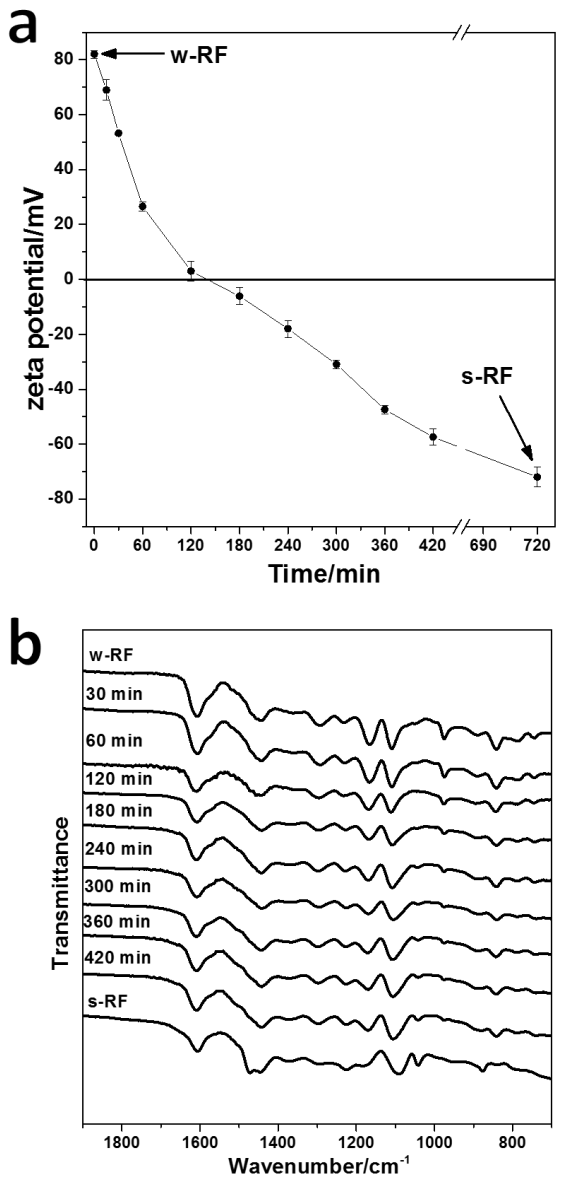

Figure 3.3 Time evolution of (a) zeta potential and (b) FTIR spectra for the w-RF dispersion incubated at 50 °C and collected at different time intervals. The zeta potential values and FTIR spectra for w-RF and s-RF spheres are also plotted in the graph.

unsubstituted hydrogen atoms in the benzene rings. Those characteristic peaks gradually disappear with increasing incubation time, confirming the occurrence of condensation reaction. There is only one characteristic peak at 876 cm^{-1} that is also ascribed to the out-of-plane C-H bending modes in the benzene rings for s-RF spheres, suggesting the formation of penta-substituted aromatics after long time crosslinking reactions. Notably, the CH_2 bending band at 1474 cm^{-1} and C-O-C stretching mode at 1041 cm^{-1} are evolved in the s-RF spheres, indicating the increase of both methylene and methylene ether bridges. The band at 1165 cm^{-1}, which could be ascribed to C-N stretching mode, gradually fade away as the incubation time prolonged, which is consistent with the evolution of zeta potential. Based on those results, we postulate that the C-N bonds are broken followed by crosslinking the benzene rings with methylene bridges while small molecules of ammonia or amine are formed and dissolved in water. Elemental analysis of both w-RF spheres and s-RF spheres may help reveal the difference in nitrogen amount.

Sol-gel derived silica has been widely used to coat onto colloidal nanoparticles to form core-shell structures to greatly enhance the stability against coalescence because of its chemical inertness, optical transparency, and porous structure. Our group have previously demonstrated a general sol-gel process to form a coating of RF resin on inorganic nanostructures by modifying the surface charge of the core materials.[19] Highly crosslinked RF resin spheres are stable in both NaOH and HCl solutions, enabling them as a robust shell material. As revealed in Figure 3.4a and c, RF resin shells are readily formed on silica spheres and FeOOH nanorods, respectively, resulting in core-shell particles. After refluxing the core-shell particles in water to further condense RF shells,

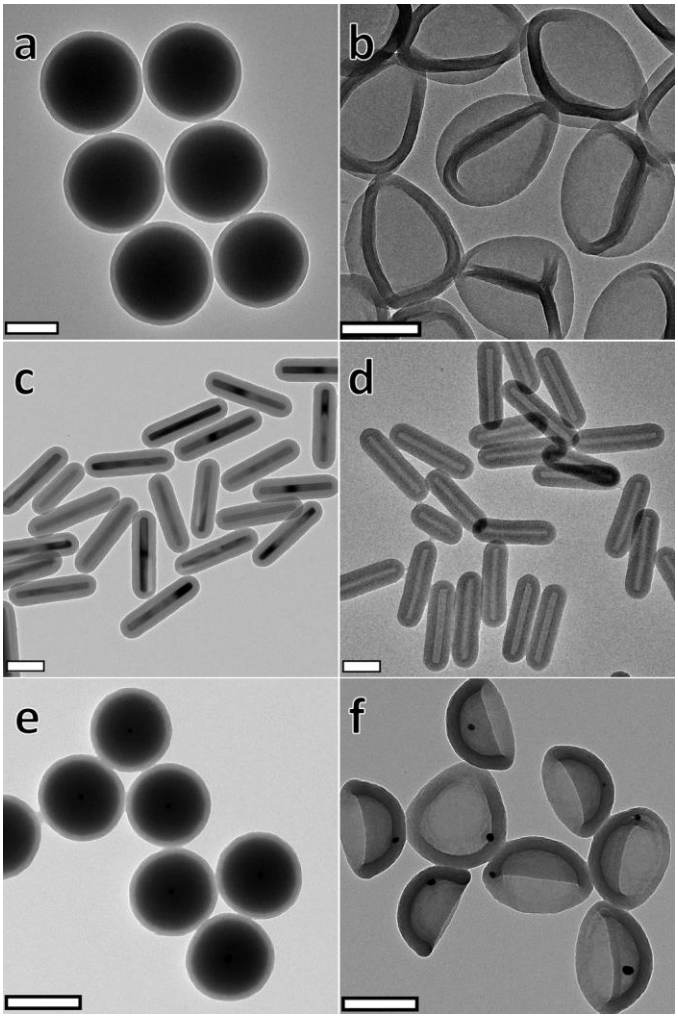

Figure 3.4 TEM images showing s-RF resin as robust shell materials; (a) SiO_2@RF and (b) bowl-like RF capsules, (c) FeOOH@RF and (d) tubular RF capsules, (e) Au@SiO_2@RF and (f) Au@RF nanobowls. The scale bar is 200 nm.

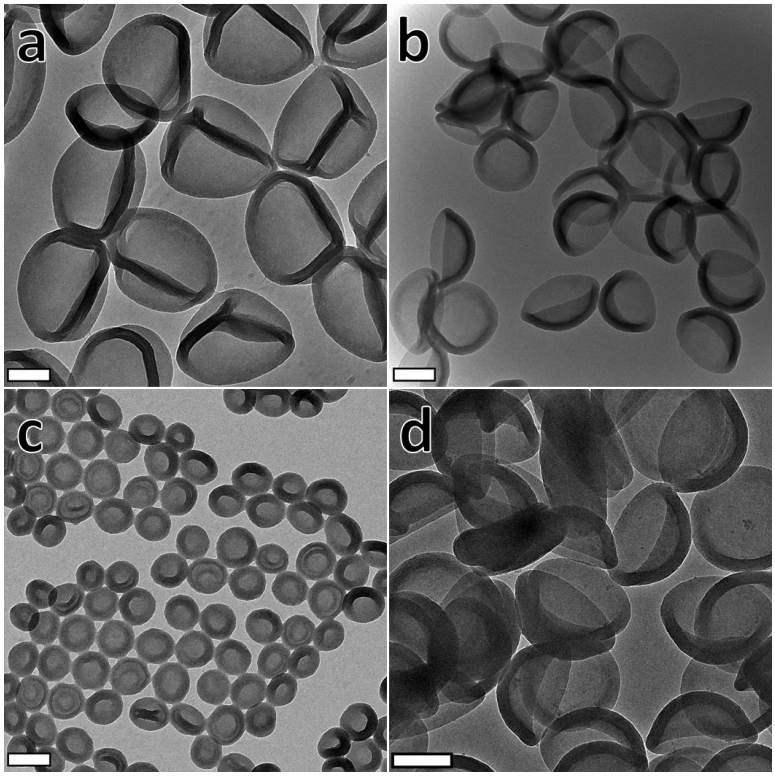

Figure 3.5 TEM images showing the bowl-like RF capsules of various sizes (a) 360 nm, (b) 200 nm and (c) 80 nm in inner diameter. (d) TEM image showing bowl-like carbon structures after carbonization of the bowl-like RF capsules in (a). The scale bar is 200 nm.

the core materials are then removed in the etchants of NaOH (for silica) and HCl (for FeOOH). RF capsules with bowl-like and tubular structures could be readily obtained (Figure 3.4c and d). The as-prepared hollow RF particles are porous in nature as the alkali solution could readily penetrate the shell to etch the core materials. The bowl-like RF capsules are formed because polymeric RF shells are not rigid enough to support the hollow structures and thus collapsed into their internal cavities during drying.[41] In addition, we have successfully demonstrated size tunability of bowl-like RF capsules by using silica templates with different sizes. The silica templates used in Figure 3.5 a, b and c are 360, 200, and 80 nm in diameter, respectively. After RF coating and removal of silica templates, all of them result in bowl-like structures, also referred to as nanocups, which are promising for intelligent drug delivery/releasing and treatment monitoring. RF resin has been widely applied to the fabrication of various carbon nanomaterials, such as carbon aerogels and carbon spheres, because of their outstanding properties and promising applications. As illustrated in Figure 3.5d, the bowl-like RF capsules can be successfully converted into carbon bowls after carbonization at 800 °C for 2 h, which could be used as high-performance electrode materials with increased packing density by stacking the bowls together.[42]

It has been well demonstrated that the encapsulation of functional nanoparticles in hollow materials not only effectively enhances the stability of these nanoparticles, but also introduces new functionalities for hollow materials.[43] Silica has been frequently used for making core-shell nanostructures because of the simple setup and excellent reproducibility. In combination with silica coating, further coating of RF resin on silica

will lead to form sandwich-like core@SiO_2@RF structures. The selective removal of silica produces core@RF yolk-shell structures. As a demonstration, sandwich-like Au@SiO_2@RF structures are first obtained through sequentially coating silica and RF onto Au nanoparticles (Figure 3e). After selective removal of the inner silica shell using either HF or NaOH, Au@RF yolk/shell nanostructures could be produced. Similarly, the RF shells collapse and form bowl-like structures after drying. As the RF shells are permeable and stable, we believe that the hollow RF nanostructures hold great potential in the research field of nanoreactors.

3.4 Surface-protected etching toward RF capsules

In addition to the hard-templating approaches toward hollow structures such as RF capsules, direct synthesis without the need of additional templates, namely self-templating method, is preferred in practical applications due to significantly reduced production cost and the ease of scaling up.[21] The self-templating strategy has been developed as one of the most important strategies to effectively fabricate hollow mesoporous silicas. Hollow structures can be synthesized by enhancing the relative stability of the surface layer of a single-component nanostructure to make it more stable than interior. Our group first demonstrated a surface-protected etching process for the preparation of permeable silica shells.[23] In a typical surface-protected etching process, colloidal silica spheres from Stöber method are coated with a protected layer of polyvinylpyrrolidone (PVP) followed by selectively etching the interior part by using an appropriate etchant such as NaOH or water.

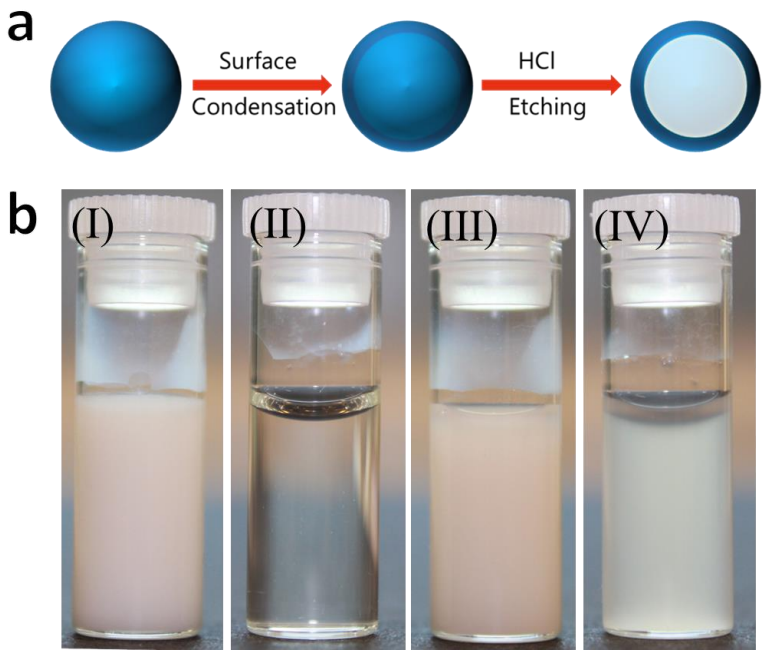

Figure 3.6 (a) Schematic illustration of the synthesis of colloidal RF hollow capsules through the extension of surface-protected etching process. (b) Digital images showing the surface condensation and selective etching of w-RF spheres (I) as-prepared w-RF dispersion and (II) after adding HCl solution, (III) w-RF spheres after surface-condensation at 50 °C and (IV) after adding HCl solution.

As the formation process and some properties of colloidal RF spheres are very similar to those of silica colloids, an immediate and natural question is whether the surface-protected etching approach can be extended to the preparation of hollow RF capsules. As weakly crosslinked RF spheres are less stable than highly poly-condensed ones, crosslinking the outer layer can enhance its stability, making it possible for selective removal of the interior to obtain hollow structures. The scheme in Figure 3.6a illustrated the self-templating strategy towards hollow RF capsules. Typically, as-prepared w-RF spheres dispersed in water are heated to enhance the surface stability. As mentioned above, the freshly prepared RF spheres can be easily dissolved in water, as shown in Figure 3.6b (II). After incubation in water at an appropriate temperature, the surface layer is more crosslinked than the interior, resulting in a more stable out layer. The weakly crosslinked inner section can then be easily dissolved away using etchant of HCl, leading to uniform polymer capsules. Figure 3.6b (III) and (IV) are digital images showing the transmittance difference before and after adding HCl, which clearly indicates the selective etching process. Incubation temperature of 50 °C is chosen in this study because the entire sphere is quickly cross-linked at higher temperature (e.g. 100 °C), while it takes longer time to condense the surface layer at lower temperature.

The hollowing process can be well controlled by monitoring the transmittance of the colloidal system. As shown in Figure 3.7a, upon adding HCl, the overall transmittance decreases accordingly with increasing incubation time because more crosslinking between RF oligomers results in less dissolution in HCl. The refractive-index contrast between the capsules and the solution increases as less RF can be replaced

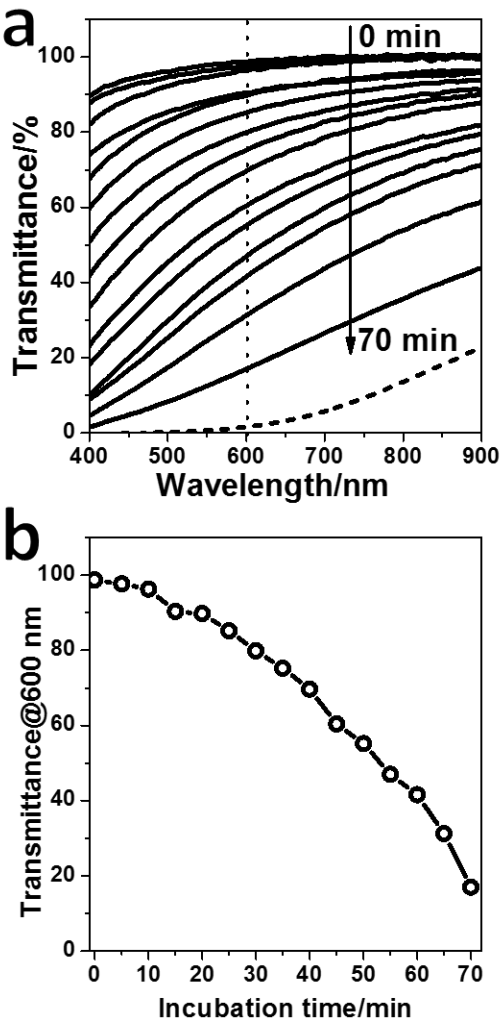

Figure 3.7 (a) Optical transmittance spectra of a typical sample of RF spheres during the surface-protected etching process. Colloidal RF spheres are incubated in water at 50 °C for different time. Samples are collected at 5 min interval, followed by adding HCl to selectively etching the interior. (c) Dependence of the transmittance at 600 nm on the incubation time.

by water during dissolution. The extent of etching can therefore be precisely controlled by monitoring the change in the transmittance of the dispersion. For better comparison, Figure 3.7b summarize the dependence of the transmittance at 600 nm on the incubation time for a typical RF colloidal sample. As it takes time to condense the surface layer, the transmittance in the first 10 min of reaction changes very slowly and keeps at ~95%, indicating the dissolution of almost the entire spheres. After 60 min incubation, the transmittance decreases to ~40%.

Figure 3.8 shows TEM images of the original RF spheres and three samples collected at different incubation time. When the colloids are incubated for only 30 min, RF capsules with very thin shells are formed after etching with HCl. Because of the weakly cross-linking nature and the thin shells, the shells collapse and form deflated capsules. As the incubation time is prolonged to 40 min, thicker out-layer will be cross-linked, resulting in RF capsules with thicker shells. Permeable shells are formed because the RF oligomers can be easily transported outside. Noteworthy is the size of the resulted capsules is larger than that of the solid RF spheres, which may be due to the stretching of polymeric framework that is similar to the formation of TiO_2 microcapsules.[24] Hence, we have successfully extended the surface-protected etching strategy towards preparing RF capsules with controllable shell thickness by partially crosslinking the out-layer and then selectively removing the inner part.

The simple process reported here can also be conveniently used to convert various RF coated composite particles into yolk-shell nanostructures. As a robust coating material, RF can be easily coated on various nanostructures of different compositions and

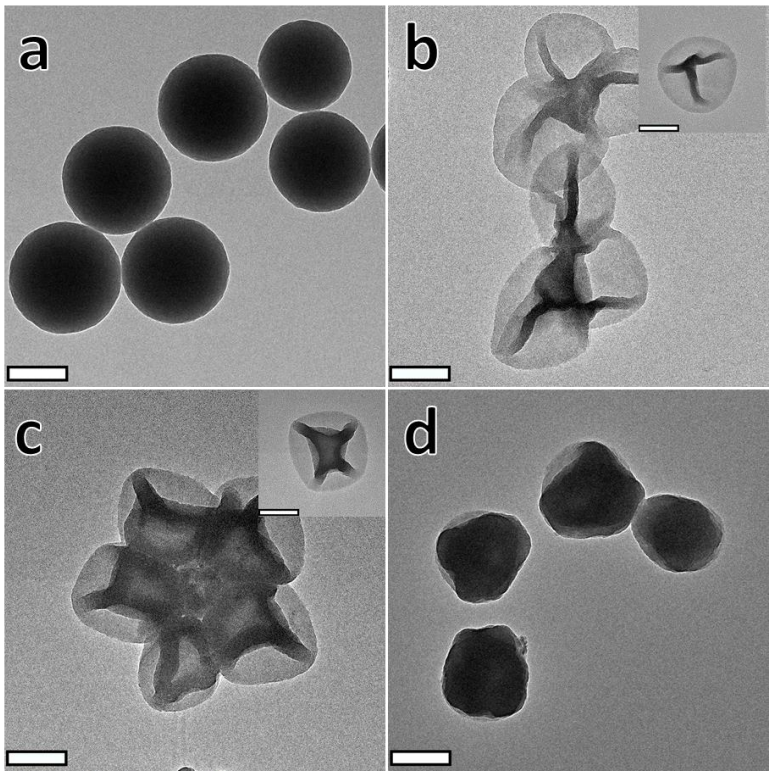

Figure 3.8 TEM images of (a) as-prepared w-RF spheres, and RF capsules obtained at different stages of condensation and etching process: (b) 30 min, (c) 45 min, and (d) 60 min. The scale bar is 200 nm.

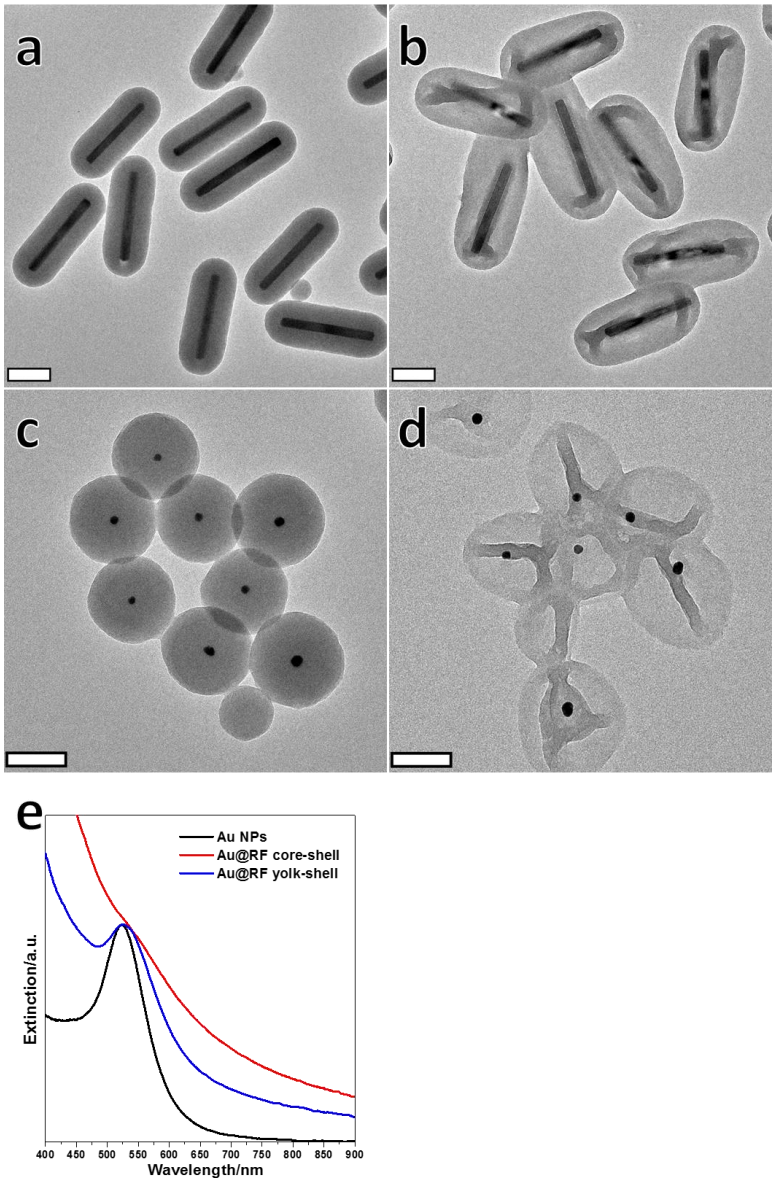

Figure 3.9 TEM images showing the conversion of core@RF particles into yolk@RF capsules through the surface-protected etching process: (a) FeOOH@RF core-shell structures and FeOOH@RF yolk-shell capsules, (c) Au@RF core-shell nanostructures and (d) Au@RF yolk-shell capsules. The scale bar is 200 nm. (e) UV-vis-NIR extinction spectra suggesting the conversion of core-shell to yolk-shell structures.

morphologies, providing a large family of core-shell particles. For example, FeOOH@w-RF core-shell particles with rod morphology are prepared at room temperature to further demonstrate the effectiveness of the extended surface-protected etching strategy. As shown in Figure 3.9a and b, after 30 min partially condensation in water at 50 °C, the core-shell particles are converted into yolk-shell particles with movable FeOOH rods encapsulated in RF capsules. We also use Au NPs (~20 nm) as the core materials to fabricate the Au@w-RF core-shell nanoparticles with shell thickness of 80 nm. After surface condensation and selective removal, Au@RF yolk-shell can be readily obtained, as shown in Figure 3.9c and d. The UV-vis spectra (Figure 3.9e) further confirms the dissolution of inner RF shell. After etching, as the RF near the Au surface was replaced by water, the Au NP absorption nearly returned to the original peak position of pure Au NPs. Based on these results, we believe that surface-protected etching method can be successfully applied to the synthesis of RF capsules as well as yolk-shell nanostructures with various compositions and functions. The as-prepared yolk-shell particles could be converted into carbon composites after the carbonization under N_2 atmosphere, which hold promising applications in energy storage and catalysis.

3.5 Template-engaged redox reaction toward hollow MnO_2 nanostructures

Optical properties of nanomaterials can be effectively modulated by manipulating their micro-/nanostructures. Particularly, the rational design and synthesis of hollow structured materials are of great significance due to their intriguing structure-induced properties and widespread applications. Recently, template engaged redox reactions have shown great potential for the synthesis of hollow nanostructures. For example, Xia and

co-workers developed a template-engaged replacement reaction approach to the large-scale synthesis of hollow noble metal nanostructures with controllable voids and shell thicknesses.[44] By utilization of template-engaged redox etching on shape-controlled Cu_2O crystals, Lou and co-workers reported the synthesis of $Fe(OH)_x$ hollow structures with designed shapes and complex interiors.[45] Hollow manganese oxide spheres have shown great potential in diverse fields, such as supercapacitors, lithium ion batteries, and molecular adsorption.[46-48] One effective way to prepare hollow MnO_2 is to use reactive templates such as carbon and $MnCO_3$ to reduce $KMnO_4$ to manganese oxides.[47-49] However, preparation of carbon templates as well as post removal of the carbon cores usually require high temperature treatment, which is time consuming, not energy efficient, and may cause environmental concerns. It is thus highly desirable to develop a simple yet effective protocol to synthesize hollow manganese oxide nanostructures.

In this section, we report a simple template-engaged redox reaction route to synthesize hollow manganese oxide nanostructures based on the redox reaction between RF resin spheres and $KMnO_4$. Since Lu and co-workers' seminal report on the synthesis of monodisperse RF resin colloidal spheres through an extension of Stöber method in 2011, much attention has been paid to utilize RF resin polymer spheres as both hard templates and coating materials.[18] By utilizing the reductive property of RF, Zhang et al. have synthesized silver shells on RF spheres through the reduction of silver-ammonia complexes.[39] In our strategy, the coating of MnO_2 can be quickly completed at room temperature by redox etching of RF polymers to form soluble species. By modifying the surface properties, our group developed a general sol-gel process to form a coating of RF

resin on inorganic nanostructures of various compositions and morphologies. SiO_2@RF core-shell nanospheres with a thin layer of RF resin are used to monitor the evolution process of shell formation. Based on the improved understanding, the strategy presented here can be easily extended to the design and preparation of interesting structures such as core-shell and yolk-shell structures. Thanks to the facile control over the sizes of RF spheres, we demonstrate that hollow manganese oxides shells with certain sizes exhibit bright colorations owing to resonant Mie scattering.

The spheres of RF resin were prepared based on an extension of the Stöber method reported by Lu and co-workers with minor modifications. RF resin spheres with size of ~380 nm in diameter (Figure 3.10a) were synthesized at room temperature and redispersed in water, followed by introducing an aqueous solution of $KMnO_4$ to initiate the redox reaction. As a strong oxidizing agent, $KMnO_4$ has been commonly utilized to oxidize a wide range of organic molecules, producing molecules with functional groups of carbonyl and carboxylic acid, and a precipitate of manganese oxides. The precipitates are confined to the vicinity of the template surface and evolve into a porous shell around the RF template, as shown in Figure 3.10b. The inner template can then be dissolved away by adding NaOH, leading to the formation of hollow MnO_2 spheres (Figure 3.10c).

The Fourier transform infrared (FTIR) spectroscopy was carried out to study the composition changes. As shown in Figure 3.10d, the FTIR spectrum of the RF resin templates is consistent with the reported ones. After manganese oxides deposition, the FTIR spectrum of the obtained core-shell composites matched well with that of the pure RF with an extra band in the low frequency region at ~560 cm^{-1}, which also appears in

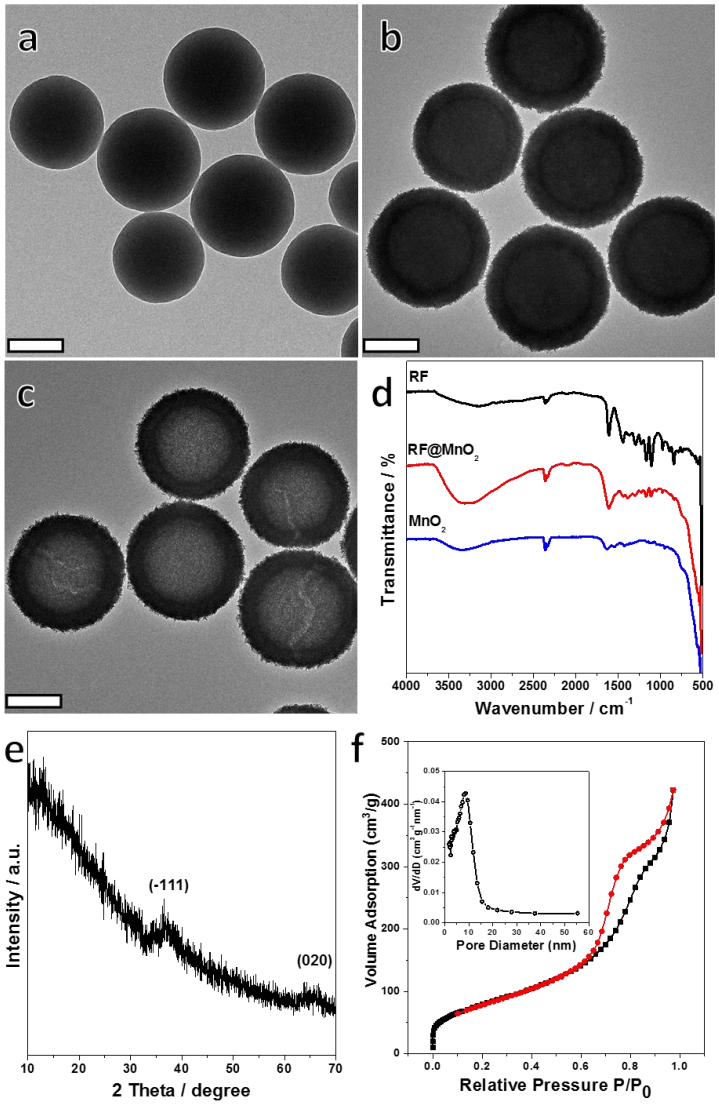

Figure 3.10 TEM images of (a) colloidal RF spheres, (b) RF@MnO_2 core-shell particles, and (c) MnO_2 hollow spheres. The scale bar is 200 nm. (d) FTIR spectra for the above three samples. (e) XRD pattern for hollow MnO_2 spheres. (f) N_2 adsorption/desorption isotherms of hollow MnO_2 spheres. Inset shows the BJH pore size distribution.

hollow MnO_2 spheres and could be attributed to the Mn-O vibrations. The crystallographic structure of the resultant hollow structures is examined by powder X-ray diffraction (XRD), as shown in Figure 3.10e. The diffraction peaks can be indexed to the birnessite-type manganese oxide (JCPDS No. 80-1098), which has a lamellar structure.[50] The broaden peaks with low intensity indicate that the sample is in poor crystalline state because the reaction is carried out at room temperature. Figure 3.10f shows the N_2 adsorption-desorption isotherms and the Barrett-Joyner-Halenda (BJH) pore size distribution curves (inset) of a typical hollow MnO_2 spheres. The isotherm has the characteristic Type IV shape indicating the presence of mesopores, as confirmed in the BJH pore size distribution with average pore diameter of 8.4 nm. A relatively large BET specific surface area of 287.8 m^2/g is found for the typical sample, which would be very beneficial for adsorbing and removing organic contaminants and hold great potential in supercapacitors.

To better understand the evolution of MnO_2 shells, SiO_2@RF core-shell structures are used for the redox reaction because clear contrast could be visualized under TEM. A thin layer of RF resin (~ 5 nm) was first coated on colloidal silica spheres to form SiO_2@RF core-shell particles. As can be seen from Figure 3.11b, very thin and porous manganese oxide shells with needle or sheet-like shapes are readily formed when small amount of $KMnO_4$ was introduced. As increasing the amount of the precursor, a gap between the shell and the template was found (Figure 3.11c), suggesting the oxidative etching of the RF resin possibly into oxidized RF oligomers. This also proves that species including MnO_4^- and oxidized RF oligomers can transport across the shells freely during

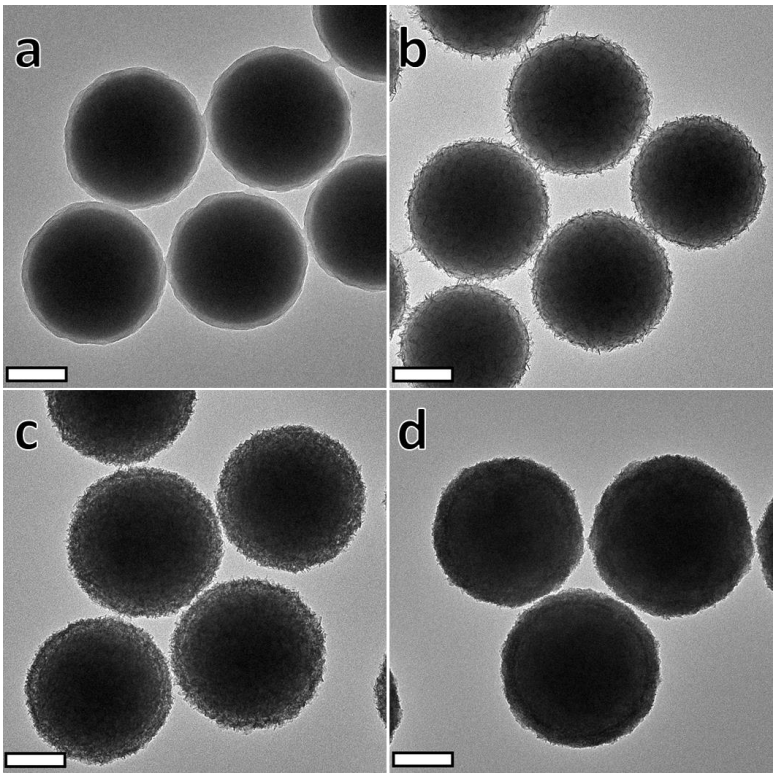

Figure 3.11 TEM images showing the evolution of MnO_2 shell formation. (a) SiO_2@RF, Deposition of MnO_2 shells on SiO_2@RF core-shell structures by adding different volume of precursors (b) 50 µl, (c) 200 µl, and (d) 1 ml of 0.02 M $KMnO_4$ solution. The scale bar is 100 nm.

the etching process. Further addition of $KMnO_4$ results in the depletion of RF and the loss of the gap due to the inward diffusion of $KMnO_4$ and the deposition of manganese oxides in the void space, which also indicates the formation of SiO_2@MnO_2 core-shell nanocomposites (Figure 3.11d). One advantage of using RF templates is that RF resin can be coated on various colloidal nanostructures through a general sol-gel process, which provides an ideal platform to deposit manganese oxides on various colloidal particles with the aid of a thin layer of RF resin coating.

The template-engaged redox etching mechanism allows the fine control over the structures.[44, 45, 51] In addition to the formation of core-shell structures, nanorattles or yolk-shell nanostructures could be readily obtained by controlling the degree of redox etching. Au@RF core-shell nanospheres are used to demonstrate the facile control over the structures. As shown in Figure 3.12a and b, a thin layer of MnO_2 is deposited onto the surface of RF with a small amount of $KMnO_4$, while increasing the amount of $KMnO_4$ leads to the formation of Au@RF-MnO_2 nanorattles. The eccentric position of Au@RF core confirms the freely movable yolk in the void space. When adding more manganese precursors, the shell thickness is further increased, as shown in Figure 3.12c. By carefully investigating the inner and outer diameter of the hollow spheres in Figure 3.12b and c, we found that the outer diameter does not increase much (~5 nm) while the inner diameter decreases dramatically (~45 nm), which further confirms the deposition of MnO_2 mainly onto the inner surface of the shell. With excess addition of $KMnO_4$, which is visually observed through the purple supernatant, all the RF polymers have been consumed and dense shells with further reduced void space are formed (Figure 3.12d).

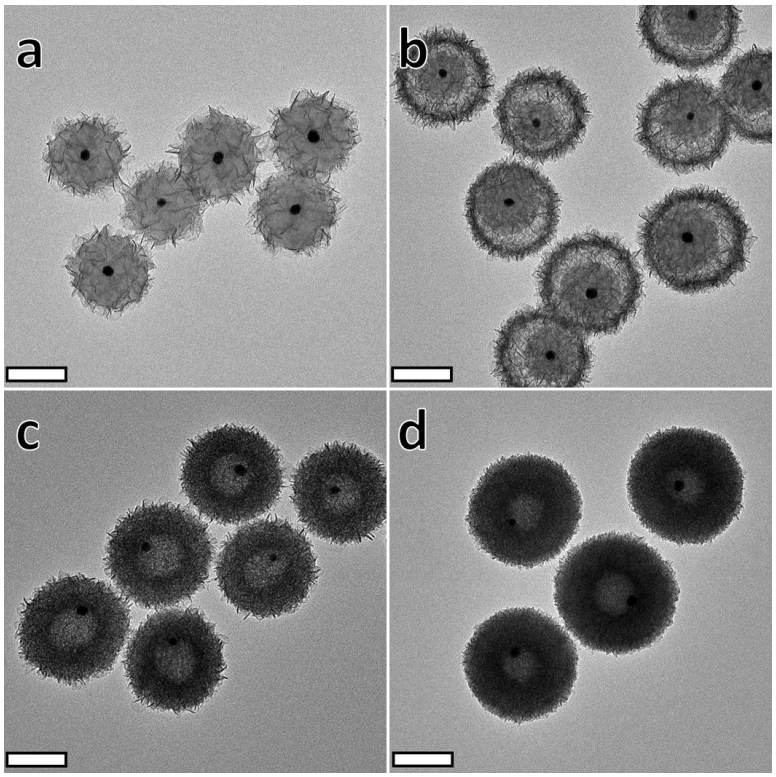

Figure 3.12 TEM images showing the fine control over the structures by adding different volume of $KMnO_4$ precursors. MnO_2 deposition on Au@RF core-shell nanoparticles to form (a) Au@RF@MnO_2 sandwich structures, (b) Au@RF-MnO_2 yolk-shell structures, (c) and (d) Au@MnO_2 yolk-shell structures by adding 50 µl, 200 µl, 500 µl, and 1 ml 0.02 M $KMnO_4$ solutions. The scale bar is 100 nm.

Another advantage of employing RF resin spheres as sacrificial templates is the wide size tunability. Lu and co-workers reported that the particle size of RF spheres could be readily tuned from 200 to 1000 nm by an extension of the Stöber method, which provides a large family of templates with tunable sizes.[18] Optical responses from resonant Mie scattering of hollow nanostructures attract much attention. For instance, multiple color appearance ranging from blue and green to yellow and violet has been observed for hollow silica spheres with different sizes.[29, 52] The utilization of a hollow nanostructure significantly enhanced the transport mean free path of incident light, thereby inhibiting the multiple scattering and making the color from Mie resonance visible to the bare eye. Mie theory is used to explain the color effect as well as to rationally design new hollow nanomaterials with resonant Mie scattering. The resonant Mie scattering is highly dependent on the refractive index of the shell material, which is reflected on the size variations for different materials. For example, hollow silica spheres of 333 nm in diameter exhibits blue coloration, while the size of hollow TiO_2 shells with blue color is 220 nm in diameter because of the difference in their refractive indexes.[29, 31] Calculations using Mie theory (Figure 3.13a) suggest that MnO_2 hollow spheres will exhibit colors with sizes around 500 nm of inner diameter. As a demonstration, we have synthesized two types of hollow MnO_2 spheres with inner diameter of ~470 and 530 nm (Figure 3.13b and 3.13c), respectively. Those hollow MnO_2 spheres were spray-coated on a black substrate by an airbrush in a butterfly pattern. Remarkable colors are observed for the two hollow structures: the smaller one exhibits purple color and the larger one presents green color (Figure 3.13d). The color of visible Mie scattering in the hollow shells was highly

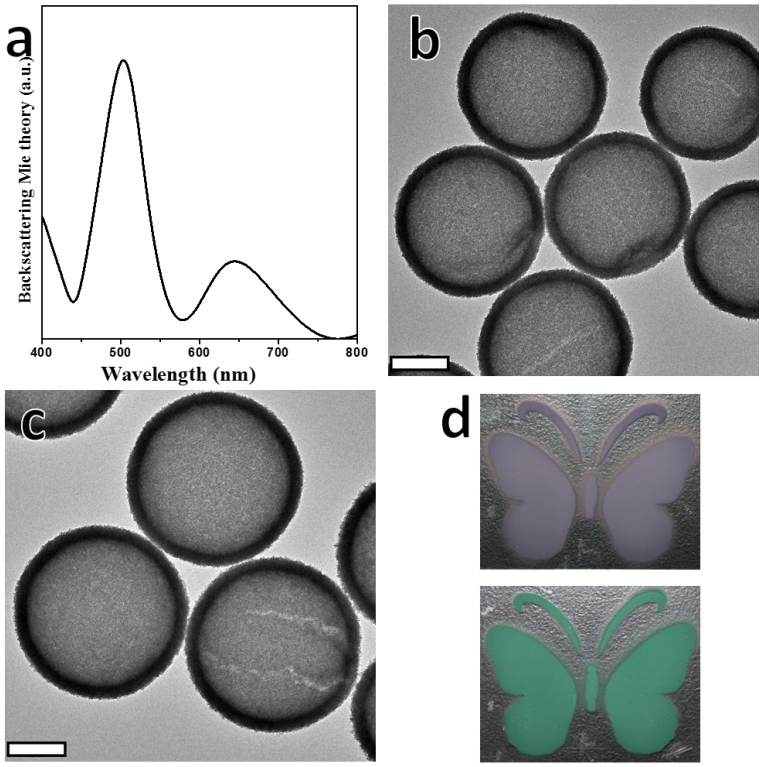

Figure 3.13 (a) Simulation of Mie backscattering for hollow MnO_2 spheres with 500 nm inner diameter and 40 nm shell thickness using n=2.1+0.05i. TEM images of hollow MnO_2 spheres with inner diameter of (b) 470 nm and (c) 530 nm. The scale bar is 200 nm. (d) Spray-coating the hollow spheres onto a patterned butterfly with carbon black as background showing remarkable colors of purple and green for samples in (b) and (c), respectively.

responsive to the surrounding medium such as solvent, which is particularly favorable for anti-counterfeiting applications.[31]

3.6 Conclusion

In summary, we have carried out a systematic study on the properties of RF spheres. Differences between w-RF spheres and s-RF spheres have been elucidated in the aspect of stability, surface property, and chemical structures. Colloidal w-RF spheres can be easily dissolved or etched in either aqueous NaOH solution or aqueous HCl solution, while colloidal s-RF spheres are stable in both solutions. The high stability of s-RF resin structures can be used to create various hollow RF capsules by removing the core particles in core@RF core-shell structures, while colloidal w-RF spheres can be used as a robust hard template for the preparation of hollow shells which are sensitive to high temperature calcination. A new understanding on the chemical structures of w-RF and s-RF resin spheres is proposed, which is different from the literature reports. The abundant amine groups (secondary and tertiary) in the colloidal w-RF resin spheres make their surface positively charged, while the loss of amine groups and the abundant hydroxyl groups render negative surface charges for s-RF spheres. We believe that our new understandings will shed light on the rationally design and synthesis of RF-based nanostructures.

Surface-protected etching has been successfully applied to the preparation of hollow RF capsules. The method involves the surface condensation of RF spheres at elevated temperature, followed by removal of the inner weakly-crosslinked part through chemical etching. Tuning the condensation time controls the shell thickness of the hollow

RF capsules which collapse to deflated capsules after drying. This self-templated strategy can be further used to construct yolk-shell nanostructures, in which nanoparticles such as Au nanoparticles and FeOOH nanorods can be easily encapsulated in the RF capsules to prevent the aggregations of those core particles. We believe that the porous RF capsules are expected to find use in important applications such as catalysis and nanoreactors.

We have also demonstrated a useful strategy for synthesis of high-quality mesoporous MnO_2 hollow structures with controlled shell thickness by template-engaged redox etching of RF resin polymers. This synthetic strategy is highly efficient and applicable to RF resin coated nanocomposites, which provides a versatile method for selective synthesis of core-shell, yolk-shell, and hollow nanostructures. A thin RF resin coating could be employed as a mediated layer for coating of MnO_2 on different nanostructures, providing a useful tool to construct core-shell nanocomposites. The same strategy can be used to rationally tailor the morphology of the final products to form uniform hollow structures such as Au@RF-MnO_2 yolk-shell structures. Using Mie theory, we can design the visible Mie scattering from hollow MnO_2 spheres and tune the color appearance from purple to green by adjusting the template diameter from 470 to 530 nm.

3.7 References

1. Yin, Y.; Alivisatos, A. P. *Nature* **2005,** 437, (7059), 664-670.

2. Murray, C. B.; Sun, S.; Gaschler, W.; Doyle, H.; Betley, T. A.; Kagan, C. R. *IBM Journal of Research and Development* **2001,** 45, (1), 47-56.

3. Park, J.; Joo, J.; Kwon, S. G.; Jang, Y.; Hyeon, T. *Angewandte Chemie International Edition* **2007,** 46, (25), 4630-4660.

4. Wang, X.; Feng, J.; Bai, Y.; Zhang, Q.; Yin, Y. *Chemical reviews* **2016,** 116, (18), 10983-11060.

5. Lou, X. W.; Archer, L. A.; Yang, Z. C. *Advanced Materials* **2008,** 20, (21), 3987-4019.

6. Wang, Z. Y.; Zhou, L.; Lou, X. W. *Advanced Materials* **2012,** 24, (14), 1903-1911.

7. Skrabalak, S. E.; Chen, J. Y.; Sun, Y. G.; Lu, X. M.; Au, L.; Cobley, C. M.; Xia, Y. N. *Accounts Chem Res* **2008,** 41, (12), 1587-1595.

8. Stöber, W.; Fink, A.; Bohn, E. *Journal of colloid and interface science* **1968,** 26, (1), 62-69.

9. Dahl, M.; Liu, Y.; Yin, Y. *Chemical reviews* **2014,** 114, (19), 9853-9889.

10. Chen, X.; Mao, S. S. *Chemical reviews* **2007,** 107, (7), 2891-2959.

11. Schneider, J.; Matsuoka, M.; Takeuchi, M.; Zhang, J.; Horiuchi, Y.; Anpo, M.; Bahnemann, D. W. *Chemical reviews* **2014,** 114, (19), 9919-9986.

12. Joo, J. B.; Zhang, Q.; Dahl, M.; Lee, I.; Goebl, J.; Zaera, F.; Yin, Y. *Energy & Environmental Science* **2012,** 5, (4), 6321-6327.

13. Joo, J. B.; Zhang, Q.; Lee, I.; Dahl, M.; Zaera, F.; Yin, Y. *Advanced Functional Materials* **2012**.

14. Joo, J. B.; Dahl, M.; Li, N.; Zaera, F.; Yin, Y. *Energy & Environmental Science* **2013,** 6, (7), 2082-2092.

15. Joo, J. B.; Lee, I.; Dahl, M.; Moon, G. D.; Zaera, F.; Yin, Y. *Advanced Functional Materials* **2013,** 23, (34), 4246-4254.

16. Liu, H.; Joo, J. B.; Dahl, M.; Fu, L.; Zeng, Z.; Yin, Y. *Energy & Environmental Science* **2015,** 8, (1), 286-296.

17. Dahl, M.; Dang, S.; Joo, J.; Zhang, Q.; Yin, Y. *Crystengcomm* **2012**.

18. Liu, J.; Qiao, S. Z.; Liu, H.; Chen, J.; Orpe, A.; Zhao, D.; Lu, G. Q. *Angewandte Chemie International Edition* **2011,** 50, (26), 5947-5951.

19. Li, N.; Zhang, Q.; Liu, J.; Joo, J.; Lee, A.; Gan, Y.; Yin, Y. *Chemical Communications* **2013,** 49, (45), 5135-5137.

20. Yu, H.; Zhang, Q.; Joo, J. B.; Li, N.; Moon, G. D.; Tao, S.; Wang, L.; Yin, Y. *Journal of Materials Chemistry A* **2013,** 1, (39), 12198-12205.

21. Zhang, Q.; Wang, W. S.; Goebl, J.; Yin, Y. D. *Nano Today* **2009,** 4, (6), 494-507.

22. Yu, L.; Wu, H. B.; Lou, X. W. D. *Accounts Chem Res* **2017,** 50, (2), 293-301.

23. Zhang, Q.; Zhang, T. R.; Ge, J. P.; Yin, Y. D. *Nano Letters* **2008,** 8, (9), 2867-2871.

24. Hu, Y. X.; Ge, J. P.; Sun, Y. G.; Zhang, T. R.; Yin, Y. D. *Nano Letters* **2007,** 7, (6), 1832-1836.

25. Hu, M.; Furukawa, S.; Ohtani, R.; Sukegawa, H.; Nemoto, Y.; Reboul, J.; Kitagawa, S.; Yamauchi, Y. *Angewandte Chemie International Edition* **2012,** 51, (4), 984-988.

26. Yang, N.; Pang, F.; Ge, J. *Journal of Materials Chemistry A* **2015,** 3, (3), 1133-1141.

27. Wang, W.; Sa, Q.; Chen, J.; Wang, Y.; Jung, H.; Yin, Y. *ACS Applied Materials & Interfaces* **2013,** 5, (14), 6478-6483.

28. Gao, C.; Zhang, Q.; Lu, Z.; Yin, Y. *Journal of the American Chemical Society* **2011,** 133, (49), 19706-19709.

29. Retsch, M.; Schmelzeisen, M.; Butt, H.-J.; Thomas, E. L. *Nano Letters* **2011,** 11, (3), 1389-1394.

30. Ye, Q.-L.; Yoshikawa, H.; Bandow, S.; Awaga, K. *Appl Phys Lett* **2009,** 94, (6), 063114.

31. Yao, X.; Bai, Y.; Lee, Y. J.; Qi, Z.; Liu, X.; Yin, Y. *In manuscript* **2017**.

32. Al-Muhtaseb, S. A.; Ritter, J. A. *Advanced Materials* **2003,** 15, (2), 101-114.

33. Pekala, R. W. *Journal of Materials Science* **1989,** 24, (9), 3221-3227.

34. Wang, M.; He, L.; Zorba, S.; Yin, Y. *Nano letters* **2014,** 14, (7), 3966-3971.

35. Turkevich, J.; Stevenson, P. C.; Hillier, J. *Discussions of the Faraday Society* **1951,** 11, (0), 55-75.

36. Lewicki, J. P.; Fox, C. A.; Worsley, M. A. *Polymer* **2015,** 69, 45-51.

37. Duignan, M. R.; Nash, C. A.; Punch, T. M. *Separation Science and Technology* **2008,** 43, (9-10), 2943-2979.

38. Pizzi, A.; Pasch, H.; Simon, C.; Rode, K. *Journal of Applied Polymer Science* **2004,** 92, (4), 2665-2674.

39. Yang, P.; Xu, Y.; Chen, L.; Wang, X.; Mao, B.; Xie, Z.; Wang, S.-D.; Bao, F.; Zhang, Q. *Nano Letters* **2015,** 15, (12), 8397-8401.

40. Van Gils, G. E. *Journal of Applied Polymer Science* **1969,** 13, (5), 835-849.

41. Pei, F.; An, T.; Zang, J.; Zhao, X.; Fang, X.; Zheng, M.; Dong, Q.; Zheng, N. *Advanced Energy Materials* **2016,** 6, (8), 1502539-n/a.

42. Liang, J.; Yu, X.-Y.; Zhou, H.; Wu, H. B.; Ding, S.; Lou, X. W. *Angewandte Chemie International Edition* **2014,** 53, (47), 12803-12807.

43. Fang, X.; Zhao, X.; Fang, W.; Chen, C.; Zheng, N. *Nanoscale* **2013,** 5, (6), 2205-2218.

44. Sun, Y.; Mayers, B. T.; Xia, Y. *Nano Letters* **2002,** 2, (5), 481-485.

45. Wang, Z.; Luan, D.; Li, C. M.; Su, F.; Madhavi, S.; Boey, F. Y. C.; Lou, X. W. *Journal of the American Chemical Society* **2010,** 132, (45), 16271-16277.

46. Liu, X.-C.; Piao, J.-Y.; Bin, D.-S.; Zhang, T.-Q.; Duan, S.-Y.; Wu, Z.-X.; Cao, A.-M.; Wan, L.-J. *Chemical Communications* **2017,** 53, (19), 2846-2849.

47. Cao, J.; Mao, Q.; Shi, L.; Qian, Y. *Journal of Materials Chemistry* **2011,** 21, (40), 16210-16215.

48. Gao, L.; Zhang, L.; Jia, S.; Liu, X.; Wang, Y.; Xing, S. *Electrochimica Acta* **2016,** 203, 59-65.

49. Fan, H.-l.; Ran, F.; Zhang, X.-x.; Song, H.-m.; Niu, X.-q.; Kong, L.-b.; Kang, L. *Nano-Micro Letters* **2015,** 7, (1), 59-67.

50. Li, F.; Xing, Y.; Huang, M.; Li, K. L.; Yu, T. T.; Zhang, Y. X.; Losic, D. *Journal of Materials Chemistry A* **2015,** 3, (15), 7855-7861.

51. Cobley, C. M.; Xia, Y. N. *Mat Sci Eng R* **2010,** 70, (3-6), 44-62.

52. Fielding, L. A.; Mykhaylyk, O. O.; Schmid, A.; Pontoni, D.; Armes, S. P.; Fowler, P. W. *Chemistry of Materials* **2014,** 26, (2), 1270-1277.

Chapter 4

Designing and Structural Engineering of Nanostructures for Optical Applications

4.1 Introduction

Optical properties of nanomaterials such as noble metal nanostructures and photonic crystals are highly dependent on their surrounding media or surrounding refractive index because of light interactions with both surroundings and optical nanomaterials. For example, when the solvents infiltrate into the voids of opal solids, the effective refractive index of the whole colloidal crystal increases due to the replacement of air with solvent, which leads to the red shift of reflection accordingly.[1] The above explains the working principle of photonic crystal sensors, which have been widely investigated to detect ions, solvent, humidity, and volatile organic compounds.[2-5] TiO_2 hollow spheres can switch color from green to purple due to the surroundings changing from air (n=1) to ethanol (n=1.35), which holds great potential for anticounterfeiting and sensing applications.[6]

Localized surface plasmon resonance (LSPR), the collective oscillations of electrons in noble metals at the nanoscale, has found a wide range of potential applications in many areas, such as biotechnology, sensing, and biomedicine.[7-9] The LSPR wavelength, extinction cross-section, and local electric field enhancement are all highly dependent on the material, size, shape, and its surrounding environment.[10]

According to Mie theory, the optical absorption α of metal NPs embedded in a medium of refractive index n is:

$$\alpha = \frac{18\pi Q n^3 \varepsilon_2/\lambda}{(\varepsilon_1 + 2n^2)^2 + \varepsilon_2^2}$$

where Q is the volume fraction of nanoparticles and ε_1 and ε_2 are the cluster-size dependent dielectric constants which are functions of radius (r) and wavelength (λ).[11, 12] Therefore, the extinction position can be tailored by changing the n of the matrices. As discussed in Chapter 2, the chemical composition and shape of noble metal nanostructures will greatly affect their LSPR properties, where Ag-Au alloy NRs manifest strong and tunable plasmon resonances. Simulation results in Figure 4.1 clearly illustrate the effect of local refractive index on LSPR frequencies, where the extinction peak positions of 70 nm Au NPs gradually red-shift upon increasing the refractive index of surrounding medium. The polarization of the surrounding medium is used to explain this red-shift phenomenon.[10] Basically, an electric field near the NPs will induce the polarization of the dielectric medium, leading to charge accumulations at the interface between the dielectric medium and the metallic NP, which will partially compensate the charge accumulation and reduce the net charge at the NP surface. The larger refractive index, the larger the polarization charge, and thus the larger the effect on the LSPR. Reduction in the net charge leads to smaller resonant frequency. Therefore, increasing the dielectric constant of the surrounding media will shift the LSPR band towards longer wavelengths (red shift). As shown in Figure 4.1, the resonance intensity also increases with increasing the refractive index of the medium, which is expected because the amplitude at resonance will increase when the resonance frequency decreases.[10]

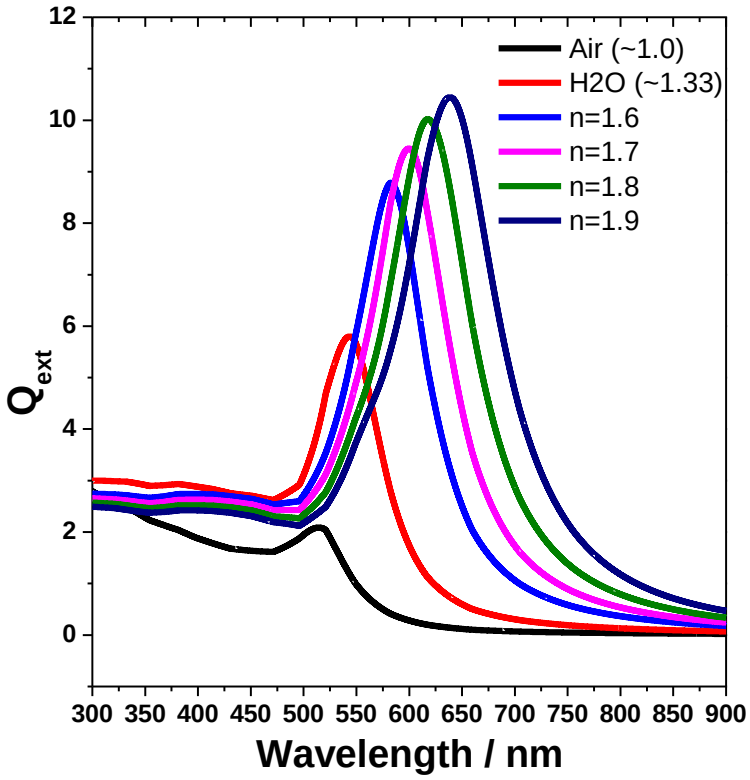

Figure 4.1 Optical extinction spectra for Au NPs with 70 nm size in a dielectric medium with different dielectric functions calculated according to Mie theory. The y-axis is extinction efficiencies.

The plasmonic properties of Au and Ag nanostructures can be tailored by structurally engineering the surrounding media. One of the efficient ways to control LSPR properties is to construct metal@shell (non-metal) core-shell architectures. By engineering the shell composition as well as the shell thickness, one can fine-tune the optical responses of metallic NPs and set the plasmon resonances at a specific wavelength or spectral region to match a specific application, which has stimulated tremendous interest in studying hybrid nanostructures.[13] For instance, epitaxial growth of Cu_2O on Au and Ag nanoparticles to form Au@Cu_2O and Ag@Cu_2O core-shell structures allow for fine control over LSPR properties.[14-16] Noteworthy is that the shell material can not only enrich the plasmonic tunability but also protect the metal core from aggregation and stabilize the colloidal objects. Another way is to change the LSPR peak positions and cross-section intensity in a reversible manner by incorporating the Au and Ag nanostructures into surrounding active media, which can change their refractive properties upon external stimuli, such as pH, light, and temperature.[17, 18] For example, the LSPR peak of gold nanoparticles in a weak polyelectrolyte gel network has been reversibly tuned by changing the environmental pH, owing to the packing density change and hence the resulting refractive index change in the polyelectrolyte gel network induced by the swelling−deswelling mechanism.[19]

In this Chapter, two scenarios which are related to the effect of surrounding refractive index are discussed. First, the dichroic property of noble metal NPs on a mirrored substrate has been investigated. By tuning the dielectric environment of those metal NPs, we have achieved a wide range of dichroic colors. In the other section, the

drying process of hollow TiO_2 spheres has been revealed by studying their optical responses.

4.2 Experimental

4.2.1 Synthesis of hollow TiO_2 shells

Hollow TiO_2 shells were synthesized by using an established procedure.[20] Colloidal silica spheres with 200 nm diameter were synthesized and dispersed in 5 ml of absolute ethanol for TiO_2 coating, followed by adding into a mixture of absolute ethanol (15 ml), acetonitrile (ACN, 7 ml), and hydroxypropyl cellulose (HPC, 0.05g). After magnetic stirring for 15 min, 0.2 mL of $NH_3 \cdot H_2O$ was subsequently added. Finally, the mixture of titanium n-butoxide (TBOT, 1 mL), ethanol (3 mL) and ACN (1 mL) was injected quickly into the above system. The precipitate was separated by centrifugation after stirring for 2 h, and washed 3 times with ethanol and 2 times with water. Then, the as-obtained $SiO_2@TiO_2$ sample was re-dispersed in 20 mL of de-ionized water. Silica templates were easily removed in an aqueous NaOH solution at room temperature.

4.2.2 Synthesis of Au@TiO_2 yolk-shell nanostructures

Au@SiO_2 were first synthesized per section 3.2.5 and dispersed in 5 ml of absolute ethanol. The TiO_2 coating was then applied to the Au@SiO_2 spheres. After removal of silica template, the Au NPs (~20 nm) in the yolk-shell structures were used as seeds for the seeded growth of larger Au NPs according to a procedure reported by our group.[21] Typically, a specific amount of Au@TiO_2 yolk-shell structures were quickly injected into a freshly prepared growth solution of Au containing 500 μL of PVP (5 wt%), 250 μL of L-ascorbic acid (0.1 M), 200 μL of KI (0.2 M), 60 μL of $HAuCl_4$ (0.25 M),

and 2 mL of H_2O. After 10 min the Au nanoparticles formed were collected by centrifugation and redispersed in water. The size of the Au nanoparticles can be facilely tuned by injecting different amounts of the seed solution in a defined typical synthesis.

4.2.3 One-pot synthesis of Ag@RF core-shell nanostructures

Ag@RF core-shell nanoparticles were synthesized using an established procedure.[22] 31.2 mL of an aqueous solution containing 0.01 g of resorcinol, 0.14 mL of formaldehyde, 30 mL of water, and 1 mL of 0.01 M $AgNO_3$ was mixed in a three-necked flask under vigorous magnetic stirring. The solution was then heated to boiling. After 0.1 mL of 2.8 wt% $NH_3 \cdot H_2O$ was injected, the solution was refluxed for 30 min. The core-shell particles were then collected by centrifugation and re-dispersed in ethanol.

4.2.4 Synthesis of Ag NPs and Ag@Cu_2O core-shell NPs

Ag NPs were prepared by kinetically controlled seeded growth from a reported procedure.[23] In a typical preparation of seed solution, 5 mL of PVP (5 wt % in H_2O) and 10 μL of $HAuCl_4$ (0.25 M) were dissolved in 5 mL of H_2O. After that, 0.6 mL of $NaBH_4$ (0.1 M) was injected under vigorous stirring, giving rise to a yellowish solution of Au nanoparticles. The Au nanoparticles obtained were then aged for 6 h. For the seeded growth of Ag NPs, 2 mL of PVP (5 wt % in H_2O), 1 mL of acetonitrile, and 200 μL of ascorbic acid (0.1 M) were added in 2 mL of H_2O, followed by adding 150 μL of $AgNO_3$ (0.1 M) and quick injection of 1.2 μL of the seed solution. After 15 min of reaction, the Ag quasi-nanospheres were finally collected by centrifugation and re-dispersed in 2 ml water. Ag@Cu_2O core-shell nanoparticles were synthesized through epitaxial growth of Cu_2O nanoshells on Ag surfaces at room temperature.[14] Typically, 0.5 mL of colloidal Ag

quasi-spherical nanoparticles was first introduced into 5 mL of 2 wt % PVP aqueous solution. Various amounts (2.5–100 μL) of 0.1 M $Cu(NO_3)_2$ solution, depending on the desired thickness of the resulting Cu_2O shells, was subsequently added. Then 11.2 μL of 5 M NaOH and 5 μL of N_2H_4 solution (35 wt %) were added under magnetic stir. The solutions were kept stirring for 10 min and the resulting core–shell nanoparticles were subsequently separated from the reaction mixtures by centrifugation.

4.2.5 Characterizations

Morphology was characterized by using a Tecnai T12 transmission electron microscope (TEM). A probe-type Ocean Optics HR2000CG-UV-NIR spectrometer was used to measure the UV-Vis extinction spectra and transmittance spectra.

4.3 Dichroic film on mirrored substrate

Date back to the 4^{th} century, the Romans created the dichroic Lycurgus Cup containing gold and silver nanoparticles that can appear different colors depending on the direction of light illumination because of the light absorption and scattering. When light interacts with noble metal nanostructures, light is either absorbed or scattered, causing extinction of the incidence light. The size of metal NPs has a dramatic effect on the light absorption and scattering, in which the increase in the size resulted in an increase in the extinction cross-section as well as the relative contribution of scattering.

In this section, we propose and demonstrate a design strategy to show an angle-dependent dichroic film on a mirrored substrate based on the light absorption and scattering of plasmonic nanomaterials. Spray-coating of core-shell or yolk-shell nanoarchitectures are proposed to realize the dichroic properties. When light is shone on

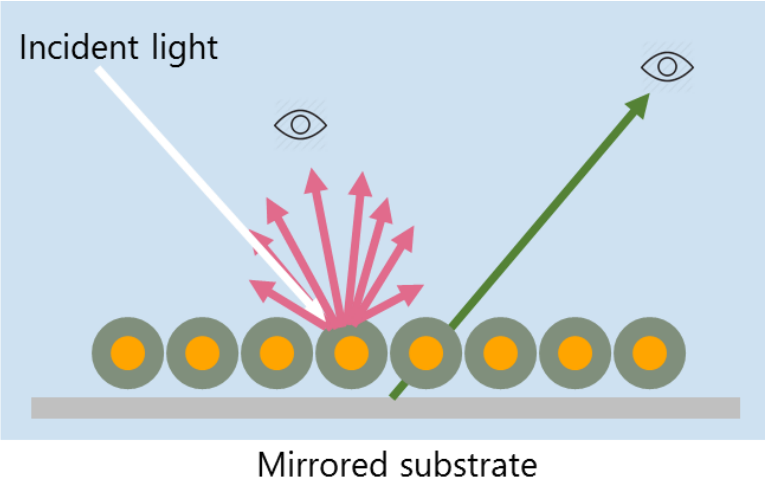

Figure 4.2 Schematic illustration of the working principle for the dichroic film on a mirrored substrate.

to it, the film appears bright green color from the reflection direction and changes to red when viewed from all other angles. We have also proposed and expanded the red-green color system to a wide range of colors by utilizing various core-shell nanostructures. Anti-counterfeiting has also been demonstrated practicable by using the dichroic optical behavior.

Figure 4.2 illustrates the design and working principle for the angular dependent dichroic film on a mirrored substrate. There are two possibilities of interaction of a medium with light, which are scattering and absorption. When incidence light illuminate on an ideal mirrored substrate, light will be specular reflected at a definite angle. Applying a coating of plasmonic nanomaterials will change the interactions between incidence light and substrate. The incidence light will be scattered and absorbed by the plasmonic nanomaterials, resulting in the transmitted light reaching to the mirrored surface and being reflected. From the view angle of reflection, the transmitted light through plasmonic NPs will be perceived, while the scattered light will be observed from the other view angles.

In the present work, to fabricate films with dichroic properties, loading plasmonic NPs on the substrate remains challenging. Here we propose to utilize core-shell or yolk-shell architecture to resolve the following issues. The shells play an important role for the successful observation of the dichroic property. It is worthy to mention that the loading density of noble metal nanoparticles on a substrate using conventional method such as dipping coating and lithography is usually low, which makes the optical responses weak. The spray-coating of colloidal particles has recently attracted much interest due to its

simplicity, low cost and scalability over a large area on both planar and curved surfaces.[24, 25] However, the spray-coating of colloidal Au NPs using air brush is not feasible because interparticle interactions caused by aggregations after drying will weaken the plasmon resonances. Different form Au NPs, the dielectric shells can prevent the Au NPs from aggregation so that spray-coating thicker films to increase the scattering intensity without affecting LSPR properties is feasible. On the other hand, the interaction between Au NPs and the substrate can also be avoided by the outer shells, preserving the origin of the colors from plasmon resonances of the metal NP itself.

Based on the above design, we first synthesized Au@TiO_2 yolk-shell nanostructures through a hard templating method followed by a seed mediated growth of Au NPs. The TEM image in Figure 4.3a shows the typical morphology of the Au@TiO2 yolk-shell nanostructures with 110 nm Au NPs and 60 nm amorphous TiO_2 shells. Figure 4.3b shows the UV-vis extinction spectra, where a strong resonance peak appears at 610 nm. The gold NPs with size of 112 nm in diameter manifest a LSPR peak at ~585 nm, indicating the TiO_2 shells in the yolk shell structures will affect surrounding refractive index of Au NPs and red-shift the resonance peak although TiO_2 is not directly coated on the Au NPs.[21] As mentioned above, the increase in the size of Au NPs results in an increase in the relative contribution of scattering to the whole extinction, suggesting larger gold NPs exhibit stronger scattering.[10] For colloidal dispersion of small gold NPs (e.g. 20 nm), the red color we perceive is the transmitted light because the scattering of such small gold NPs is negligible. For larger gold NPs, the scattering becomes noticeable and the dichroic feature occurs. As shown in Figure 4.3b, the dispersion of the Au@TiO_2

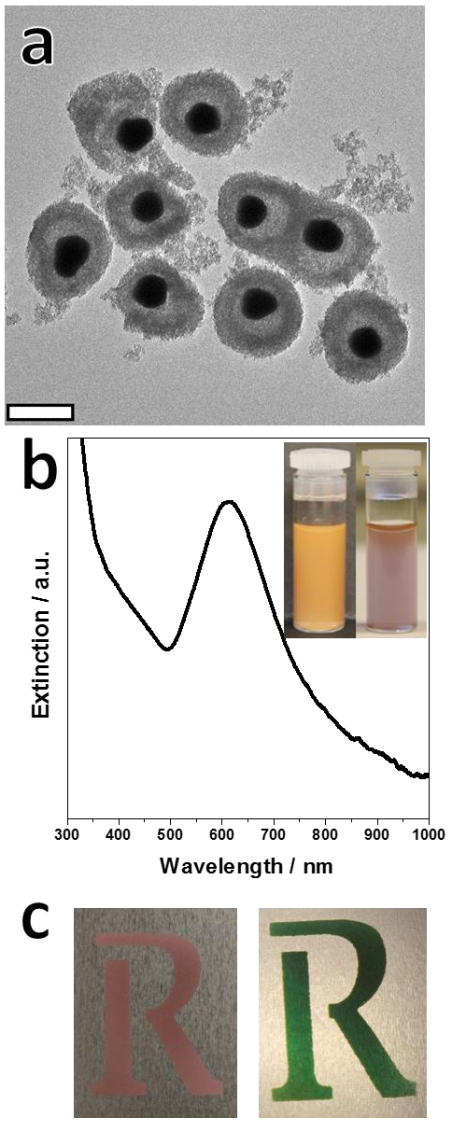

Figure 4.3 (a) TEM image showing Au@TiO_2 yolk-shell nanostructures. The scale bar is 200 nm. (b) UV-vis-NIR spectra of the yolk-shell structures. Inset shows the digital images of the dispersion with different background. (c) Digital images showing the dichroic properties on stainless steel. Green one was taken from the reflection angle and the red one is taken from the top.

structures exhibit a dichroic feature similar to the Lycurgus cup, where orange color is observed for the dispersion with a black background and blue color with red tone is perceived owing to the combination of scattered light and transmitted light. The dichroic properties of the Au nanostructures on a mirrored substrate were then investigated. The Au@TiO_2 yolk-shell structures can be well dispersed in ethanol and easily spray-coated onto a mirrored substrate such as stainless steel using an air brush. As shown in Figure 4.3c, bright green letter R can be observed from the view angle of reflection when shining light, while red color is perceived from all other angles.

To investigate the function of mirrored substrate, the yolk-shell nanostructures were applied onto a glass substrate (Figure 4.4a). Without a mirrored substrate, the optical behavior of the glass slide is like the behavior of Au NP dispersion or the Lycurgus cup. When the stainless-steel substrate was placed under the glass slide, similar dichroic properties are observed, indicating there is no interaction between Au NPs and the substrate. We have also demonstrated the aluminum foil can also act as a reflecting mirror layer, as shown in Figure 4.4b. Using the robust spray-coating strategy along with patterns, various shaped color display can be readily achieved. As shown in Figure 4.4c, a butterfly pattern was used and red-green switching of butterfly has been realized. In addition to Au@TiO_2 yolk-shell nanostructures, Au@SiO_2 core-shell structures can also be used for the dichroic film (Figure 4.4d), in which the silica shells play the same role as TiO_2 shells.

Next, we further extended the dichroic properties to Ag NPs to enrich the ranges of colorations. As discussed in Chapter 2, Ag has the largest quality factor across most of

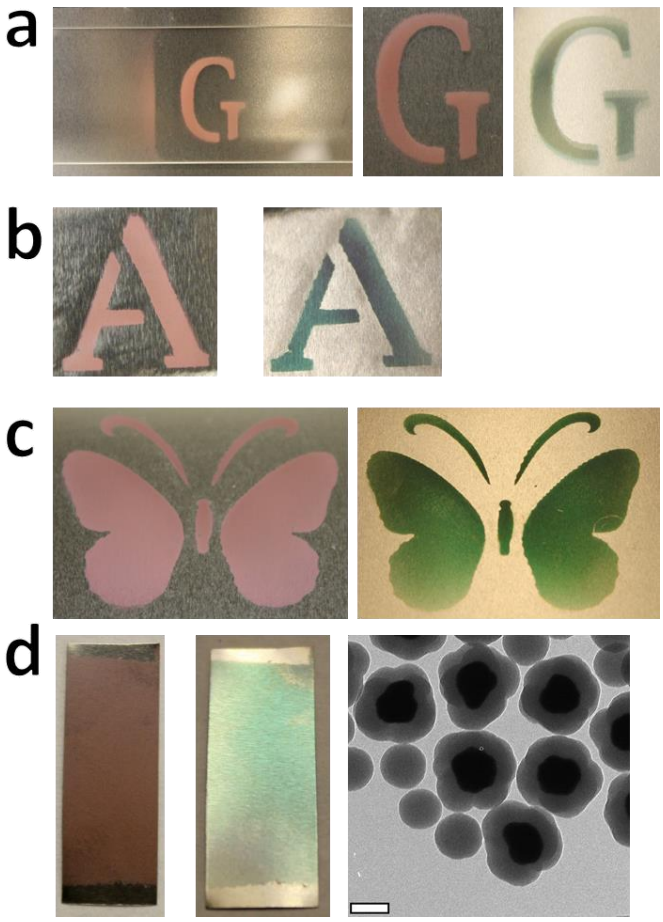

Figure 4.4 Dichroic properties on different substrates. Au@TiO_2 yolk-shell structures spray-coated on (a) glass substrate with stainless steel underneath and (b) aluminum substrate. (c) Patterned dichroic film on stainless steel. (d) Dichroic film by spray-coating Au@SiO_2 core-shell structures on stainless steel. The right TEM image shows the morphology of Au@SiO_2 core-shell nanostructures. The scale bar is 100 nm.

the spectrum and exhibits strong electric field enhancement.[26] Ag NPs exhibit stronger scattering compared with gold NPs of same size. In addition, Ag nanostructures can support surface plasmons across the whole visible spectrum, making it an ideal choice for constructing dichroic films with wide range of colors. Finally, Ag is much cheaper than gold, especially when the size of gold NPs needs to be large enough to scatter light. As a demonstration, we prepared Ag@RF core-shell nanostructures through a one-pot synthesis approach developed by Zhang and co-workers.[22] Figure 4.5a shows the TEM image of monodisperse Ag@RF core-shell nanoparticles with 45 nm Ag NPs and 30 nm RF shells. As shown in Figure 4.5b, colloidal Ag@RF NPs exhibit a sharp and strong resonant peak at 466 nm. The colloidal dispersion shows jade green color from scattering and red-orange color for transmitted light. After the dispersion was spray-coated on a stainless-steel substrate, the film can display two colors: pink from the reflected view angle and jade green from all other directions (Figure 4.5 c and d). As mentioned above, the resonance frequencies of the Ag NPs can be facilely tuned across the whole visible spectrum by controlled epitaxial growth of Cu_2O of various thickness using a robust wet chemistry approach. As revealed in Figure 4.5e, the plasmon resonance peak position can be manipulated over the whole visible range by simply adding different volume of copper precursor. The digital images in Figure 4.5f shows the dichroic properties of three typical samples of Ag@Cu_2O, where purple, blue and green color can be observed through the transmittance mode, while orange and red color can be perceived with a black background. Therefore, the capabilities to fine-control over the optical properties of Ag@Cu_2O core-shell NPs enable us to develop dichroic films with complex colorations.

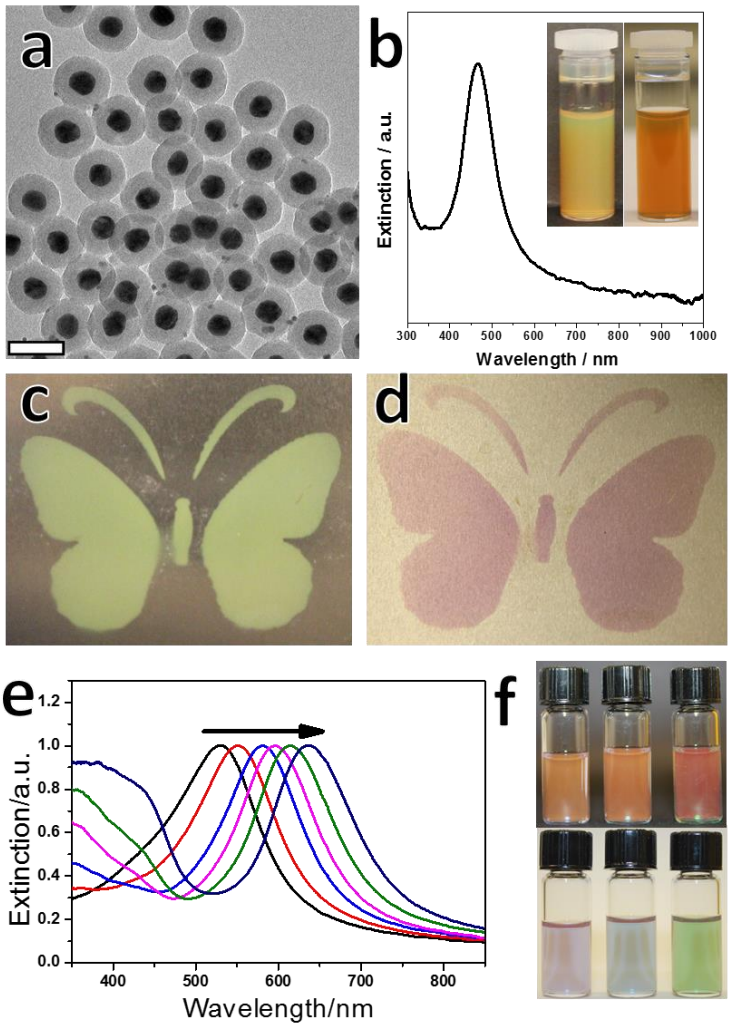

Figure 4.5 (a) TEM image of Ag@RF core-shell nanoparticles. The scale bar is 100 nm. (b) UV-vis-NIR spectra of the Ag@RF structures. Inset shows the digital images of the dispersion with different background. Digital images showing the dichroic properties of the Ag@RF nanostructures view from different angles. (c) From the top and (d) from the reflected angle. (e) UV-vis-NIR extinction spectra of $Ag@Cu_2O$ core-shell nanoparticles with increasing volume of $Cu(NO_3)_2$. (f) Digital images showing the dispersion of $Ag@Cu_2O$ particles with different background.

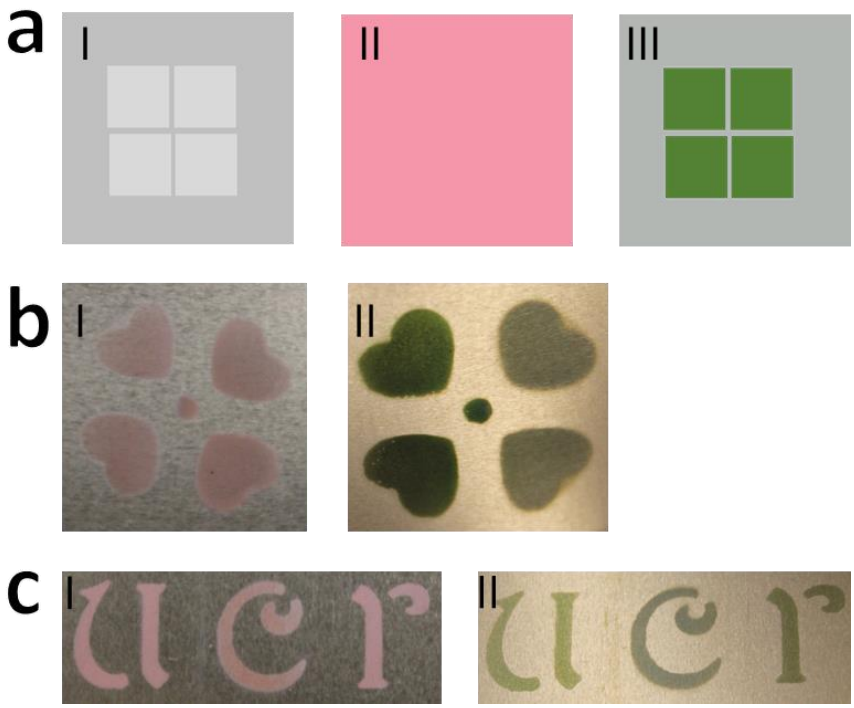

Figure 4.6 (a) Schematic illustration for the design of anti-counterfeiting film. (I) Patterning the substrate, (II) and (III) viewing the substrate from different angles. Two demonstrations utilizing the patterned dichroic films for anti-counterfeiting. (b) Heart-shaped flower with the right two hearts on HPC coated stainless steel. (c) Letters of *ucr* with the letter *c* on HPC coated stainless steel.

Finally, the dichroic film on the mirrored substrate have been demonstrated for a potential application of anti-counterfeiting. The scattering is negligibly affected by the mirrored substrate while the reflected light or transmitted light (which are similar in this case) depends on the mirrored surface. Based on this understanding, we have proposed an information-encoding platform with enhanced anti-counterfeiting features. As illustrated in Figure 4.6a, the mirrored stainless steel substrate was first spray-coated with a patterned layer of dielectric material such as polymer (e.g. HPC) to change the surface reflectivity, followed by spray-coating the desired plasmonic nanomaterials to form a film. The same optical responses are found in the presence or absence of the dielectric layer when viewed from most directions, which can be used for encoding the information. The decoding can be realized by perceiving the film from the reflected angle, where the mirrored surface determines the reflection angle. As a simple demonstration, two patterns are used: one is heart-shaped flower, the other one is letters of *ucr*. As shown in Figure 4.6 b and c, there are no color differences for the patterns of flower and letters when viewed from the aspect of scattering, both of which show red color. When illuminating the substrate, and viewing from the reflected direction, the color information can be clearly revealed, in which the polymer coated areas (two hearts and letter c) look dark greenish while the uncoated areas display bright green color. The encoded information can be made more complex by introducing Ag nanostructures for multi-color encoding. In addition, the mirrored surface can be realized on planar and curved substrates (e.g. PET) by depositing metal reflectors such as aluminum, providing a great platform for creating patterned dichroic films with high complexities.[25, 27]

4.4 *In-situ* optical probing on drying process of hollow structures

Based on Mie theory, the Mie resonance is dependent on the relative refractive indexes of both the core and shell materials to the surrounding medium. We have reported that the color of visible Mie scattering in the hollow TiO_2 shell was highly responsive to the surrounding medium.[6] For example, the purple hue of the hollow TiO_2 spheres switches to blue color after spraying ethanol onto the patterned film. The color can change back after the evaporation of ethanol. It is thus desirable to investigate the related evaporation process. The aim of this study is to analyze the evaporation of solvent or the drying process in a spray-coated film containing hollow TiO_2 spheres.

The hollow TiO_2 shells used in this study were prepared based on TiO_2 coating on colloidal silica template. After removal of silica, no further treatment such as calcination was made to the hollow shells, indicating the amorphous nature of TiO_2 shells. Figure 4.7 shows a typical TEM image of hollow TiO_2 shells with 200 nm inner diameter and 25 nm shell thickness. We used a spray-coating technique to spread the TiO_2 particles onto a polystyrene substrate, which was also used in the preparation of dichroic film in the Section 4.3. After coating of TiO_2 hollow shells, the clear substrate becomes translucent, as shown in Figure 4.7 b (i). After 5 µl of ethanol was dropped onto it, the substrate appears much more clear (Figure 4.7 b (ii)) because water is filtrated into the pores, which dramatically reduces the number of scattering interfaces.[28] During the drying process, there is an intermediate stage in which the substrate is opaque and white, as revealed in Figure 4.7 b (iii). This is because a large area of unfilled open pores is formed

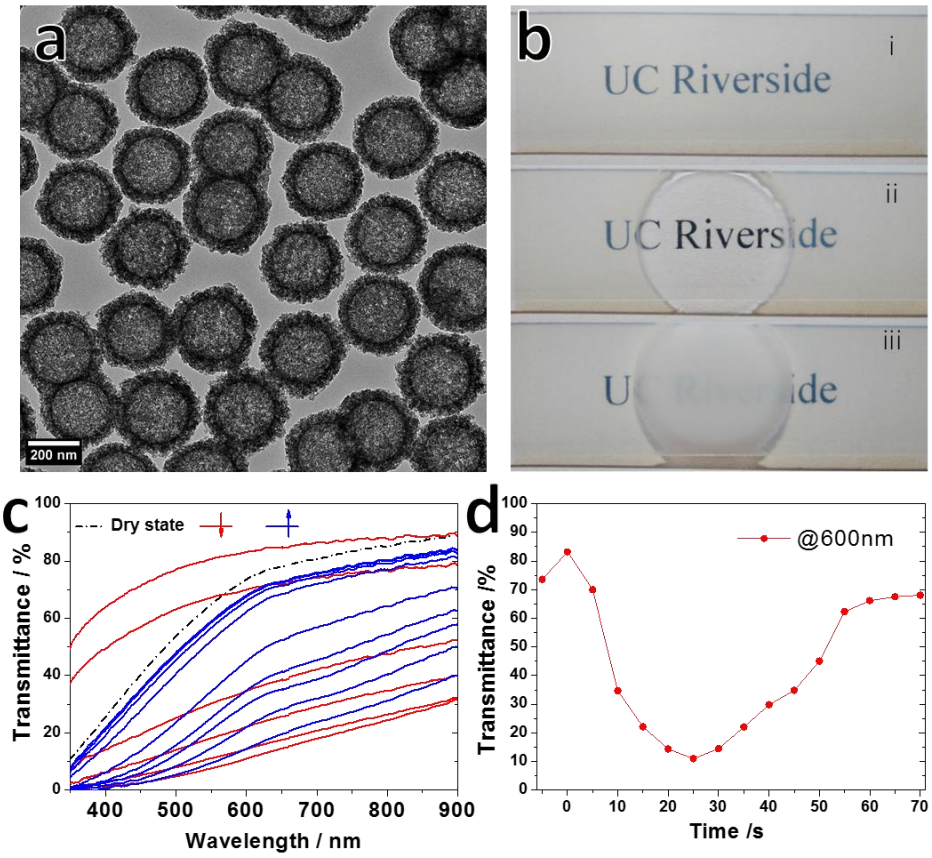

Figure 4.7 (a) TEM image of TiO_2 hollow shells. (b) Digital images showing (i) TiO_2 shells on polystyrene substrate, (ii) Applying ethanol, and (iii) Opaque effect during drying process. (c) Optical transmittance spectra during the drying process. (d) Dependence of the transmittance at 600 nm on the drying time.

in the film and more light is scattered at the water/air interface. Similar phenomena are found in nature, where the petals of Diphylleia grayi turn from white to transparent in the rain.[29]

UV-vis spectroscopy has been applied to study dynamic processes such as growth of gold nanorods in a tubular template, formation of silver nanoplate, and surface-protected etching of silica spheres.[30-32] As the transmittance is varying during the drying process, it is thus a good way to use UV-vis spectroscopy to monitor the drying process of the film in an in-situ manner. As shown in Figure 4.7c, dynamic transmittance spectra for the drying of hollow TiO_2 shells on a PS substrate are recorded at an interval of 5 seconds. During the drying process or the solvent (ethanol in this study) evaporation process, the transmittance first decreases very quickly (red lines) and then gradually returns to almost the initial dry state. For better illustration, we summarize the dependence of the transmittance at 600 nm on the drying time, as shown in Figure 4.7d. The initial dry state shows a transmittance value of 74% and there is a 10% increase after dropping ethanol, which is consistent with the digital images shown in Figure 4.7b. In the first 25 seconds, the transmittance quickly decreases to 11%, which is opaque as shown in Figure 4.7 b (iii). The modulation of light transmittance through external stimuli is useful in smart devices such as smart windows.[28, 33] At the initial drying stage, the air quickly substitutes the evaporated solvent, resulting in rapid formation of abundant air/liquid interface to scatter the light. The continuing evaporation of ethanol leads to a decrease of air/liquid interface and thus an increase in transmittance. As the hollow

particles are movable, there will be microcracks formed after drying, leading to slight decrease in transmittance after drying.[34]

As discussed in the introduction, the LSPR peak position is dependent on the surrounding refractive index. Au NPs can be used as probes to sense their local environment changes. To investigate the drying process in detail, we incorporated 70 nm Au NPs into the film of hollow TiO_2 shells to monitor the drying process. The Au NPs were either encapsulated in the shells or directly mixed with hollow TiO_2 shells. Au@TiO_2 yolk-shell nanostructures were prepared through a hard templating method followed by a seed mediated growth of Au NPs. The drying process of the film composite was then monitored by UV-vis-NIR spectrometer. As shown in Figure 4.8 a, the extinction spectra are recorded at an interval of 1 second. The surface plasmon resonance peak shifts from 528 nm to ~560 nm after infiltration of solvent into the dry film because the surrounding of Au NPs changes from air (n=1) to ethanol (n=1.35). During the drying process, the extinction intensities first rise and then fall back, which is consistent with the transmittance spectra shown in Figure 4.7. The resonance peak of Au NPs is unchanged during the rising stage, while there is a quick blue-shift of the resonance peak with the decreasing of extinction intensities. Figure 4.8c summarize the time evolution of resonance peak position and peak intensity during the evaporation process of ethanol. When the peak intensity reaches to its maximum, the peak position is at ~560 nm, indicating the Au NPs are surrounding with ethanol. It is noteworthy that the time scale of evaporation varies from each drying process possibly because evaporation is affected by the rate of airflow, which is not controlled in the measurement. Figure 4.8b shows the

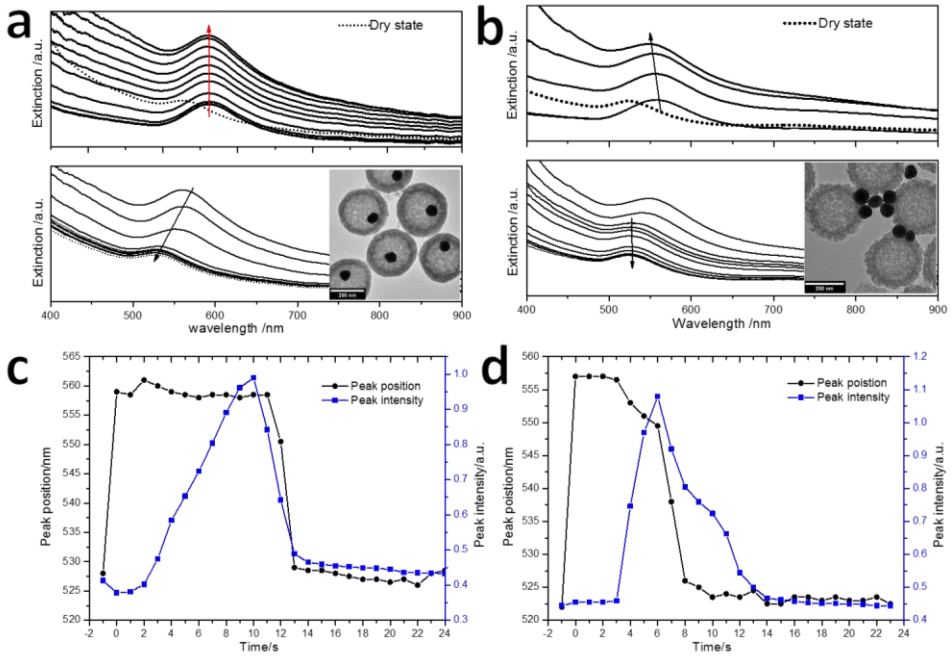

Figure 4.8 Optical extinction spectra during drying process of (a) Au@TiO_2 yolk-shell structures and (b) Au/TiO_2 shell mixture. The insets in (a) and (b) show the TEM images of the yolk-shell structures and Au/TiO_2 shell mixture, respectively. Dependence of peak position and peak intensity on the drying time. (c) Au@TiO_2 yolk-shell and (d) Au/TiO_2 mixture.

extinction spectra evolution for the film with a mixture of Au NPs and TiO_2 shells. The evolution of peak intensity is similar. As shown in Figure 4.8d, the surface plasmon resonance peak starts to blue-shift before the peak intensity reaches to its maximum, and keeps blue-shifting when the peak intensity is decreasing, suggesting the evaporation of the ethanol outside of the shells first.

From these UV-vis-NIR spectra results, we deduce the following drying sequence of hollow TiO_2 shells. The solvent surrounding the hollow shells in the stacking pores first evaporates. Air invades into the dried space and cause light scattering at the air/solvent and air/solid interfaces, which leads to the dramatic decrease in transmittance. The voids in the hollow shells then starts to dry and empty once the hollow shell walls are exposed to air.

4.5 Conclusion

In conclusion, a dichroic film has been designed on a mirrored substrate based on the scattering and absorption of plasmonic nanomaterials. Spray-coating of core-shell nanostructures has been proposed to realize the dichroic properties. The shell materials in the core-shell structures play an important role in protecting the noble metal core from aggregation and interactions. In addition, fine-control over the core-shell structures allow the optical properties tunable across the visible spectral regions, which enriches the color complexities of dichroic film. The application in anti-counterfeiting has been successfully demonstrated by manipulating the surface of mirrored substrate, where the encoded information can be made more complex by introducing multi-color encoding.

4.6 References

1. Zhang, Y.; Fu, Q.; Ge, J. *Nature communications* **2015,** 6, 7510.

2. Diao, Y. Y.; Liu, X. Y.; Toh, G. W.; Shi, L.; Zi, J. *Advanced Functional Materials* **2013,** 23, (43), 5373-5380.

3. Wang, Z.; Zhang, J.; Li, J.; Xie, J.; Li, Y.; Liang, S.; Tian, Z.; Li, C.; Wang, Z.; Wang, T.; Zhang, H.; Yang, B. *Journal of Materials Chemistry* **2011,** 21, (4), 1264-1270.

4. Chen, C.; Zhu, Y.; Bao, H.; Shen, J.; Jiang, H.; Peng, L.; Yang, X.; Li, C.; Chen, G. *Chemical Communications* **2011,** 47, (19), 5530-5532.

5. Holtz, J. H.; Asher, S. A. *Nature* **1997,** 389, (6653), 829-832.

6. Yao, X.; Bai, Y.; Lee, Y. J.; Qi, Z.; Liu, X.; Yin, Y. *In manuscript* **2017**.

7. Hu, M.; Chen, J.; Li, Z.-Y.; Au, L.; Hartland, G. V.; Li, X.; Marquez, M.; Xia, Y. *Chemical Society reviews* **2006,** 35, (11), 1084-1094.

8. Yang, X.; Yang, M.; Pang, B.; Vara, M.; Xia, Y. *Chemical reviews* **2015,** 115, (19), 10410-10488.

9. Willets, K. A.; Van Duyne, R. P. *Annu Rev Phys Chem* **2007,** 58, 267-297.

10. Garcia, M. A. *Journal of Physics D: Applied Physics* **2011,** 44, (28), 283001.

11. Mie, G. *Annalen der Physik* **1908,** 330, (3), 377-445.

12. Medda, S. K.; De, S.; De, G. *Journal of Materials Chemistry* **2005,** 15, (32), 3278-3284.

13. Jiang, R.; Li, B.; Fang, C.; Wang, J. *Advanced Materials* **2014,** 26, (31), 5274-5309.

14. Jing, H.; Large, N.; Zhang, Q.; Wang, H. *The Journal of Physical Chemistry C* **2014,** 118, (34), 19948-19963.

15. Zhang, L.; Jing, H.; Boisvert, G.; He, J. Z.; Wang, H. *Acs Nano* **2012,** 6, (4), 3514-3527.

16. Zhang, L.; Blom, D. A.; Wang, H. *Chemistry of Materials* **2011,** 23, (20), 4587-4598.

17. Jeon, J.-W.; Ledin, P. A.; Geldmeier, J. A.; Ponder, J. F.; Mahmoud, M. A.; El-Sayed, M.; Reynolds, J. R.; Tsukruk, V. V. *Chemistry of Materials* **2016,** 28, (8), 2868-2881.

18. Jain, P. K.; Huang, X.; El-Sayed, I. H.; El-Sayed, M. A. *Accounts Chem Res* **2008,** 41, (12), 1578-1586.

19. Tokarev, I.; Tokareva, I.; Minko, S. *Advanced Materials* **2008,** 20, (14), 2730-2734.

20. Liu, H.; Joo, J. B.; Dahl, M.; Fu, L.; Zeng, Z.; Yin, Y. *Energy & Environmental Science* **2015,** 8, (1), 286-296.

21. Gao, C.; Vuong, J.; Zhang, Q.; Liu, Y.; Yin, Y. *Nanoscale* **2012,** 4, (9), 2875-2878.

22. Yang, P.; Xu, Y.; Chen, L.; Wang, X.; Zhang, Q. *Langmuir : the ACS journal of surfaces and colloids* **2015,** 31, (42), 11701-11708.

23. Liu, X.; Yin, Y.; Gao, C. *Langmuir : the ACS journal of surfaces and colloids* **2013,** 29, (33), 10559-10565.

24. Ge, D.; Yang, L.; Wu, G.; Yang, S. *Chemical Communications* **2014,** 50, (19), 2469-2472.

25. Ge, D.; Yang, L.; Wu, G.; Yang, S. *Journal of Materials Chemistry C* **2014,** 2, (22), 4395-4400.

26. Rycenga, M.; Cobley, C. M.; Zeng, J.; Li, W.; Moran, C. H.; Zhang, Q.; Qin, D.; Xia, Y. *Chemical reviews* **2011,** 111, (6), 3669-3712.

27. Choi, D.; Shin, C. K.; Yoon, D.; Chung, D. S.; Jin, Y. W.; Lee, L. P. *Nano Letters* **2014,** 14, (6), 3374-3381.

28. Yao, X.; Hu, Y.; Grinthal, A.; Wong, T.-S.; Mahadevan, L.; Aizenberg, J. *Nat Mater* **2013,** 12, (6), 529-534.

29. Yong, J.; Chen, F.; Yang, Q.; Du, G.; Shan, C.; Bian, H.; Farooq, U.; Hou, X. *Journal of Materials Chemistry A* **2015,** 3, (18), 9379-9384.

30. Gao, C.; Zhang, Q.; Lu, Z.; Yin, Y. *Journal of the American Chemical Society* **2011,** 133, (49), 19706-19709.

31. Zhang, Q.; Li, N.; Goebl, J.; Lu, Z.; Yin, Y. *Journal of the American Chemical Society* **2011,** 133, (46), 18931-18939.

32. Zhang, Q.; Zhang, T. R.; Ge, J. P.; Yin, Y. D. *Nano Letters* **2008,** 8, (9), 2867-2871.

33. Ge, D.; Lee, E.; Yang, L.; Cho, Y.; Li, M.; Gianola, D. S.; Yang, S. *Advanced Materials* **2015,** 27, (15), 2489-2495.

34. Cardinal, C. M.; Francis, L. F.; Scriven, L. E. *Journal of Coatings Technology and Research* **2009,** 6, (4), 457-469.